UTILIZING UNMANNED AERIAL VEHICLES FOR ATMOSPHERIC DATA ACQUISITION

A Thesis

Submitted to the Graduate Faculty of the
University of South Alabama
in partial fulfillment of the
requirements for the degree of

Master of Science

in

Mechanical Engineering

by
Lisa M. Schibelius
M.S., University of South Alabama, 2018
July 2018

ProQuest Number: 10840176

ProQuest 10840176

To my daughter, Madelyn,

who has been my strength and inspiration

ACKNOWLEDGEMENTS

This work would not have been possible without the overwhelming support and guidance from a number of people. They say you are the sum of the experiences, encounters, and people you have met throughout your life, and I am thankful to have met such influential and supportive human beings. My advisor, Dr. Carlos Montalvo, has had the most profound impact on my life, both professionally and personally since he became my undergraduate thesis advisor almost four years ago. Here we are again today, at the end of my second thesis, and we have both become better for it. He always said, "baby steps," and taught me to take every day one step at a time. He enouraged me to keep pushing forward and to never forget who I am and what is important to me, and I am forever grateful.

I would like to thank my committee members, Dr. Carlos Montalvo, Dr. Sytske Kimball, and Dr. Joseph Richardson, and all of the Engineering faculty at the University of South Alabama (there are too many to list) for providing such an encouraging environment for my growth and igniting my love for engineering. What I have gained both professionally and personally from the people and my experiences at South has been immeasurable.

This research would not have been possible without the hard work of our team of undergraduates, graduates, pilots, FAST lab members and the guidance from Dr. Montalvo and Dr. Kimball. Thank you to Nemo Hyunh for being my support through graduate school. Life wouldn't have been as fun without you - and there is no other graduate student I'd rather have had working by my side. I am equally thankful to Cody Salter - your wise input and guidance steered both Nemo and I

through the chaos of life and graduate school. Thanks, Matt Simmons, for your research contributions and work with sensors and wind tunnel testing. I hope you can carry on our research and that you enjoy graduate school and working with Dr. C as much as I have. Thank you to the undergraduate students, Rockwell Garrido, Alicia Ratcliffe, Harrison White, and the pilots - Jake Magnin, Colin Carithers, Jonah Phillips, Quinn Currie (and several others) for your contributions to our research and assistance with flight testing.

Thank you to my family - Christopher Hanley, my mom, dad, sister and brother - for always believing in me and supporting my dreams. Thank you to my friends, peers, and mentors for the support along the way. To those who have lended a listening ear, given me kind words or advice, I am thankful. Your encouragment inspired me to keep pushing through, especially when times were tough.

Lastly, I am thankful for my daughter, Maddie, who has given me strength and inspiration. Obstacles and adversity are often easier to overcome when you are motivated by someone other than yourself. I'm looking forward to a lifetime of fun and adventures with you. Thank you for being the light of my life.

TABLE OF CONTENTS

LIST OF TABLES

LIST OF FIGURES

x

LIST OF SYMBOLS

x, y, z = position components of the quadrotor in the inertial frame (m)

ϕ, θ, ψ = Euler roll, pitch, and yaw quadcopter components (rad)

u, v, w = translational velocity components (m/s)

p, q, r = angular velocity components (rad/s)

$\mathbf{T}_{I/B}$ = transformation matrix for inertial to body frame

X, Y, Z = force components vector in the body frame (N)

L, M, N = moment components vector in the body frame (N-m)

$\mathcal{S}()$ = skew symmetric cross product operator

$\tau_\phi, \tau_\theta, \tau_\psi$ = roll, pitch, and yaw torques in the body frame (N-m)

Ω_i = angular velocity of the ith quadcopter rotor (rad/s)

f_i = upward force of the ith quadcopter rotor (N)

R = uniform quadcopter rotor radius (m)

m = mass of the quadcopter (kg)

g = gravitational constant (m/s^2)

C_T = thrust factor

C_Q = momentum factor

F_T = total thrust applied to the quadrotor (N)

ABSTRACT

Schibelius, Lisa M., M. S., University of South Alabama, May, 2018. Utilizing Unmanned Aerial Vehicles for Atmospheric Data Acquisition. Chair of Committee: Carlos J. Montalvo, Ph.D.

Unmanned aerial vehicles (UAVs) are an emerging platform for observing the atmospheric boundary layer (ABL), which is the lowest layer of the Earth′s atmosphere. Quadrotors are a type of rotary UAV which provide high controllability and vertical take-off and landing (VTOL) capabilities, allowing for targeted measurements and vertical profiling of the ABL. Obtaining atmospheric parameters using rotary UAVs still faces problems however, such as sensor accuracy, vibration noise, and effects of measuring data on moving aircraft. This work focuses on establishing an accurate method for wind parameter estimation using pitot-static tubes and cup-anemometers on board rotary UAVs. A mobile atmospheric sensing system (MASS) is designed for pressure, temperature, relative humidity, wind speed and direction measurements using a commercially available aircraft and a custom-built pitot-static array. Sensors are validated using wind tunnel testing and flights next to a Mesonet tower. The ability for multiple UAVs to accurately sample a realistic 3D wind field is evaluated experimentally and in simulation using quadrotors and fixed-wing aircraft.

CHAPTER I

INTRODUCTION

Several methods and techniques exist for measuring the atmospheric boundary layer (ABL), which is the lowest part of the Earth's atmosphere. It extends up to 1-2 km above the surface of the Earth (about 1% of the atmosphere) and hosts turbulent winds and physical processes that are important to weather forecasting [1]. The ABL can be measured indirectly via remote sensing or directly using instruments equipped on meteorological towers, weather balloons and aircraft. Remote sensing with the utilization of ground-based, flight-based and satellite-based instruments can be expensive and is better suited for obtaining spatial averages than in situ data [2,3]. While meteorological towers provide stable measurements over long periods of time, they are limited in their ability to make targeted in situ measurements and most structures are less than 100 m in height [3]. Contrarily, weather balloons are more versatile, capable of reaching altitudes upwards of 40 km, but are expendable and strongly influenced by the mean atmospheric winds, limiting their potential for targeted measurements [4]. Weather balloons can be used recurrently when tethered, but move through the atmosphere rapidly, restricting the resolution for vertical measurements [5]. Unmanned aerial vehicles (UAVs) have recently been developed for more accessible use in commercial and various other applications. With photogrammetry and video filming capabilities, quadrotors have been used for bridge inspections, for example, among other civil applications, for preventive maintenance [6]. Quadrotors have been used in many applications to improve efficiency, or to mitigate the risks for the operator in a task or environment.

1

For bridge inspections, the quadrotor can investigate areas during high-traffic hours or areas that are difficult to access. Only recently have UAVs been used for atmospheric applications, with the first meteorological sampling with a UAV in the 1960's [7]. They are being utilized in atmospheric and environmental applications specifically with work done by Roldan on measuring greenhouse parameters and Kiefer on fire plume monitoring [8,9]. Quadrotors are particularly effective in capturing the vertical distribution of parameters in the ABL and acquiring hyper-local atmospheric data with their ability to be actively controlled and to hover in flight. The utilization of UAVs for atmospheric measurements in the ABL allows for targeted measurements that are not attainable by piloted aircraft [10].
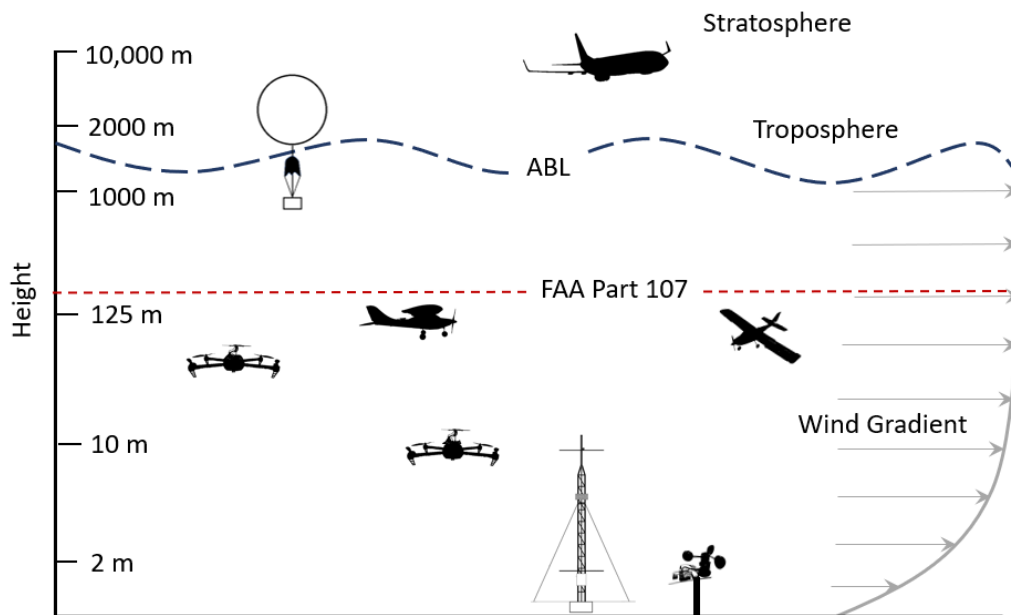
Figure 1. Various wind measurement devices

The atmosphere can be sampled directly using UAVs such as quadrotors and fixed-wing aircraft with absolute sensors such as pitot-static tubes or indirectly with inertial measurements which use subtractive algorithms to estimate atmospheric

2

winds by comparing an aircraft model with no external disturbances to a measured output [11, 12]. The ability to use the quadrotor to estimate wind speed and direction using only a global positioning system (GPS) and inertial measurement unit (IMU) saves valuable payload for the UAV; however, it requires extensive knowledge of the quadrotor such as flight behavior and the effect of inclination angle on wind measurements for accurate sampling.

The proposed research presents a mobile atmospheric sensing system (MASS) for directly measuring the ABL which consists of a meteorological sensor, a flow measurement sensor for measuring wind speed and both a commercially available quadrotor and fixed-wing aircraft as the mobile platform. The design and calibration of a flow measurement sensor is detailed with emphasis on avoiding propeller downwash produced by the quadrotor. Multiple sensors for measuring wind speed on board the quadrotor are investigated such as pitot probes and cup-anemometers. Flight tests are performed alongside an on-site mesonet tower to validate the atmospheric sensing package, which consists of pressure, temperature, humidity and wind speed sensors. Four experimental test cases are performed to quantify the impacts of the mobile platform on wind estimations. The resultant estimation of atmospheric winds, U_A is dependent on several factors, including the quadrotor velocity, V_A, angular rotation, and an empirical model for the pitot probes. The sensors are calibrated using scaling factors and ground-based and flight-based correction factors. The following test cases were evaluated:

Case 1: Quadrotor stationary with no atmospheric winds

$$\vec{V_Q} = 0$$

$$\vec{V_A} = 0$$

$$U_A = 0$$

Case 2: Sensors stationary with atmospheric winds

$$\vec{V_Q} = 0$$

$$\vec{V_A} \neq 0$$

$$U_A = \|\mathbf{V_A}\|$$

Case 3: Quadrotor motion with no atmospheric winds

$$\vec{V_Q} \neq 0$$

$$\vec{V_A} = 0$$

$$U_A = \|\mathbf{V_Q}\|$$

Case 4: Quadrotor motion with atmospheric winds

This case includes the quadrotor in hover, flown in a square pattern, and soundings.

$$\vec{V_Q} \neq 0$$

$$\vec{V_A} \neq 0$$

$$U_A = \|\mathbf{V_Q}\| + \|\mathbf{V_A}\| + B_Q$$

where B_Q is a correction factor for bias from the quadrotor.

A multiple MASS (multi-MASS) simulation is used to verify the ability of a fleet of aircraft equipped with atmospheric sensors to characterize a wind field against an existing wind field model. Ultimately, the goal of this work is to investigate the ability of inexpensive sensors onboard quadrotors to sample the atmosphere. The accuracy and affordability of the sensors are summarized and experimental tests are performed to support the findings.

1.1 Background

Numerous papers have been published showing subtractive algorithms which estimate the difference between the model of an aircraft with no winds and a measured output [13]. The difference between the model and the measured output is the disturbance, which in this research is atmospheric winds. This would require a sensor-rich aircraft, but is entirely feasible with the onset of commercially available electronics. In the work done by Neumann and Bartholmai, this method was experimentally tested with an AirRobot quadrotor which uses only the IMU

and GPS for wind vector estimation [14]. The disadvantage with this technique is that it requires wind tunnel testing to determine a relationship between quadrotor inclination angle and wind speed. This method is promising in the estimation of wind speed, but accuracy is low in estimation of wind direction with a root-mean-square error (RMSE) between 14.77° and 31.66° in flight [14]. Pitot probes and anemometers have advantages in sampling the atmosphere in that they are direct methods that do not require any prior aircraft wind tunnel testing and are platform transferable. Historically, to estimate wind parameters, pitot probes have been used onboard fixed-wing aircraft while anemometers have been used on static towers [15]. Pitot probes work well on fixed-wing aircraft since the inflow of wind during flight is high, providing a large pressure differential. Coupled with GPS, the effect of groundspeed from the absolute sensor measurement is subtracted to obtain the local atmospheric disturbance [13]. At low wind speeds however, pressure differences are small, requiring sensitive sensors for accurately measuring wind speed with a pitot probe [16]. This poses difficulty for estimating wind speed using pitot probes on quadrotors while they are in hover or moving at slow speeds, but can potentially be overcome with sensitive sensors, calibration, data processing and sensor aspiration. The use of commercially available anemometers on board UAVs is the most recent development for wind speed measurement on rotary UAVs. In the 2017 work done by Palomaki et. al, a 2D sonic anemometer was flown on a hexacopter and compared to an indirect method for wind estimation using a quadrotor [17]. Results conclude that at low wind speeds, the RMSEs were comparable to the work done by Neumann and Batholmai, with slightly better estimations using the indirect method. In the work done by Bruschi, et. al, a novel MEMS-based (microelectromechanical systems) 2D anemometer was designed for estimating wind speed specifically on a quadrotor. Testing the sensor onboard the quadrotor indicates that the effects of the propellers only significantly impact

5

estimated wind speed measurements below 10 m/s [18]. However, the effects of the propellers on wind speed measurements are directly influenced by the location of the sensor and distance from the turbulent propwash. Given their size, weight and location requirements onboard a quadrotor, anemometers are not a popular method for measuring wind speed on UAVs, but could potentially provide accurate wind measurements. In addition to sampling atmospheric winds using either inertial or absolute measurement devices, equipping a portable platform with pressure, temperature and humidity sensors results in a sophisticated mobile atmospheric sensing system, which is ultimately the aim of this work.

Although several techniques exist for wind field estimation, the utilization of multiple UAVs is a relatively new approach. Given the spatial and temporal variation of a three-dimensional atmospheric wind field, it is difficult to quantify, analyze and visualize data that is gathered. To overcome this, a fleet of aircraft can be used to obtain real-time wind data, generating an atmospheric wind model more efficiently and accurately than a single aircraft, which is only able to sample data in its local frame. The use of weather reconnaissance devices such as dropsondes to sample cyclones in real-time have been used, but are unguided, resulting in a sample space that is largely governed by the local atmosphere [19]. The newly developed Raytheon Coyote UAV, however, combines the controllability of UAVs and expendability of dropsondes. Shown in Figure 2, it is dropped from an aircraft, deploys its wings and propeller, self-propels, and is able to acquire real-time data of the atmosphere for up to one hour [20]. These unmanned systems have been deployed in hurricanes to acquire data in areas that are too dangerous for piloted aircraft. Multiple Coyote systems have even been operated as a swarm. The greatest disadvantage to these is that the sonobuoy tube must be dropped from an aircraft, and the unmanned system is expendable.

6

Figure 2. Raytheon Coyote UAV

The potential for recreating a windfield has been explored previously in simulation using multiple UAVs with data processed through a radial basis function to recreate a wind field [21]. Green's function was also used in simulation to recreate a wind field with limited data measurements from UAVs [22]. The current project seeks to validate the simulated theoretical test case in this work by acquiring physical atmospheric data to test in simulation to verify this method.

Although quadrotors offer a recoverable means for atmospheric data acquisition, wind measurements using UAVs still faces problems, and an accurate method for obtaining atmospheric data using rotary UAVs has not yet been established. For direct wind sensors measurement methods, one obstacle is the avoidance of the quadrotor propeller downwash from the spinning rotors. The turbulent downwash would impact wind speed measurements, so any direct sensor for measuring wind speed or direction must be outside of the influence of the downwash. Wind speed measurement sensors also face vibration issues while the quadrotor is in hover. Even with inertial-based methods for estimating wind speed and direction, there are limitations to accuracy based on the aircraft model, IMU and GPS.

7

Motivation for developing the MASS is to observe sea breezes (SBs) and bay breezes (BBs) in the Mobile Bay area, which have several environmental impacts. The mobile platform allows for targeted measurements - rather than those supplied by fixed meteorological towers or weather stations - providing beneficial meteorological data. The sea breeze is a meteorological phenomenon that occurs along coasts of large bodies of water like the Gulf Coast. The wind of a sea breeze moving inland from the body of water is caused by differences in air pressure and heating capacities between the land and sea [23]. Sea breezes commonly occur in the Mobile Bay region between the months of May and October. Shown in Figure 3 is a radar reflectivity image of a sea-breeze front along the Gulf Coast in Mobile, Alabama provided by the KMOB weather surveillance radar (WSR)-88D at 20:33:03 UTC, 6 August 2010 [24].
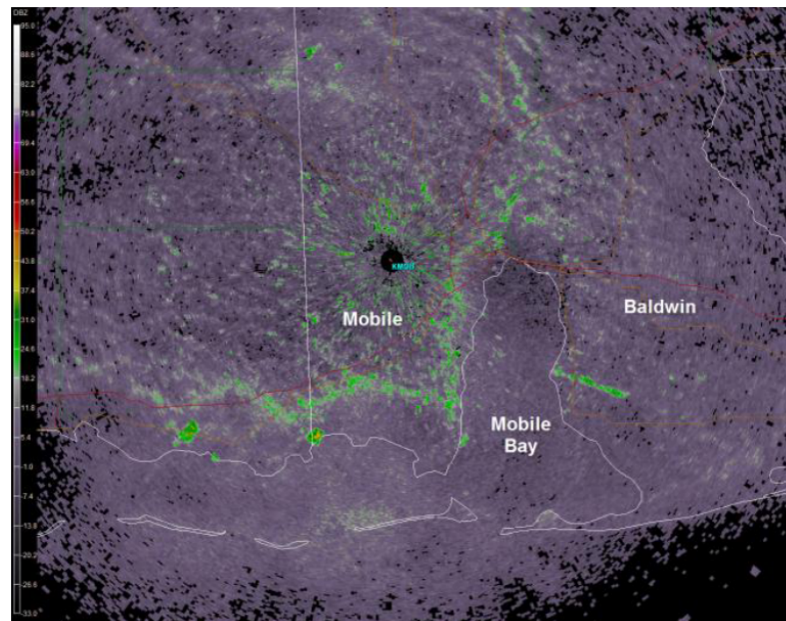
Figure 3. Radar reflectivity image showing a sea/bay breeze in Mobile, AL

When occurring in areas of high atmospheric humidity, sea breezes can cause severe thunderstorms. Understanding and forecasting the SB structure and its effect on weather conditions is critical for the safety and well-being of coastal residents [24]. Hyper-local data in the lower atmospheric boundary layer obtained using the MASS can be used to improve understanding of SB/BB interaction and SB/BB-generated convective activity. Furthermore, this data acquired using the MASS can be assimilated into the Weather Research and Forecasting model (WRF), which is a numerical weather prediction model [25]. Considering the cooperative outlook of multi-MASS, missions can be performed to survey an area with cameras or other devices, such as sampling hazardous gases to model propagation of airborne chemicals. Future applications will still be uncovered as technology develops. The focus of this work, however, is on the analysis and development of an accurate wind sensor for use on rotary UAVs, and the multi-MASS method is tested in simulation.

1.3 Contributions of Thesis

Unlike recent research and technology utilizing inertial-based measurements for wind speed measurements, the MASS presented here is relatively inexpensive and portable across different platforms. This type of system is useful for applications where the aircraft system has not been tested in a wind tunnel to determine characteristics unique to the aircraft model. In this thesis, the problem of obtaining wind speed data on a quadrotor using direct sensors is addressed. Contributions of this thesis include:

1. Created concept of operations for multi-MASS experiment
2. Analysis of wind speed measurement capabilities for VTOL aircraft
3. Development of an inexpensive, portable weather station on a mobile platform

9

4. Calibration of sensors, including vibration reduction and wind speed and direction extraction from a pitot-static tube array

CHAPTER II
SIMULATION

Multiple fixed-wing aircraft and quadrotors are simulated using standard rigid body dynamics and inner loop-outer loop control laws. A radial basis function approximation is used to reproduce a wind field from the sampled data of the aircraft in a modeled atmosphere. The aim of the simulation is to expand on the work done by Montalvo et. al. and to simulate multiple UAVs in a realistic 3D wind field. This includes the incorporation of quadrotors in the Multi-agent Atmospheric Wind Mapper (MaAWM) tool, rather than just the use of fixed-wing aircraft [26]. This section presents the dynamic models used for aircraft simulation and analysis, which include the fixed-wing aircraft aerodynamic model, quadrotor aerodynamic model, aircraft control systems, and the Weather Research and Forecasting (WRF) model.

2.1 Flight Dynamics

Mathematical models for the quadrotor and fixed-wing aircraft dynamics are detailed in this section. Each aircraft in the simulation is modelled independently and is excited by gravitational and aerodynamics forces and moments.

2.1.1 Quadrotor Dynamic Model

Two reference frames are used to describe the orientation of the quadrotor: the inertial reference frame, which is fixed to the ground, and the body reference frame,

11

which is fixed to the quadrotor. The quadrotor is able to translate and rotate about three axes with six degrees of freedom. The body frame axes are denoted by $\bar{X}_B$, $\bar{Y}_B$, and $\bar{Z}_B$. The quadrotor is powered by four motors with two rotors spinning clockwise and two spinning counter-clockwise, as shown in Figure 4.
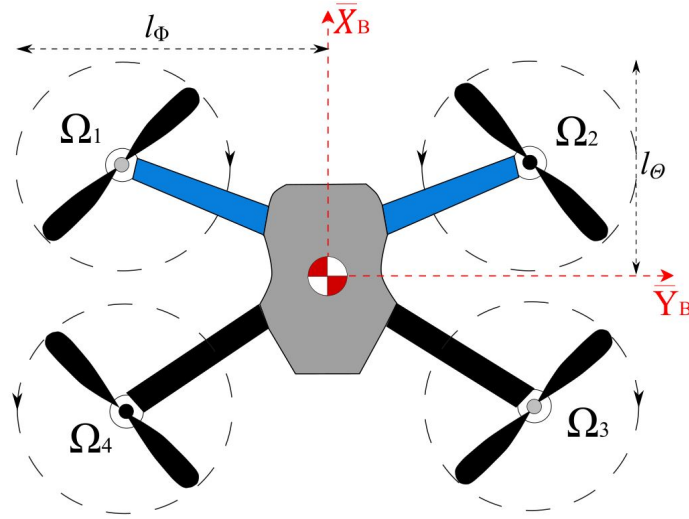
Figure 4. Top down view of the quadrotor with body reference frame.

The quadrotor kinematic equations of motion are taken about the mass center of the quadrotor with the body reference frame aligned using standard aerospace convention. A standard rigid structure is assumed, along with roll symmetry and rotors that are rigid in the orthogonal plane to the body z-axis. The transformation matrix, $\mathbf{T}_{I/B}$, relates the quadrotor body reference frame to the inertial reference frame velocity components as shown in Equation 1.

$$\begin{Bmatrix} \dot{x} \\ \dot{y} \\ \dot{z} \end{Bmatrix} = [\mathbf{T}_{I/B}] \begin{Bmatrix} u \\ v \\ w \end{Bmatrix} \tag{1}$$

12

Trigonometric functions are shorthanded using standard notation: $cos(\alpha) \equiv c_\alpha$, $sin(\alpha) \equiv s_\alpha$, and $tan(\alpha) \equiv t_\alpha$.

$$\mathbf{T}_{I/B} = \begin{bmatrix} c_\theta c_\psi & s_\phi s_\theta s_\psi - c_\phi s_\psi & c_\phi s_\theta c_\psi + s_\phi s_\psi \\ c_\theta s_\psi & s_\phi s_\theta s_\psi + c_\theta c_\psi & c_\phi s_\theta s_\psi - s_\phi c_\psi \\ -s_\theta & s_\phi c_\theta & c_\phi c_\theta \end{bmatrix} \tag{2}$$

The **H** matrix, shown in Equation 3, relates the body angular velocity components to the time derivative of the Euler angles.

$$\begin{Bmatrix} \dot{\phi} \\ \dot{\theta} \\ \dot{\psi} \end{Bmatrix} = \begin{bmatrix} 1 & s_\phi t_\theta & c_\phi t_\theta \\ 0 & c_\phi & -s_\phi \\ 0 & s_\phi/c_\theta & c_\phi/c_\theta \end{bmatrix} \begin{Bmatrix} p \\ q \\ r \end{Bmatrix} \tag{3}$$

The dynamic equations are formed by summing forces and moments about the system center of mass of the system in the body reference frame and equating the result to the time derivative of linear and angular momentum. The translational and rotational dynamic equations of motion are expressed below.

$$\begin{Bmatrix} \dot{u} \\ \dot{v} \\ \dot{w} \end{Bmatrix} = \frac{1}{m} \begin{Bmatrix} X \\ Y \\ Z \end{Bmatrix} - \mathbf{S}(\vec{\omega}_{I/B}) \begin{Bmatrix} u \\ v \\ w \end{Bmatrix} \tag{4}$$

$$\begin{Bmatrix} \dot{p} \\ \dot{q} \\ \dot{r} \end{Bmatrix} = [I]^{-1} \left(\begin{Bmatrix} L \\ M \\ N \end{Bmatrix} - \mathbf{S}(\vec{\omega}_{I/B})[I] \begin{Bmatrix} p \\ q \\ r \end{Bmatrix} \right) \tag{5}$$

The skew symmetric operator is denoted by $\mathbf{S}()$, which is equivalent to a cross product when multiplied by a vector.

$$\mathbf{S}(\vec{\omega}_{I/B}) = \begin{bmatrix} 0 & -r & q \\ r & 0 & -p \\ -q & p & 0 \end{bmatrix} \tag{6}$$

The mass moment of inertia matrix is denoted as I.

$$I = \begin{bmatrix} I_{xx} & 0 & -I_{xz} \\ 0 & I_{yy} & 0 \\ -I_{xz} & 0 & I_{zz} \end{bmatrix} \tag{7}$$

For the quadrotor rotational dynamics, the standard body aerodynamic moment will consider aerodynamics created by the rotor torque. The total external moments are given by input torques, $\vec{\tau}$, and gyroscopic torques, $\vec{\Gamma}$.

$$\begin{Bmatrix} L \\ M \\ N \end{Bmatrix} = \begin{Bmatrix} \tau_\phi \\ \tau_\theta \\ \tau_\psi \end{Bmatrix} + \begin{Bmatrix} \Gamma_x \\ \Gamma_y \\ \Gamma_z \end{Bmatrix} \tag{8}$$

The input torque derivation starts with defining thrust per rotor, f_i, which is dependent on the angular velocity of the ith rotor, Ω_i, the rotor radius, R, the thrust factor, C_T, and the density of air, ρ.

$$f_i = C_T \frac{4\rho R^4}{\pi^2} \Omega_i{}^2 \tag{9}$$

14

The input torque per rotor, τ_i, is dependent on the angular velocity of the ith rotor and the blade drag factor, b, which is defined in Equation 11. Note that the torque applied to r_1 and r_3 are positive and r_2 and r_4 are negative.

$$\tau_i = b\Omega_i{}^2(-1^{i+1}) \tag{10}$$

The blade drag factor is a function of the rotor radius, the density of air and the momentum factor, C_Q.

$$b = C_Q\frac{4\rho R^5}{\pi^3} \tag{11}$$

The blade drag factor, thrust factor and momentum factor are assumed to be constant throughout flight for Equation (9 - 11) to be valid. These constants result from the momentum theory of blade elements [27]. Knowing τ_i, relations for τ_ϕ, τ_θ and τ_ψ can be written as

$$\begin{aligned}
\tau_\phi &= l_\phi[(f_2 + f_3) - (f_1 + f_4)] \\
\tau_\theta &= l_\theta[(f_1 + f_2) - (f_3 + f_4)] \\
\tau_\psi &= \tau_1 + \tau_2 + \tau_3 + \tau_4
\end{aligned} \tag{12}$$

The lengths from the rotor axis to the positive body frame axes for roll and pitch are denoted as l_ϕ and l_θ, respectively. These lengths are shown in Figure 4 along with the rotors labeled as Ω_1, Ω_2, Ω_3, and Ω_4. The relations in Equation 12 are based on the required angular velocities of each rotor for a positive Euler angle, which are summarized in Equation 13. A positive roll angle, ϕ, is achieved when the right front and right back rotors, r_2 and r_3, rotate faster than the left front and left

15

back rotors, r_1 and r_4.

$$\phi^+ : \Omega_2 = \Omega_3 > \Omega_1 = \Omega_4$$
$$\theta^+ : \Omega_1 = \Omega_2 > \Omega_3 = \Omega_4 \tag{13}$$
$$\psi^+ : \Omega_1 = \Omega_3 > \Omega_2 = \Omega_4$$

The gyroscopic torques due to the rotors are defined as

$$\begin{Bmatrix} \Gamma_x \\ \Gamma_y \\ \Gamma_z \end{Bmatrix} = I_r \mathbf{S}(\vec{\omega}_{I/B}) \begin{Bmatrix} 0 \\ 0 \\ \Omega_r \end{Bmatrix} = \begin{Bmatrix} I_r \Omega_r q \\ -I_r \Omega_r p \\ 0 \end{Bmatrix} \tag{14}$$

where $\Omega_r = \Omega_1 - \Omega_2 + \Omega_3 - \Omega_4$, I_r is the moment of inertia about the rotor axis and Ω_r is the relative rotor speed. The total external forces acting on the quadrotor body are given by the force of gravity from weight, mg, total rotor thrust, F_T, and aerodynamic drag, $\{X_A, Y_A, Z_A\}^T$.

$$\begin{Bmatrix} X \\ Y \\ Z \end{Bmatrix} = \mathbf{T}_{I/B} \begin{Bmatrix} 0 \\ 0 \\ mg \end{Bmatrix} - \begin{Bmatrix} 0 \\ 0 \\ F_T \end{Bmatrix} + \begin{Bmatrix} X_A \\ Y_A \\ Z_A \end{Bmatrix} \tag{15}$$

The total thrust, F_T, is simply the sum of the thrust per rotor for each of the four rotors.

$$F_T = \sum_{i=1}^{4} f_i \tag{16}$$

Thrust of the rotors causes aerodynamic drag on the quadrotor due to both rotor flapping and lift-induced drag [28]. While the quadrotor is in motion, flexibility of

16

the rotors results in rotor flapping, which is a function of advance ratio, μ and is dependent on the rotors and hub design [29], as shown in Equation 17.

$$\mu = \frac{\sqrt{u^2 + v^2}}{\eta}$$
$$\eta = \sum_{i=1}^{4} \Omega_i R \tag{17}$$

Asymmetry of lift for the quadrotor is caused by an imbalance in the thrust produced by advancing and retreating rotors, resulting in lift-induced drag. The total aerodynamic drag is then expressed in Equation 18.

$$\begin{Bmatrix} X_A \\ Y_A \\ Z_A \end{Bmatrix} = -F_T \begin{Bmatrix} \left(\frac{A_{1c}}{\eta} + d_x\right) u - \frac{A_{1s}}{\eta} v \\ \frac{A_{1s}}{\eta} u + \left(\frac{A_{1c}}{\eta} + d_y\right) v \\ 0 \end{Bmatrix} \tag{18}$$

where d_x, and d_y are induced drag coefficients and A_{1s}, and A_{1c} are positive coefficients that describe the rotor flapping response.

2.1.2 Fixed-Wing Dynamic Model

Similar to the quadrotor dynamic model, the fixed-wing aircraft model uses standard rigid body dynamics to represent aircraft motion [30]. Kinematic equations of motion are taken about the mass center of the aircraft. The transformation matrix, $\mathbf{T}_{I/B}$, relates the aircraft body reference frame to the inertial reference frame, as shown in the previous section in Equation 41.

$$\begin{Bmatrix} \dot{x} \\ \dot{y} \\ \dot{z} \end{Bmatrix} = [\mathbf{T}_{I/B}] \begin{Bmatrix} u \\ v \\ w \end{Bmatrix} \tag{19}$$

17

Modelling multiple aircraft, the transformation matrix relates the ith aircraft body reference frame to the inertial frame, while the $\mathbf{H}_i$ matrix relates the body angular velocity components to the time derivative of the Euler angles, as shown in Equation 20.

$$\begin{Bmatrix} \dot{\phi}_i \\ \dot{\theta}_i \\ \dot{\psi}_i \end{Bmatrix} = [\mathbf{H}_i] \begin{Bmatrix} p_i \\ q_i \\ r_i \end{Bmatrix} = \begin{bmatrix} 1 & s_{\phi_i} t_{\theta_i} & c_{\phi_i} t_{\theta_i} \\ 0 & c_{\phi_i} & -s_{\phi_i} \\ 0 & s_{\phi_i}/c_{\theta_i} & c_{\phi_i}/c_{\theta_i} \end{bmatrix} \begin{Bmatrix} p_i \\ q_i \\ r_i \end{Bmatrix} \tag{20}$$

The dynamic equations are formed by summing forces and moments about the system mass center in the body reference frame and equating the result to the time derivative of linear and angular momentum. The translational and rotational dynamic equations of motion are expressed below.

$$\begin{Bmatrix} \dot{u}_i \\ \dot{v}_i \\ \dot{w}_i \end{Bmatrix} = \frac{1}{m_i} \begin{Bmatrix} X_i \\ Y_i \\ Z_i \end{Bmatrix} - \mathbf{S}(\vec{\omega}_{i/I}) \begin{Bmatrix} u_i \\ v_i \\ w_i \end{Bmatrix} \tag{21}$$

$$\begin{Bmatrix} \dot{p}_i \\ \dot{q}_i \\ \dot{r}_i \end{Bmatrix} = [I_i]^{-1} \left(\begin{Bmatrix} L_i \\ M_i \\ N_i \end{Bmatrix} - \mathbf{S}(\vec{\omega}_{i/I})[I_i] \begin{Bmatrix} p_i \\ q_i \\ r_i \end{Bmatrix} \right) \tag{22}$$

The skew symmetric operator is given in Equation 6. The mass moment of inertia matrix I_i is taken about the center of gravity of the aircraft and is positive definite and symmetric. The applied forces and moments expressed in Equation 21 and 22

18

contain contributions from weight *(W)*, and aerodynamics *(A)*. The total forces applied to the aircraft expressed in the body reference frame are given below.

$$\begin{Bmatrix} X_i \\ Y_i \\ Z_i \end{Bmatrix} = \begin{Bmatrix} X_W + X_A \\ Y_W + Y_A \\ Z_W + Z_A \end{Bmatrix} \tag{23}$$

The weight contribution is given by equation (24).

$$\begin{Bmatrix} X_W \\ Y_W \\ Z_W \end{Bmatrix} = m_i g \begin{Bmatrix} -s_{\theta_i} \\ s_{\phi_i} c_{\theta_i} \\ c_{\phi_i} c_{\theta_i} \end{Bmatrix} \tag{24}$$

The aerodynamic force for all lifting surfaces on the body are determined using aerodynamics expansion [30].

$$\begin{Bmatrix} X_A \\ Y_A \\ Z_A \end{Bmatrix} = \frac{1}{2} \rho V_\infty^2 S \begin{Bmatrix} C_L s_\alpha - C_D c_\alpha + C_{x_{\delta_t}} \delta_t \\ C_{y\beta}\beta + C_{y\delta_r}\delta_r + \frac{b}{2V_\infty} C_{yp} p \\ -C_L c_\alpha - C_D s_\alpha \end{Bmatrix} \tag{25}$$

Where the lift and drag coefficients are:

$$\begin{Bmatrix} C_L \\ C_D \end{Bmatrix} = \begin{Bmatrix} C_{L0} + C_{L\alpha}\alpha + \frac{c}{2V_\infty} C_{Lq} q + C_{L\delta_e}\delta_e \\ C_{D0} + C_{D\alpha}\alpha^2 + C_{Du} u_a \end{Bmatrix} \tag{26}$$

Using the aircraft velocity with respect to atmospheric winds it is possible to compute the total velocity, angle of attack and sideslip.

$$V_\infty = \sqrt{u_a^2 + v_a^2 + w_a^2} \tag{27}$$

$$\alpha = tan^{-1}\left(\frac{w_a}{u_a}\right) \tag{28}$$

19

$$\beta = sin^{-1}\left(\frac{v_a}{V_\infty}\right) \tag{29}$$

It should be noted that these velocities include the components of atmospheric winds.

$$\begin{Bmatrix} u_a \\ v_a \\ w_a \end{Bmatrix} = \begin{Bmatrix} u_i \\ v_i \\ w_i \end{Bmatrix} + \mathbf{T}^T{}_{IB_i} \begin{Bmatrix} V_x \\ V_y \\ V_z \end{Bmatrix} \tag{30}$$

The body aerodynamic moment is also computed using an aerodynamic expansion.

$$\begin{Bmatrix} L_A \\ M_A \\ N_A \end{Bmatrix} = \frac{1}{2}\rho V_\infty{}^2 Sc \begin{Bmatrix} C_{l\beta}\beta + \frac{b}{2V_\infty}(C_{lp}p + C_{lr}r) + C_{l\delta_a}\delta_a + C_{l\delta_r}\delta_r \\ C_{m0} + C_{m\alpha}\alpha + \frac{c}{2V_\infty}C_{mq}q + C_{mu}u_a + C_{m\delta_e}\delta_e \\ \frac{b}{2V_\infty}(C_{np}p + C_{nr}r) + C_{n\beta}\beta + C_{n\delta_a}\delta_a + C_{n\delta_r}\delta_r \end{Bmatrix} \tag{31}$$

The aerodynamic coefficients in Equations 25, 26 and 31 can be obtained from flight data, aerodynamic modeling and wind tunnel testing.

2.2 Aircraft Control Systems

The control systems for the quadrotor and fixed-wing aircraft are detailed in this section. Each aircraft utilizes standard PID tracking control with conventional inner loop-outer loop control laws.

2.2.1 Quadrotor Control System

In order to control and stabilize the quadrotor system, feedback and proportional-derivative control are added. The standard PID controller repeatedly computes an error value, which is the difference between a measured value and a desired setpoint value. This error value is minimized over time with the use of the three functions, where proportional control tracks present values of the error,

integral control tracks past values of the error, and derivative control tracks potential future values of the error [31]. To maintain the quadrotor in hover, a desired altitude, z_c is chosen as the setpoint, and the error value is calculated as the difference between the measured quadrotor altitude and setpoint altitude. Proportional and derivative control are used to adjust the input angular velocity to the system to apply thrust to the quadrotor to hover at the desired setpoint. The proportional and derivative gains, k_p and k_d, respectively, are tuned to minimize settling time and overshoot of the system.

The quadrotor shown in Figure 4 is controlled by the rotational speed of the four propeller blades. The altitude of the quadrotor in the $\bar{Z}_B$ axis is controlled by applying an equal amount of thrust to all four rotors. To control the roll of the quadrotor, the front left and back left rotors must have a higher rotational speed, Ω, than the front right and back right rotors for a positive roll. For a positive pitch of the quadrotor, the front two rotors must have a higher speed than the back two rotors. For a positive yaw of the quadrotor, the front right and back left rotors must have a higher speed than the front left and back right rotors. For example, to impose a positive roll angle, ϕ, on the quadrotor, rotors two and three must rotate faster than rotors one and four. The relations between the rotors and controlling axes are described in Equation 13.

A quadrotor has an inertial measurement unit (IMU) to determine the orientation of the quadrotor using an accelerometer, gyroscope and magnetometer. The measured roll, pitch and yaw angles from the IMU are denoted as $\tilde{q}$

$$\tilde{q} = \begin{Bmatrix} \tilde{\phi} \\ \tilde{\theta} \\ \tilde{\psi} \end{Bmatrix}$$

Three input variables ϕ_c, θ_c, and ψ_c, for roll, pitch and yaw angle, respectively, can be used to control the orientation of the quadrotor. By comparing these values to

21

the measured values from the IMU, three error signals, ϕ_e, θ_e, and ψ_e are established, which are fed into the proportional and derivative control. The outer loop block diagram in Figure 5 utilizes x_c and y_c, the desired x coordinate and y coordinate position of the quadrotor, to determine the desired input roll, pitch and yaw angles based on the current position of the quadrotor that is determined by the GPS. The error signal that is determined by comparing the desired position to the measured position is fed into proportional and derivative control, yielding the desired roll pitch and yaw angles that are inputted into the inner loop in Figure 6.
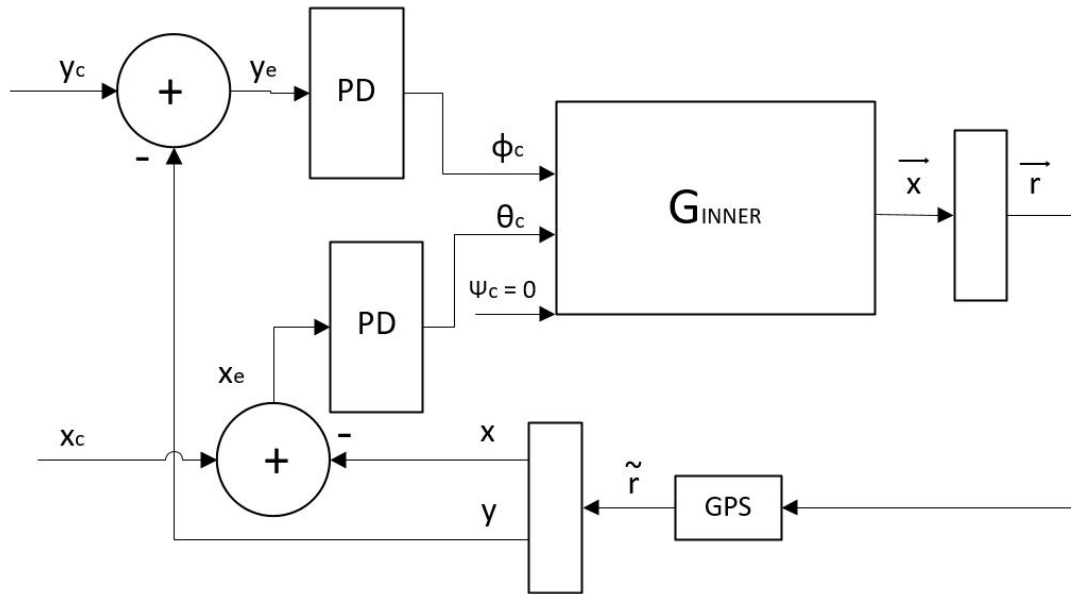
Figure 5. Outer loop block diagram for the quadrotor system

The yaw angle command, ψ_c, is set to zero because applying yaw to the quadrotor does not directly change the x and y position of the quadrotor. The input $\vec{u}$ to the quadrotor is

$$\vec{u} = \left\{ \Omega_1 \quad \Omega_2 \quad \Omega_3 \quad \Omega_4 \right\}^T$$

22

Furthermore, the inner loop utilizes proportional and derivative control based on the error signal obtained from the measured roll, pitch and yaw angles from the IMU and the desired roll, pitch and yaw angles that are inputted from the outer loop. Either a positive or negative signal will then be sent to each of the four rotors.
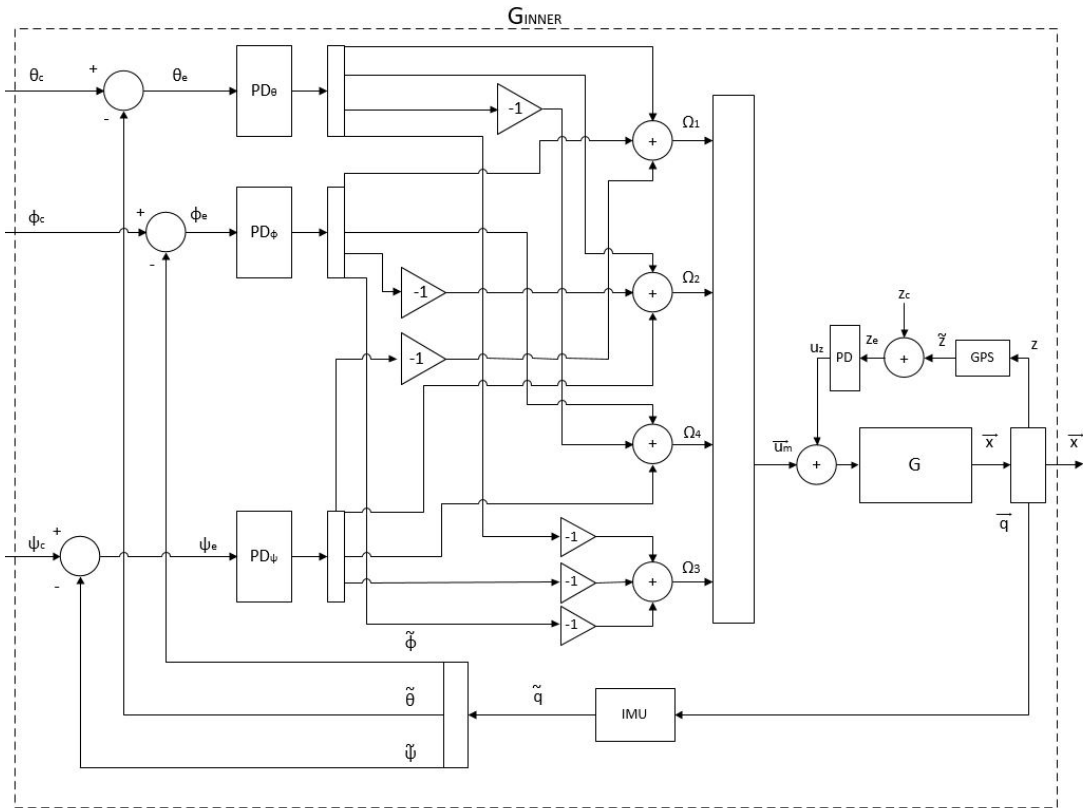
Figure 6. Inner loop block diagram for the quadrotor system

The quadrotor can be programmed to navigate to a single desired waypoint or navigate to multiple waypoints in a pre-determined flight path. To simulate the quadrotor flying waypoints, each of the individual controllers for x, y, z, ϕ, θ and ψ must be established with commanded values and controller gains. The proportional and derivative controller gains for each state are tuned for adequate response time of the system and are summarized in Table 1.

23

Table 1. PD Controller gain values for individual z, ϕ, θ and ψ control

Controller gain	Value
k_{pz}	4.8
k_{dz}	21
$k_{p\phi}$	0.5
$k_{d\phi}$	0.8
$k_{p\theta}$	0.9
$k_{d\theta}$	1.2
$k_{p\psi}$	0.34
$k_{d\psi}$	1.9

The waypoint nagivation controller begins with establishing an altitude hold algorithm to command the quadrotor to a desired altitude to remain in hover. The angular velocity of the four rotors are kept equal for level ascent, and the change from the nominal angular velocity of Ω_0 to Ω for each rotor is governed by the error signal obtained from the difference between the commanded altitude and the current altitude times proportional gain and the difference between the velocity command of zero and the current velocity times derivative gain, illustrated in Equation 32.

$$\Omega = \Omega_0 - k_{pz}(z_c - z) - k_{dz}(0 - \dot{z}) \tag{32}$$

Utilizing altitude hold, roll, pitch and heading controllers, the quadrotor can be programmed to fly single and multiple waypoints. For waypoint control, the controller gains from the individual roll, pitch, yaw and altitude controllers are adjusted for a faster settling time. The updated controller gains for waypoint navigation are shown in Table 2. The inner loop controller gains must result in a settling times for ϕ, θ and ψ that is five times faster than the settling times for the

x, y and z positions. This results in a system with a total response that is similar to that of a pure second order system [32].

Table 2. PD Controller gain values for waypoint navigation

Controller gain	Value
k_{px}	0.121
k_{dx}	0.24
k_{py}	0.095
k_{dy}	0.0008
k_{pz}	15
k_{dz}	150
$k_{p\phi}$	100
$k_{d\phi}$	12
$k_{p\theta}$	100
$k_{d\theta}$	15
$k_{p\psi}$	150
$k_{d\psi}$	40

2.2.2 Fixed-Wing Control System

The control scheme utilized for the fixed-wing aircraft is a conventional inner loop-outer loop control law using a PID tracking controller. Waypoint commands, x_c, y_c, z_c, are needed to control each aircraft path, which can include sinusoidal and square patterns, as well as obstacle avoidance. The outer loop commands are given

25

by the control surface commands of the rudder, elevator and aileron, shown in
Equation 33.

$$\delta_{r_i} = -K_v v_i$$
$$\delta_{e_i} = K_p(\theta_i - \theta_c) + K_d \dot{\theta}_i \tag{33}$$
$$\delta_a = K_p(\phi - \phi_c) + K_d \dot{\phi}$$

A saturation block is included to avoid a signal that is sent to the control surfaces
that exceeds the limits of the control surface actuators. The Euler angle commands
ϕ_c and θ_c are set using the relationships in Equation 34, and ψ_c is determined using
the output of a potential field method [26].

$$\phi_c = K_p(\psi_i - \psi_c) + K_d \dot{\psi}_i$$
$$\theta_c = K_p(z_i - z_c) + K_d \dot{z}_i + K_I \int z_i - z_c dt \tag{34}$$

2.3 Atmospheric Model

To simulate realistic atmospheric winds, the Weather Research and Forecasting
model (WRF) is used to generate a three dimensional, time varying wind field. The
WRF model was developed from a partnership of multiple entities, including the
National Center for Atmospheric Research (NCAR) and the National Oceanic and
Atmospheric Administration (NOAA) [25]. An example vertical wind field is shown
in Figure 7 with an example flight sampling path of a fixed-wing aircraft. This wind
field was created using the WRF model at an altitude of 200 m in a 1000 m^2 area.

26
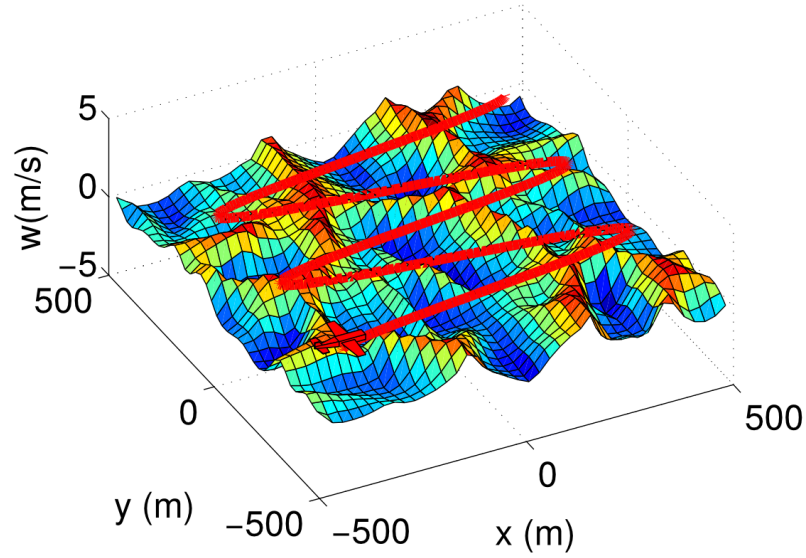
Figure 7. Example vertical wind field (m/s) with aircraft

2.4 Aircraft Simulation

Multiple aircraft are simulated to recreate a wind field using the aircraft flight models, the atmospheric model and a radial basis function (RBF) approximation. The simulation used in this research was developed by Montalvo et. al. in their 2015 work, which also details the RBF model and the Multi-agent atmospheric Wind Mapper (MaaWM) simulation [21].

2.4.1 Aircraft Parameters

Physical parameters of the Iris+ 3D Robotics quadrotor and Apprentice S15e are used for simulation, and are shown in Table 3.

The Iris+ 3D Robotics quadrotor has a cross configuration with two rotors spinning clockwise and two spinning counter-clockwise, as denoted in Figure 4. It is equipped with four brushless DC motors. The maximum angular velocity of each motor is

27

equivalent to the motor velocity constant, k_v, multiplied by the voltage, V, of the three cell lithium polymer battery that powers the quadrotor.

$$\omega_{Mmax} = k_v V \tag{35}$$

Assuming an electrical motor efficiency, n_m, of 100 percent, the electric power delivered to the motor from the battery is fully transferred to the propeller shaft. Thus, the maximum angular velocity of each propeller, ω_{Pmax} is equivalent to the maximum motor speed, ω_{Mmax}. With ω_{Mmax} estimated as 10,200 rpm, the maximum angular velocity of each propeller is about 1,100 rad/s. Physical parameters of the quadrotor system such as mass, propeller radius, thrust factor, and momentum factor are listed in Table 3. The values for thrust factor, momentum factor, induced drag coefficients, and moments of inertia that are listed were estimated for an Iris+ quadrotor by Kun and Hwang [29]. These parameters will be determined independently later.

Table 3. Physical parameters of the Iris+ quadrotor

Parameter	Value
m (kg)	1.282
l_Φ (m)	0.3302
l_Θ (m)	0.24130
r_p (m)	0.12065
K_v (rpm/V)	920
V (V)	11.1
C_T	0.05
C_Q	0.1
$I_{xx} = I_{yy}$ $(kg \cdot m^2)$	0.005
$I_{zz}(kg \cdot m^2)$	0.009
$I_r(kg \cdot m^2)$	8.8 x 10^{-5}
$A_1c = A_1s$	0.5
$d_x = d_y$	0.5

General physical parameters of the Apprentice aircraft are shown in Table 4, such as reference area, S, wingspan, b, mean chord, $\bar{c}$, and trim velocity, V_{trim}. The Apprentice longitudinal and lateral coefficients are shown in Table 5 [33,34].

29

Table 4. Physical parameters of the Apprentice fixed-wing

Parameter	Value
m (kg)	1.524
S (m^2)	0.336
b (m)	1.5
$\bar{c}$	0.224
$V_{trim}(m/s)$	20

Table 5. Apprentice aircraft longitudinal and lateral coefficients

Longitudinal	Coefficient	Lateral	Coefficient
C_{L_0}	0.062	C_{y_β}	-0.2083
C_{L_α}	5.195	$C_{y_d r}$	0.1096
C_{L_q}	4.589	C_{y_p}	0.0057
$C_{L_d e}$	0.2167	C_{y_r}	0.0645
C_{D_0}	0.028	C_{l_β}	-0.0377
C_{D_α}	1.3537	C_{l_p}	-0.4625
C_{D_u}	0	C_{l_r}	0.0288
C_{m_0}	0.0598	$C_{l_d a}$	-0.2559
C_{m_α}	-0.9317	$C_{l_d r}$	0.0085
C_{m_q}	-5.263	C_{n_β}	0.0116
$C_{m_d e}$	-0.8551	C_{n_p}	-0.0076
C_{m_u}	0	C_{n_r}	-0.0276
$C_{x_d T}$	7.6509	$C_{n_d a}$	-0.0216
$C_{m\dot{\alpha}}$	-2.897	$C_{n_d r}$	0.0035

2.4.2 Simulation

One aircraft and one quadrotor were simulated using the MaaWM tool with predetermined waypoints. The results show one aircraft flying in a spiral pattern with 81 waypoints and one quadrotor flying in the center in a sinusoidal path with 46 waypoints. The trajectories of the fixed-wing and quadrotor in the 3,000 ft^2 area are shown in Figure 8. Each aircraft samples the model atmosphere at 1 Hz using the algorithms shown in the previous sections. The data is fed into the Radial Basis Function routine to compute the basis function coefficients. Figures 9 - 12 show that the aircraft sampled winds and the actual wind data is fit very well with correlation coefficients of 0.9938, 0.9904 and 0.9942 for the U, V, and W (ft/s) wind components respectively. It should be noted that no sensor errors are included in this simulation, and the minimum amount of sensor measurements possible to obtain a fit will be determined in future work.
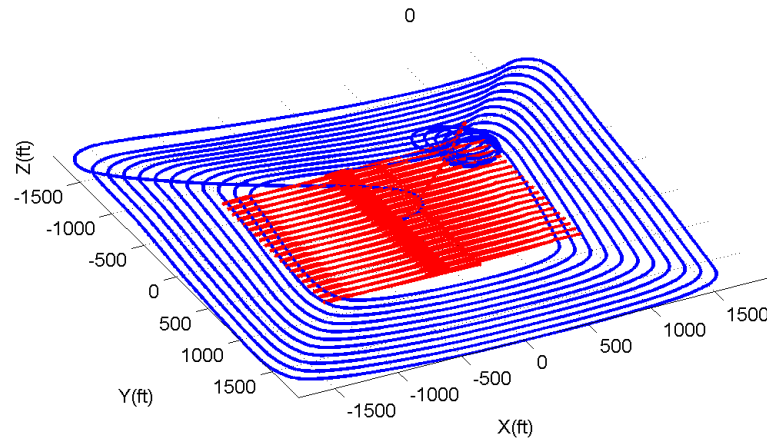
Figure 8. Trajectories of aircraft

The x component of wind speed (U ft/s) obtained from the aircraft is shown compared to the actual wind field and error in Figure 9. The wind speed error stays below 0.2 m/s almost everywhere except two small regions where the error exceeds 0.6 m/s and 0.8 m/s. These types of errors can be corrected by using an alternate flight trajectory of the aircraft with more data sampling in the regions with error.

(a) U wind component (ft/s)   (b) U component error (ft/s)
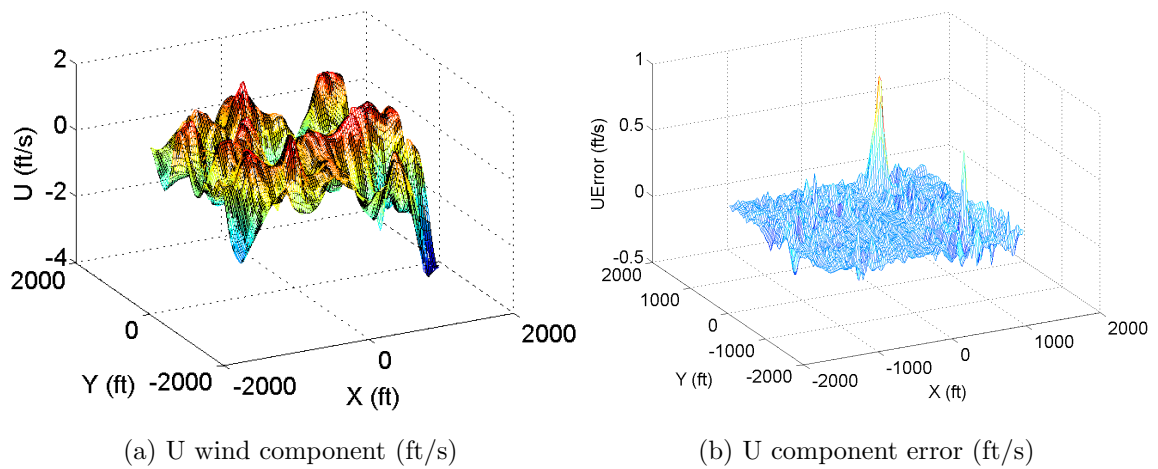
Figure 9. Simulation of two aircraft U wind component

The U wind component error (ft/s) in the x and y directions are shown in Figure 10.

(a) Error versus X (ft) (b) Error (ft/s) versus Y (ft)
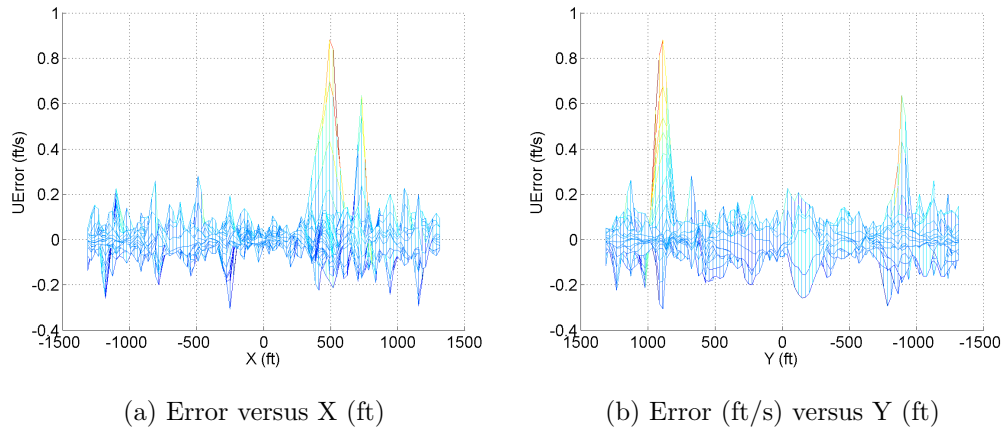
Figure 10. U wind component error

The y component of wind speed, V (ft/s) obtained from the aircraft is shown compared to the actual wind field and error in Figure 11. Most regions have errors well below 0.2 m/s, with a few small regions of error spiking above 0.5 m/s. One region in the X direction between 600 to 800 ft, and in the Y direction between 0 to -500 ft experiences a spike in error of -1.5 m/s. This is likely due to the trajectory of the aircraft resulting in minimal sampling in this region.

(a) V wind component (ft/s) (b) V component error (ft/s)
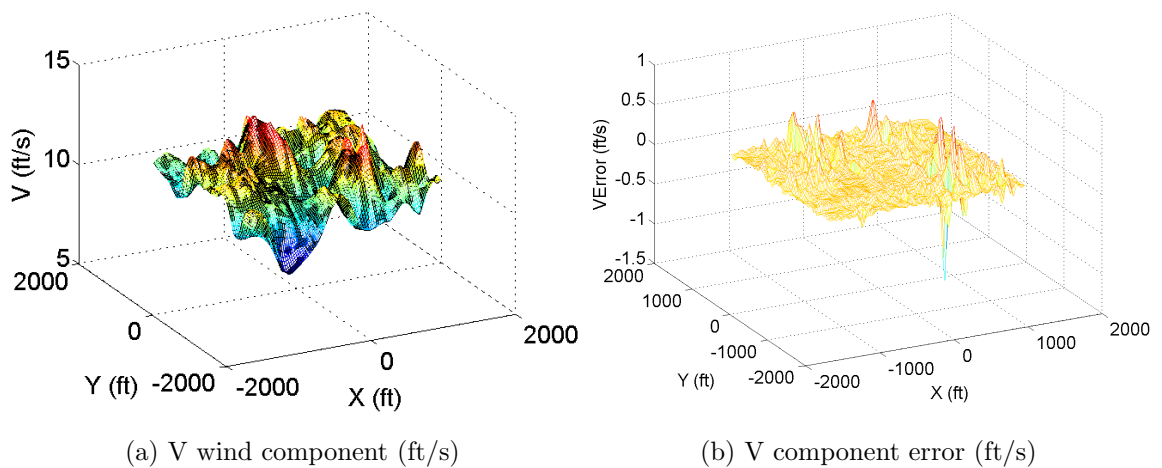
Figure 11. Simulation of two aircraft V wind component

The z component of wind speed, W (ft/s) obtained from the aircraft is shown compared to the actual wind field and error in Figure 12. A region in the X direction from 300 to 850 ft experiences the most error with a maximum error of -3.5 ft/s.

(a) W wind component (ft/s) (b) W component error (ft/s)
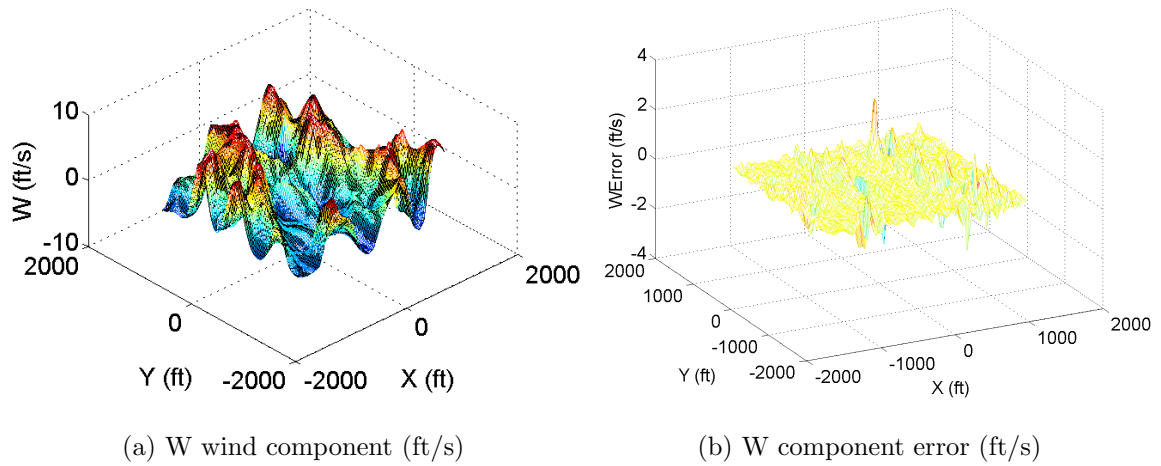
Figure 12. Simulation of two aircraft W wind component

The time taken to fly in the 3,000 ft^2 area was 8266 seconds, which is more than 2 hours. Realistically, the two aircraft would not fly this long or sample a space this large. The aircraft are also moving slowly in the simulation. Additional aircraft can be simulated with different trajectories and speeds to optimize sampling of the 3D wind field to reduce error and sampling time. Still, the concept is clear that this is a viable means to obtain wind speed using multiple MASS.

34

CHAPTER III
SENSOR OVERVIEW AND DESIGN

In this work, a mobile atmospheric sensing system (MASS) is presented that utilizes meteorological sensors and wind speed sensors to measure atmospheric parameters. An overview of the quadrotor and fixed-wing mobile platforms are presented, as well as various sensors for measuring pressure, temperature, relative humidity (PTRH), wind speed and wind direction. The design of a custom-built wind measurement sensor is detailed which includes the kinematic wind speed model for wind speed estimation. Preliminary ground testing and wind tunnel testing is used to validate and calibrate sensor wind speed measurements.

3.1 Mobile Platforms

Two different types of mobile platforms are used in this research. The first is an Iris+ 3D Robotics quadrotor and the second is an Apprentice S15e fixed-wing aircraft, which are both shown in Figure 13.

(a) Iris+ 3D Robotics quadrotor with transmitter   (b) Apprentice S15e fixed-wing aircraft

Figure 13. Mobile platforms used for the MASS (not to scale)

The Iris+ is powered by a rechargeable 3S lithium polymer (LiPo) 500 mAh battery and is equipped with four brushless DC motors. The payload capacity is 0.4 kg and it has a flight time range of 16 - 22 minutes. The Iris+ is equipped with a Pixhawk autopilot and contains a 3-axis gyroscope, accelerometer and magnetometer, as well as a barometer for measuring atmospheric pressure. Combined with a ground station, the Iris+ is capable of waypoint GPS navigation with a 3DR uBlox GPS with compass onboard the quadrotor. It can also be remotely piloted using a wireless transmitter. The Apprentice has a wingspan of 1.5 m, utilizes a 3S 3200 mAh LiPo battery and has a payload capacity of about 0.7 kg. Each aircraft contains a GPS and an inertial measurement unit (IMU) which provides linear acceleration and rotational rates. Key parameters of the Iris+ quadrotor and Apprentice S15e fixed-wing aircraft are listed in Table 6.

Table 6. Aircraft key parameters summary

Parameter	Iris+ Quadrotor	Apprentice S15e Fixed-Wing
Motors	950 kV	840 kV
Mass	1.282 kg	1.390 kg
Height	0.1 m	0.2 m
Spanwise Length	0.6 m	1.5 m
Payload Capacity	0.4 kg	0.7 kg
Flight Time	16 - 22 min	8 - 12 min

These aircraft were chosen based on their medium-rated payload capacity and flight time range compared to cost.

3.2 Atmospheric Sensors

Each MASS is equipped with two commercially available sensors for measuring atmospheric pressure, temperature and relative humidity. The first is the iMet-XQ meteorological sensor by InterMet Systems, shown in Figure 14a and the second is the Adafruit BME280 I2C Temperature Humidity Pressure (Adafruit PTH) sensor, shown in Figure 14b. The iMet-XQ sensor has a mass of 15 g and was designed specifically for rotary wing UAVs. The self-contained sensor is 100 by 30 mm and includes a GPS receiver. It has a battery life of 120 minutes and sampling rate of 1-3 Hz. The iMet-XQ utilizes a piezoresistive pressure sensor with a range of 10 to 1200 hPa, accuracy of $\pm$ 1.5 hPa and resolution of 0.02 hPa. The bead thermistor temperature sensor has a range of -95 to 50° C with an accuracy of $\pm$ 0.3° C and resolution of 0.01° C. The capacitive humidity sensor has a range of 0 - 100 % relative humidity (RH) with an accuracy of $\pm5\%$ RH and resolution of 0.7% RH [35]. The Adafruit PTH Bosch breakout board is 19 x 18 mm and has a mass of 1 g. It is wired to an Arduino Uno for data logging, which has a mass of 25 g. The Adafruit PTH has an operating range from -45 to 50° C with $\pm$ 3 ° C accuracy. Humidity is measured with with $\pm3\%$ accuracy, and barometric pressure is measured with ±1 hPa absolute accuracy [36].

(a) iMet-XQ meteorological sensor   (b) Adafruit PTH sensor
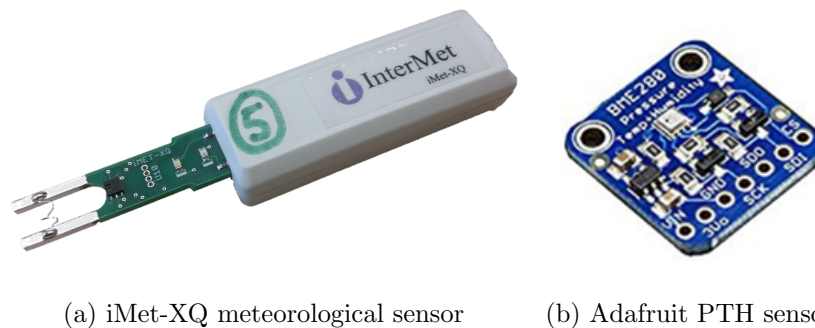
Figure 14. Sensors for measuring pressure, temperature and relative humidity.

3.3 Wind Measurement Sensors

There are several different methods and sensors that exist to directly measure wind speed in situ versus indirectly measuring winds using an empirical model of vehicle flight dynamics. Some sensors measure scalar wind speed such as pitot-static tubes and cup, vane or hot-wire anemometers, while other sensors measure magnitude and directional wind speed, such as multi-hole probes, and 2-axis or 3-axis ultrasonic (US) anemometers. The problem, however, arises in the ability to measure wind parameters using sensors on board a quadrotor. These sensors equipped on a moving platform are subject to altitude changes, rotational motion and vibration, resulting in sensor noise and data processing needed to accurately estimate wind speed and direction. As such, there are trade-offs between weight, cost, accuracy, capabilities and size for these sensors. A range of commercially available wind measurement sensors were evaluated for their application onboard quadrotors. A summary of selected sensors are listed in Table 7.

Table 7. Selected windspeed measurement sensor comparison

Sensor	Manufacturer	Mass	Cost	Capability	Range/Accuracy
Single pitot probe	Hobby King	100g	\$30	Scalar	$\pm\,2.5 m/s$
Multi-hole probe	Aeroprobe	300 g	\$1.5k	Vector	$\pm 1 m/s$
Omniprobe	Aeroprobe	400 g	\$5k	Vector	$\pm 0.01 m/s$
Cup anem.	Adafruit	220 g	\$50	Scalar	$0.5-50\pm0.5 m/s$
Hot-wire anem.	Sper Scientific	471 g	\$482	Scalar	$0.2-25\pm0.1 m/s$
2D US anem.	Gill	500 g	\$1.5k	Vector	$0-60\pm2\% m/s$
2D US anem.	R. M. Young	400 g	\$1.5k	Vector	$0-75\pm0.1 m/s$
3D US anem.	R.M. Young	1700 g	\$3k	Vector	$0-40\pm0.05 m/s$

Pitot probes that utilize differential pressure measurements range between $30 − 5,000 with accuracies down to 0.01 m/s. Based on the evaluated sensors, payload capacity of the Iris+ quadrotor and budget limitations, the most suitable sensors for study are the single-hole pitot probe and Adafruit anemometer, even though they only measure scalar wind speed. However, given no weight or cost constraint, the 12-hole Omniprobe and 3D ultrasonic (US) anemometer provide the most accuracy for scalar and directional wind speed with accuracies of 0.01 m/s and 0.05 m/s, respectively. Description and results of detailed testing of the Adafruit cup anemometer and single pitot probe follow in the next sections.

3.3.1 Anemometers

The Adafruit standard cup anemometer is shown in Figure 15 wired to an Arduino Uno microcontroller for logging data. The anemometer wired to the Arduino with a LiPo battery and PTH sensor has a mass of approximately 220 g. It is capable of sampling data at rate of 5 Hz and taking scalar wind speed measurements with an accuracy of $0.5 m/s$ at a range between 0.5 and $50 m/s$. This anemometer provides an analog voltage output which ranges from 0.4 to 2.0 V, which corresponds to a range of 0 to 50 m/s, with a resolution of 0.1 m/s. It has a height of 0.105 m and arm length of 0.07 m.
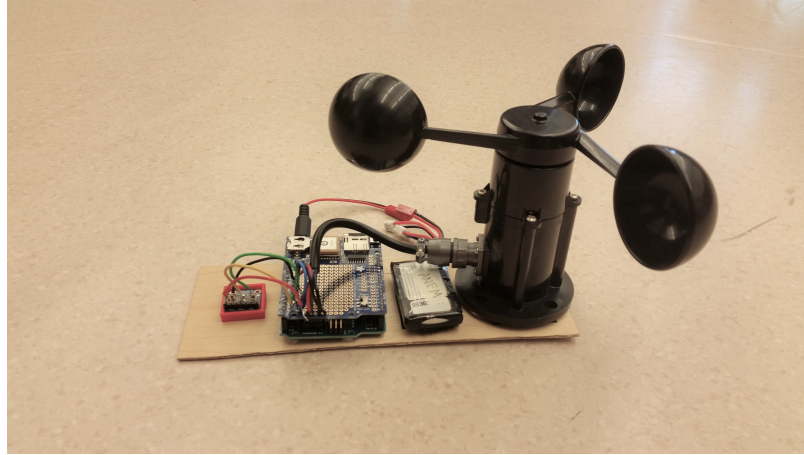
Figure 15.   Adafruit standard cup anemometer

To calculate scalar wind speed, U, from the voltage output of the anemometer, V_{out}, the minimum and maximum voltage and wind speed ranges of the anemometer are used, as shown in Equation 36. A calibration constant, K_w, is determined using wind tunnel testing.

$$V_{min} = 0.4 \text{ V}$$

$$V_{max} = 2.0 \text{ V}$$

$$U_{min} = 0 \text{ m/s}$$

$$U_{max} = 50 \text{ m/s}$$

$$U = \frac{(V_{out} - V_{min})(U_{max} - U_{min})}{(V_{max} - V_{min})} K_w \tag{36}$$

3.3.2 Pitot Probe Sensor Design

Pitot-static tubes are used for estimating wind speed with a pressure differential measurement. Static ports provide static pressure while a port pointed directly into the flow provides stagnation pressure. A schematic diagram for a wired pitot probe is shown in Figure 16. UV resistant clear PVC tubing (not shown) connects the pitot tube to a pressure board mounted onto an Arduino Uno microcontroller. The

pressure board provides an analog signal in raw bits to the Arduino Uno based on the dynamic pressure and equivalent diaphragm deflection. The Arduino Uno is powered by a 7.4 V 430mAh LiPo battery and logs GPS and the raw bits to the micro SD card which is later converted to wind speed data.
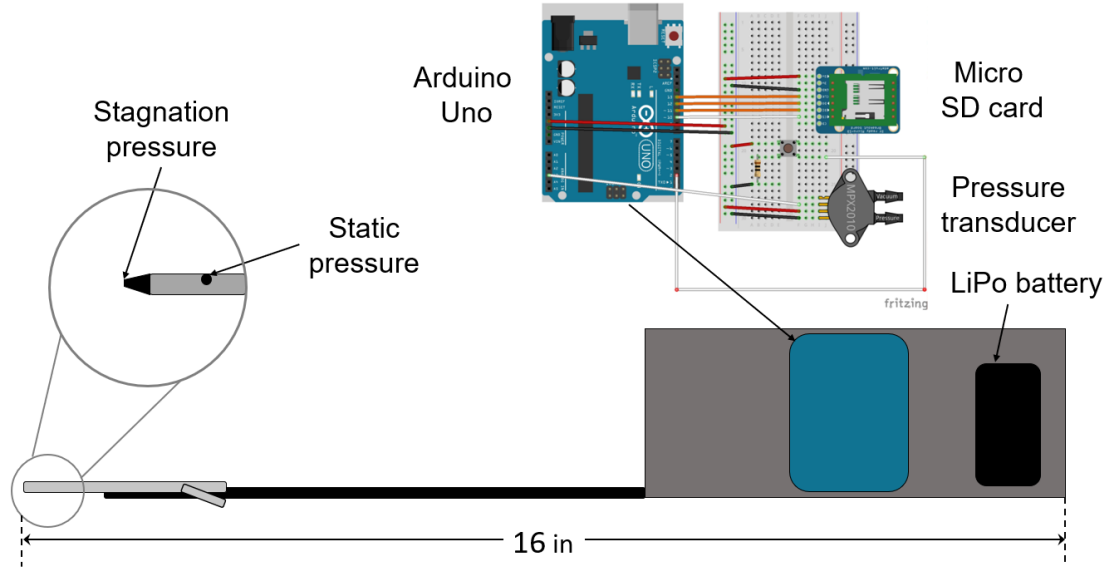
Figure 16. Pitot-static tube sensor diagram

The scalar measurement of wind speed by the pitot-static tube, $\tilde{v}_p$, is determined using a modified form of Bernoulli's equation for calculating indicated airspeed. Calibrated airspeed, shown in Equation 37, is corrected for instrument and position error and utilizes impact pressure, q_c, the standard speed of sound, a_0, and ambient pressure, p_0 [37].

$$\tilde{v}_{p_i} = a_0 \sqrt{5 \left[\left(\frac{q_c}{p_0} + 1 \right)^{2/7} - 1 \right]} \tag{37}$$

Equation 37 is valid for airspeeds at subsonic level. The speed of sound is assumed to change with altitude due to changing temperature of the surrounding air, so the

www.manaraa.com

ideal gas law is used to compute the speed of sound based on the adiabatic index of air and the molar gas constant. A correction factor can be included to provide accurate wind speed measurements based on calibration of the pitot-static tube. A prototype of the single pitot sensor design was fabricated for testing and is shown in Figure 17. The pitot-static tube is extended on a carbon fiber rod to avoid propeller wash from the quadrotor. A small area is left on the balsa wood platform for atmospheric sensors for measuring pressure, temperature and relative humidity.
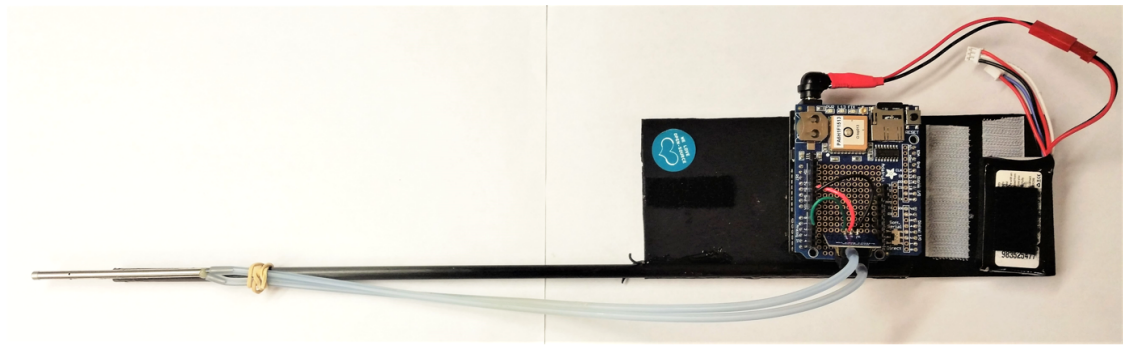
Figure 17. Prototype pitot-static tube sensor (top down view)

A clear limitation of the single pitot sensor design is the ability to only measure wind speed in the flow direction in which the pitot tube is pointing. To alleviate this, multiple pitot tubes can be used to measure wind speed from different directions. The multi-hole probe and omniprobe utilize this concept, but at a much higher cost than multiple pitot tubes. To obtain the full wind speed vector, four pitot tubes can be placed orthogonally on the quadrotor, providing wind speed components along the lateral and longitudinal quadrotor fixed-axes. The problem then arises in the optimal placement and configuration of the four tubes on the quadrotor. The four spinning rotors generate downwash which would affect sensor measurements if the pitot-static tube inlets are placed in turbulent regions of air

42

near the rotors. To minimize the effects of the propeller downwash, the four pitot tubes can be placed near the aircraft body on the interior of the rotor radius, as shown in Figure 18, or extended on booms outside of the rotor radius where downwash is not produced. With a propeller diameter of 0.24 m, the pitot tubes would need to be extended a distance of 0.38 - 0.425 m from the Iris+ quadrotor center of mass (COM). Alternatively, the pitot tubes could be placed on the interior of the propellers, about 0.13 m away from the COM.
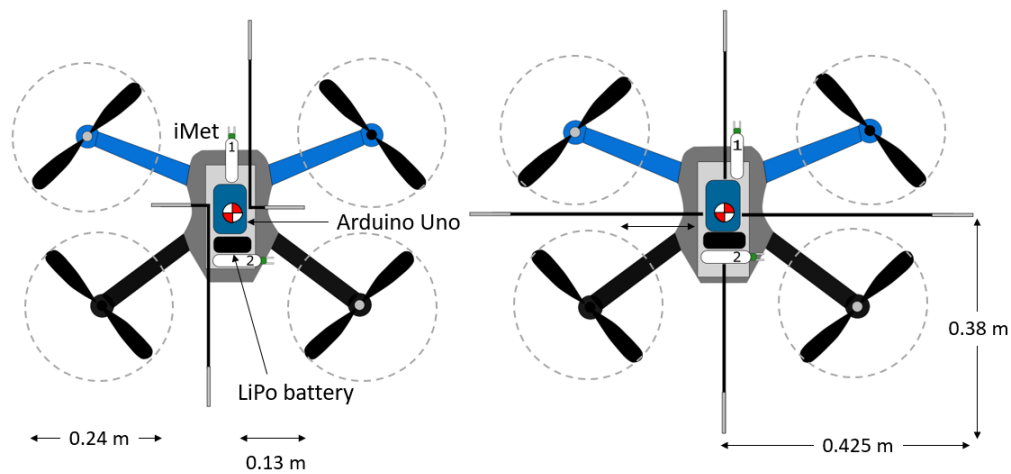
Figure 18. Two sensor configurations on the Iris+ quadrotor (top down view)

Knowledge of the rotor downwash profile of the quadrotor would allow for the sensor design to be optimized. Mapping the flow around the rotors can be accomplished using Computational Fluid Dynamics (CFD) or physical testing. With limited access to CFD modelling and the simplicity of physical testing, a test bench was set up to verify the predicted areas of minimal quadrotor downwash. The quadrotor is fixed to a platform so that the spinning rotors do not cause the aircraft to lift, as shown in the experimental test setup in Figure 19. Scalar propwash is observed in a plane 1 inch above the quadrotor using a Windtronics cup anemometer.

43
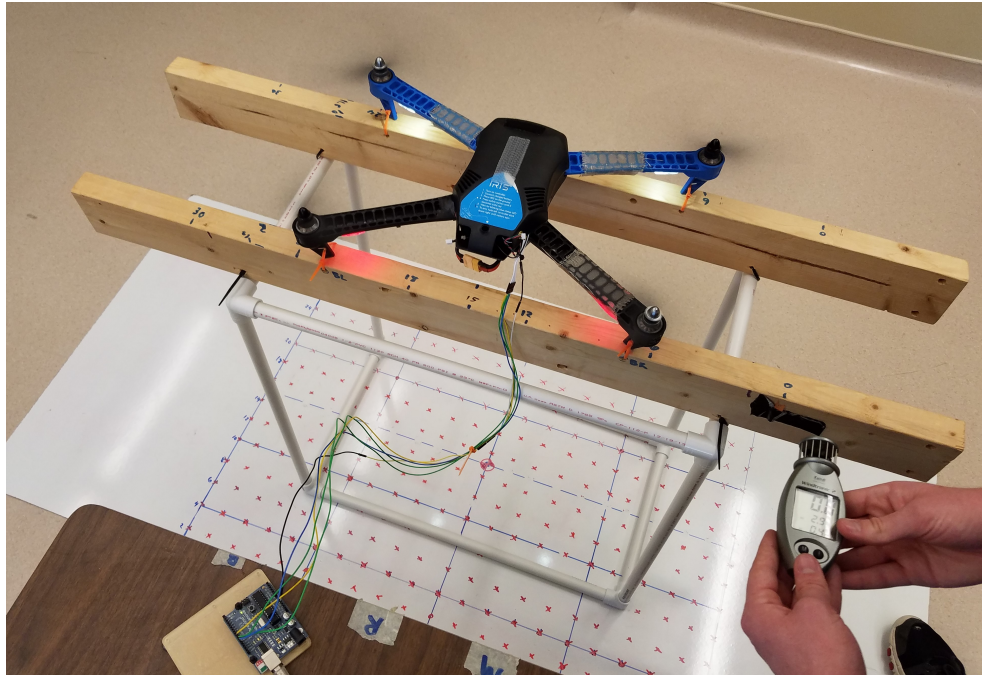
Figure 19.   Experimental setup for quadrotor propwash profile

A 40 x 30 inch grid was created to map data observation points of wind speed above the quadrotor. The quadrotor overlayed on the grid is shown in Figure 20.
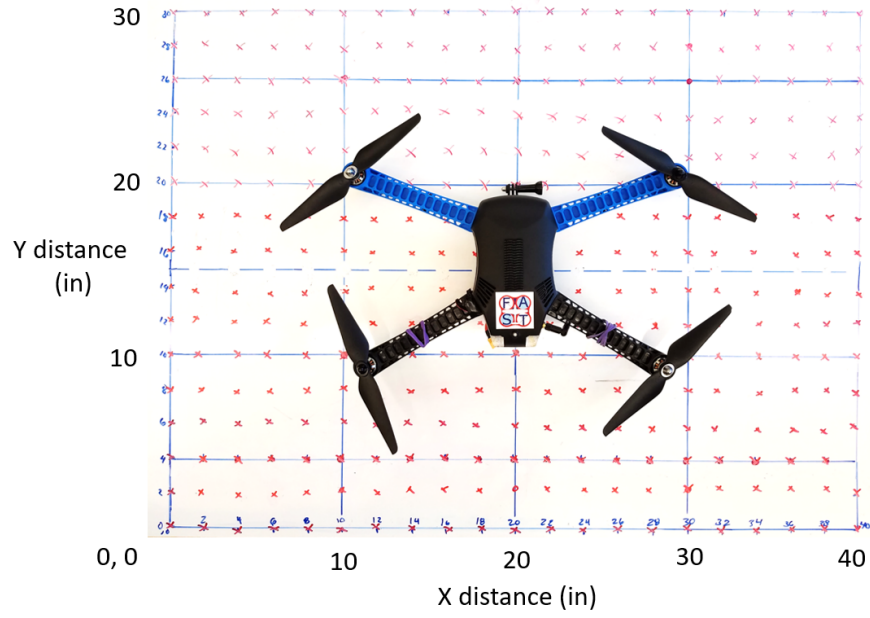
Figure 20. Scalar windspeed (m/s) as a function of spatial location

With the quadrotor fixed to the test bench, wind measurements were manually recorded from the Windtronics anemometer for the grid of 300 data observation points. Wind speed as a function of spatial location in a plane 1 inch above the quadrotor is shown in Figure 21 with contour propwash profiles.

(a) Quadrotor 2D propwash profile   (b) Quadrotor 3D propwash profile
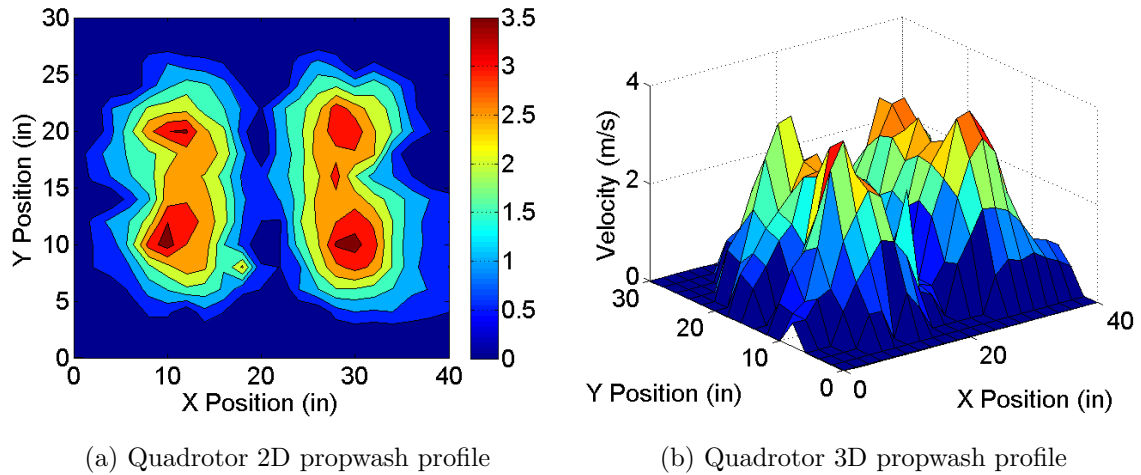
Figure 21. Scalar wind speed (m/s) as a function of spatial location

As expected, the highest measured wind speeds from the propwash are located above the spinning rotors and decrease parabolically moving away from the rotors.The maximum windspeed around the rotors range from 3.2 to 3.7 m/s. The slight skew of the data is attributed to experimental error. Clearly, the location of the wind speed sensors could significantly influence measurements, and thus, should be positioned out of the influence of the propwash. The wind speed sensor was fabricated as shown in Figure 22 with two booms extending horizontally away from the aircraft body. It has a mass of 0.226 kg. This design is an improvement of the initial designs shown in Figure 18 by minimizing the number of booms extending from the quadrotor body. As shown in Figure 22, the pitot-static tubes for the east and west wind speed components can be placed on booms extended on the front and rear of the aircraft body such that the north and west components and south and east components are coupled together. The sensor is about 32 inches in length total.

46
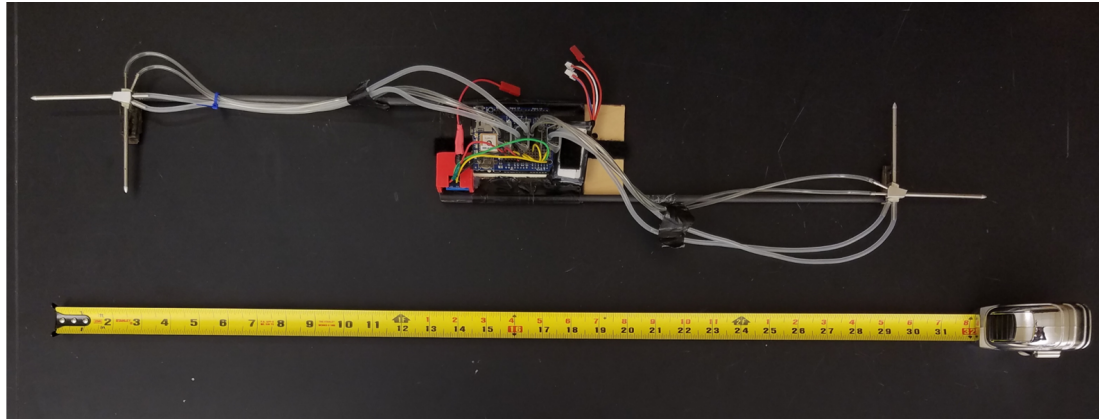
Figure 22.   Horizontal wind measurement sensor

However, since the propwash profile was only determined for a plane 1 inch above
the quadrotor, additional testing was performed to determine the minimum height
the sensor should be placed above the aircraft body to avoid propeller downwash.
This vertical test, shown in Figure 23, indicates that the sensor should be at a
minimum height of 0.1 m (4 in) above the aircraft body to avoid the effects of
downwash on FMS wind speed measurements. Thus, a second sensor was designed
that extends vertically above the quadrotor body to avoid downwash, rather than
extending horizontally outside of the rotor radius.
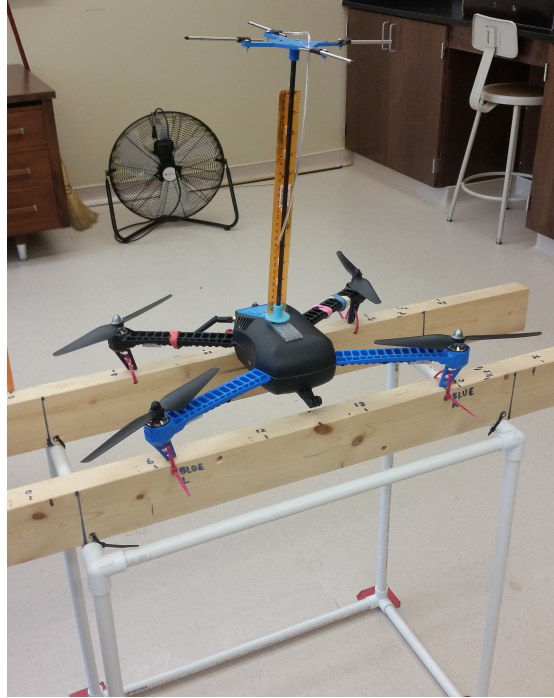
Figure 23. Vertical downwash test

The fabricated vertical sensor is shown in Figure 24 with a single vertical boom extending 0.1 m (4 in) above the aircraft body. This sensor has a mass of 0.202 kg, which is 0.024 kg less than the first sensor. A custom-designed piece was 3D printed to mount the four pitot-static tubes on the vertical boom outside of the propeller downwash. Accuracy in sensor wind speed measurements is limited based on the prototype construction of the sensor. The four pitot probes are not aligned perfectly, nor is the base of the sensor perfectly vertical. The pitot probes are mounted with screws which sometimes loosen and allow the pitot probe to rotate. The combination of these issues, with cheap pressure transducers for the pitot probes, results in hardware limitations for accuracy in wind speed and direction measurements.
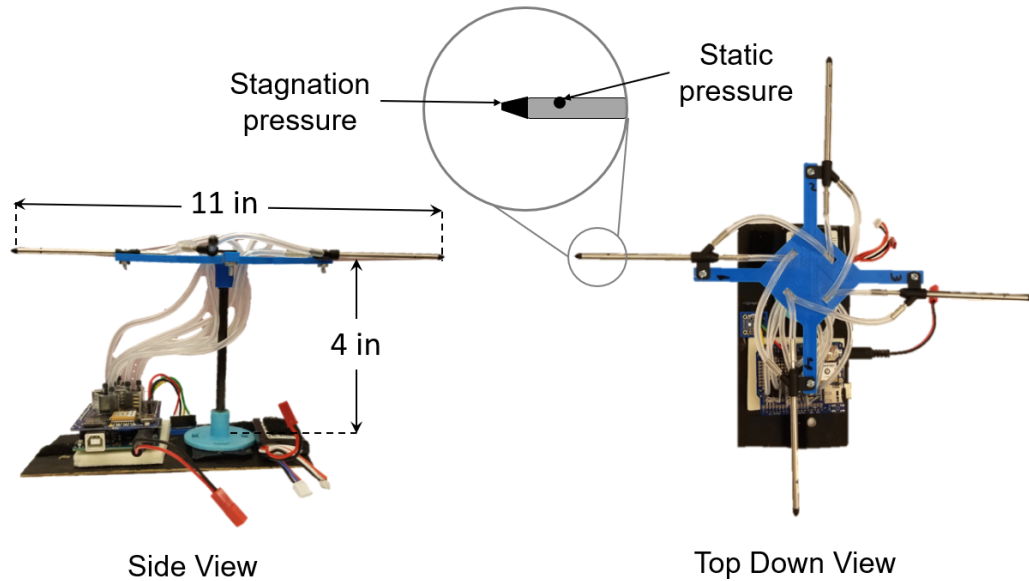
Figure 24. Vertical wind measurement sensor

3.4 Preliminary Calibration and Testing

This section includes preliminary ground testing of the PTH and wind speed measurement sensors. Fan tests, vibration tests, and wind tunnel tests are performed and calibration and filtering of the data is detailed.

3.4.1 Flow Measurement Sensor Ground Testing

Once fabricated, the two flow measurement sensors were tested to validate wind speed measurements for all four directional components. First, the horizontal FMS was tested on board the Iris+ quadrotor, as shown in Figure 25a.
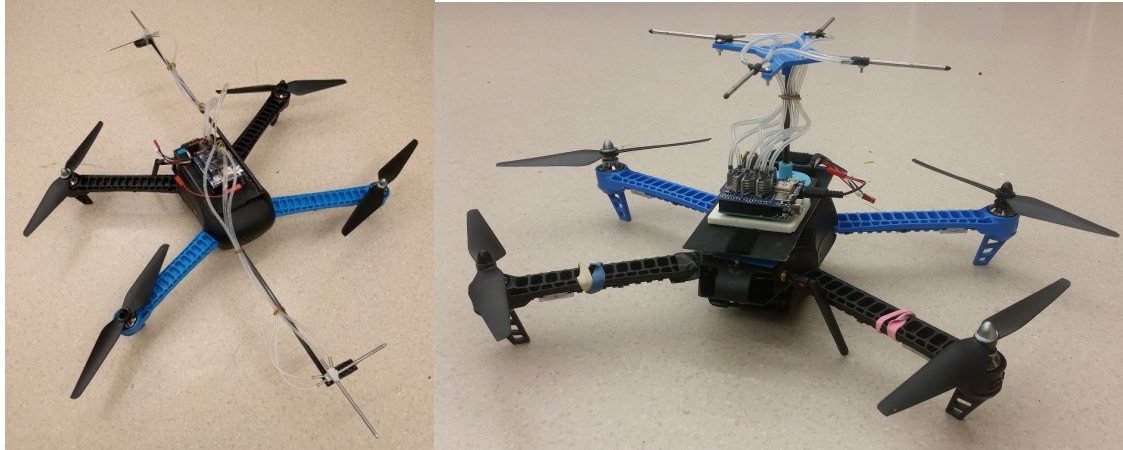
(a) Horizontal sensor (FP4)   (b) Vertical sensor (FP4V)

Figure 25. Quadrotor flow measurement sensors

The quadrotor was remotely piloted indoors and flown to hover next to a standard Utilitech fan at 1 m in height to expose the FMS to a known external wind source. During hover, the quadrotor was then rotated 90° counter-clockwise so that each of the four pitot-static tubes would be exposed to the flow for about 20 seconds each. Results from testing are shown in Figure 26. The flow profile from the fan is not linear, so the magnitude of each wind speed component reading varies between 3 m/s and 6 m/s since the quadrotor did not maintain a constant altitude during each rotation. Overall, the results indicate that each wind speed component is reading properly with a potential bias approximately 0.5 m/s for the south and east wind speed components.
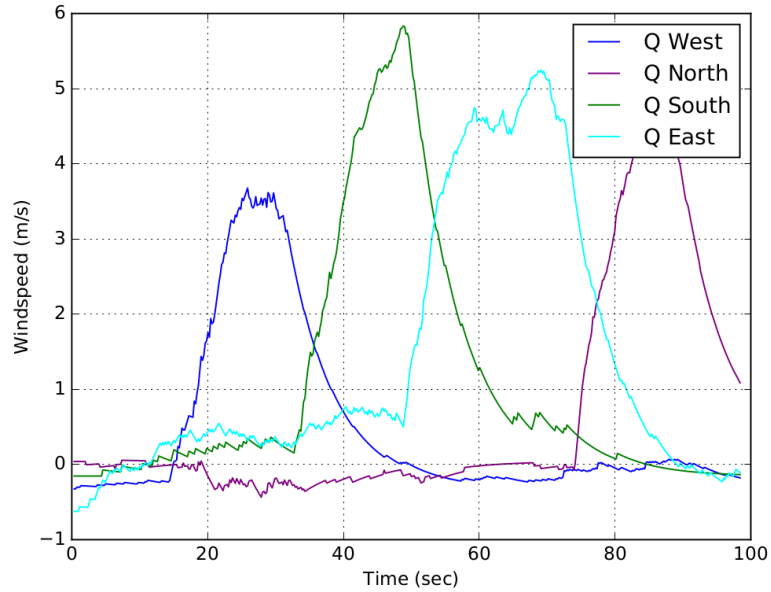
Figure 26. Sensor testing on quadrotor

Utilizing the Utilitech fan, a mounted platform was used to test each of the two
FMSs independent from the quadrotor to isolate any vibration noise and altitude
changes from the hovering quadrotor. The horizontal FMS was rotated clockwise in
front of the center of the fan starting with the east wind speed component for 30
seconds each. The same test was repeated for the vertical FMS except the sensor
was rotated counter-clockwise starting with the east wind speed component. A wind
gauge was used to determine a wind speed on the mounted platform of 6.0 m/s.
Wind speed results from testing shown in Figure 27 are smoother than wind speed
results in Figure 26 and indicate that the horizontal FMS provides more accurate
measurements between components than the vertical sensor. Coincidentally, the
south wind speed component for both sensors provides a wind speed measurement
1.5 m/s lower than two of the other components. Furthermore, the horizontal FMS
captured an average wind speed of approximately 6 m/s while the vertical FMS
captured an average wind speed of approximately 3 m/s. It seems the vertical FMS
is biased by 3 m/s and should be corrected using individual correction factors for

51

each wind speed component. It is important to note, however, that the Utilitech fan is also an industrial sized fan that produces non-uniform flow, which could be a source of error for the biased results. Future work would involve testing the sensors inside a wind tunnel to obtain more uniform wind speed data.

(a) Horizontal FMS   (b) Vertical FMS
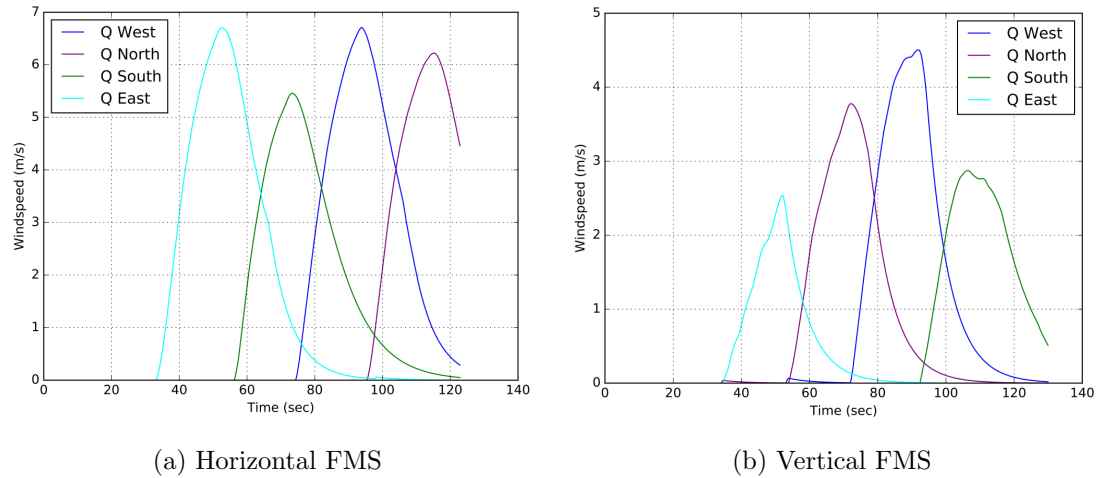
Figure 27. Flow measurement sensor fan testing

3.4.2 Vibration Testing and Analysis

During initial testing of the flow measurement sensors, vibration from the quadrotor became a concern for wind speed measurements. To determine the amount of vibration noise affecting the sensors, the Iris+ quadrotor equipped with the wind speed sensors was tested indoors with caps placed on the pitot-static tubes to eliminate any external wind speed measurements. This vibration test is the first experimental test case with four total experimental test cases for quantifying the impacts of the mobile platform on wind estimations. For Case 1, the sensors are tested while stationary, with the velocity of the quadrotor, V_Q, and the atmospheric

52

winds, V_A, both equal to zero. This trivial case should result in wind estimations from the sensors, U_A, equal to zero, without sensor noise.

<div align="center">Case 1: Quadrotor stationary with no atmospheric winds</div>

$$\vec{V_Q} = 0$$

$$\vec{V_A} = 0$$

$$U_A = 0$$

For testing, the flow measurement sensor was installed on the quadrotor and set to record five minutes of data with the quadrotor on ground-level. The quadrotor was then flown at a height of 0.6 m with the flow measurement sensor and remotely piloted to hover for five minutes. Then the quadrotor returned to its takeoff position and the flow measurement sensor recorded data for another five minutes. The quadrotor equipped with the flow measurement sensor for vibration testing is shown in Figure 28.

<div align="center">Figure 28. Quadrotor FMS vibration testing</div>

Figure 29a shows the raw data from the flow measurement sensor with a value of 515 bits for the East/West components and 520 bits for the North/South

components before and after hovering. The central region shows the influence of vibration on the quadrotor, increasing the raw bit data by an average of 3 bits. To reduce the amount of vibration noise affecting the raw data measurements, servo tape was applied between the mobile platform and flow measurement sensor interface. As seen in Figure 29b, this dampened some of the vibration; however, this noise still affects the wind speed measurements as the quadrotor is in hover since vibration travels through the interface between the platform and the sensor.
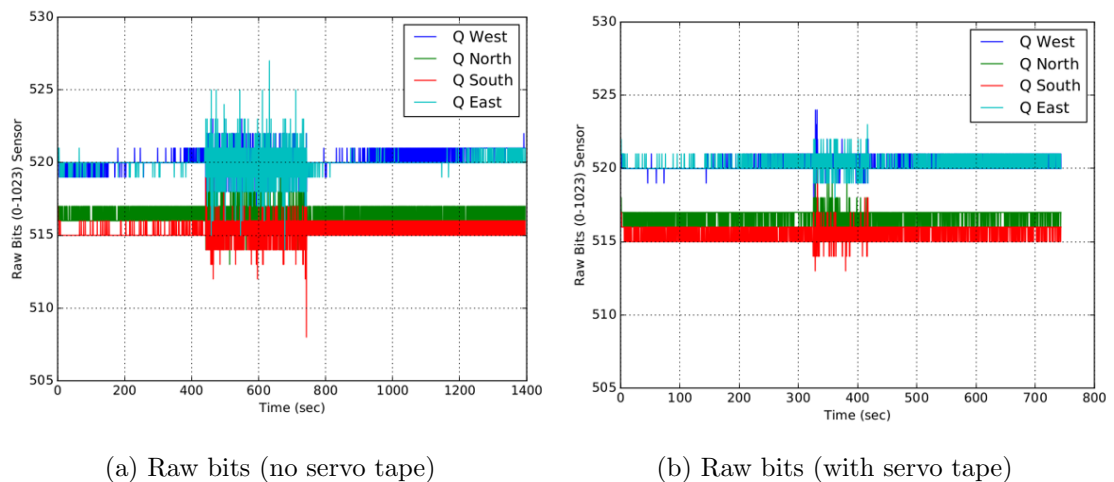
(a) Raw bits (no servo tape)   (b) Raw bits (with servo tape)

Figure 29. Horizontal flow measurement sensor vibration testing

The two flow measurement sensors were tested again using servo tape on both sensors. The significant spike in the raw bits reading approximately 140 s in Figure 30a for the horizontal FMS was a result of a poor remotely piloted landing and should be ignored. Results from Figure 30b indicate that the horizontal FMS experiences less vibration from the hovering quadrotor than the vertical FMS, suggesting that the horizontal FMS is capable of more accurate wind speed measurements.

54

(a) Raw bits for horizontal FMS testing   (b) Raw bits for vertical FMS testing
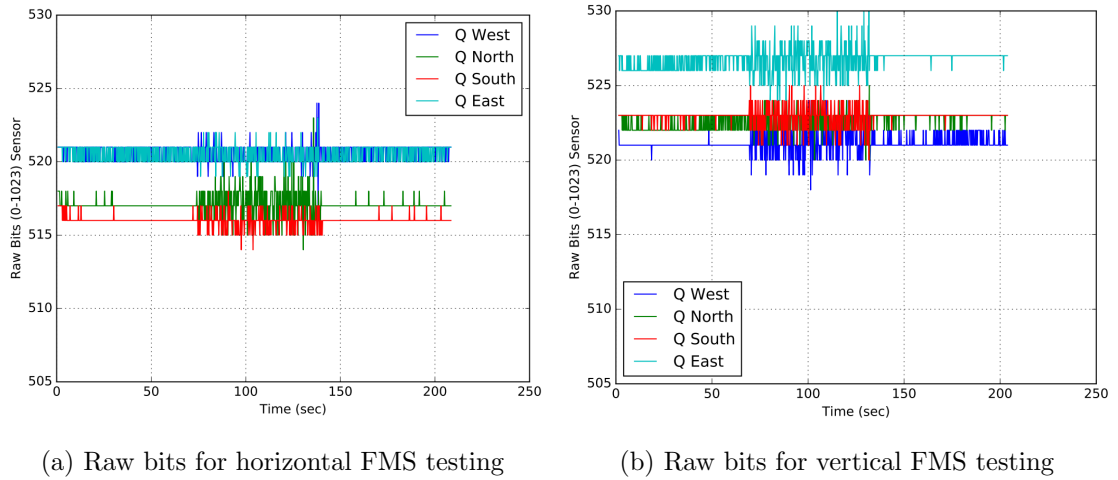
Figure 30. Vibration analysis for both flow measurement sensors

Vibration testing was repeated for the vertical sensor once the vertical boom was anchored down to the platform with bolts, depicted in Figure 31a. Data was taken for 60 seconds with the quadrotor off, then the quadrotor was turned on for 60 seconds, and then turned off for 30 seconds. Results indicate that with the new vertical sensor design and the bolted rod, the sensor experiences almost negligible vibration transmissivity from the quadrotor.
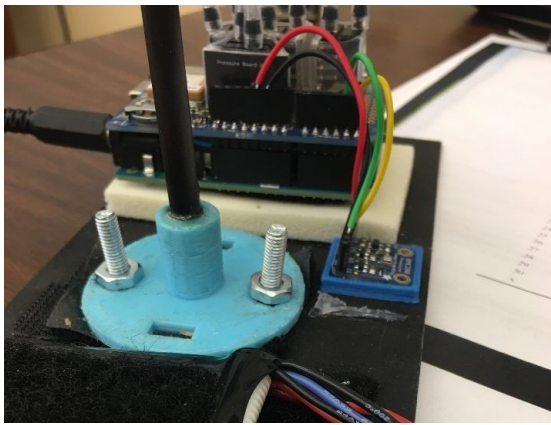
(a) Vertical sensor with bolts
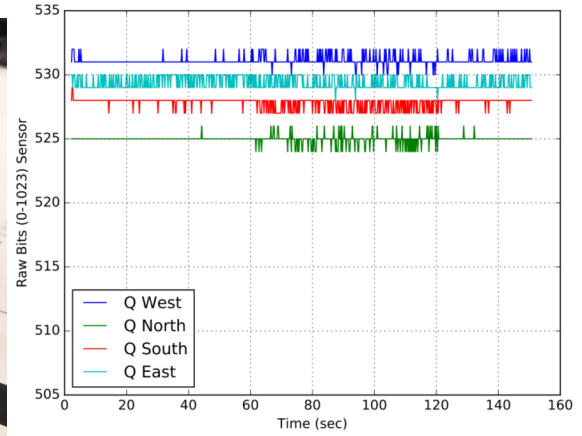
(b) Raw bits for vertical FMS testing

Figure 31. Vibration testing for vertical sensor

Filtering is introduced to alleviate noise in raw sensor measurements. A truncation filter is used to to determine mean bits from the first 20 seconds of data. Data that is within 2 bits of the mean raw bit value is set to the mean value. A standard complementary low-pass filter is used as shown in Equation 38 with filtered speed, U_f equal to the previous filtered measurement combined with the unfiltered previous wind speed measurement.

$$U_{f(i+1)} = (1 - \sigma)U_{f(i)} + \sigma U_{(i)} \tag{38}$$

where $\sigma = 0.03$ and $U_{f0} = U_0$.

An example of raw data versus filtered data is shown in Figure 32 with raw data in blue and filtered data in red. The truncation filter determines the mean bits, and the data is filtered significantly, reducing the data noise to an output of zero, as shown between 1000 and 1800 seconds in the figure.

56
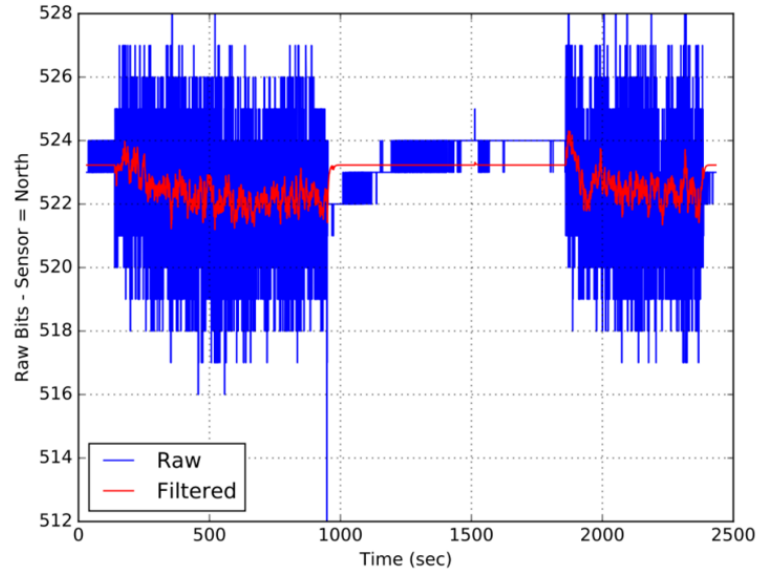
Figure 32. Vibration filtering

3.5 Wind Tunnel Testing

A Hampden Model H-6910-12 low speed wind tunnel, shown in Figure 33, was used to validate and calibrate wind speed measurements for all sensors. It contains an aerodynamic flow straightener section with low head-loss and provides uniform flow. With a 12 inch square test section, it is capable of reaching air speeds of up to 100 mph, but is typically operated below 50 mph. The prototype pitot sensor, the FP4V and two Adafruit anemometers were tested in the wind tunnel against a WindTronics wind gauge.

3.5.1 Anemometer Wind Tunnel Testing

The anemometer placement in the wind tunnel is shown in Figure 33. For anemometer testing, the wind tunnel fan frequency was manually increased every 60

57

seconds from 0 to 40 Hz in 5 Hz intervals. This procedure was performed for two standard cup anemometers, Anem 0 and Anem 1.
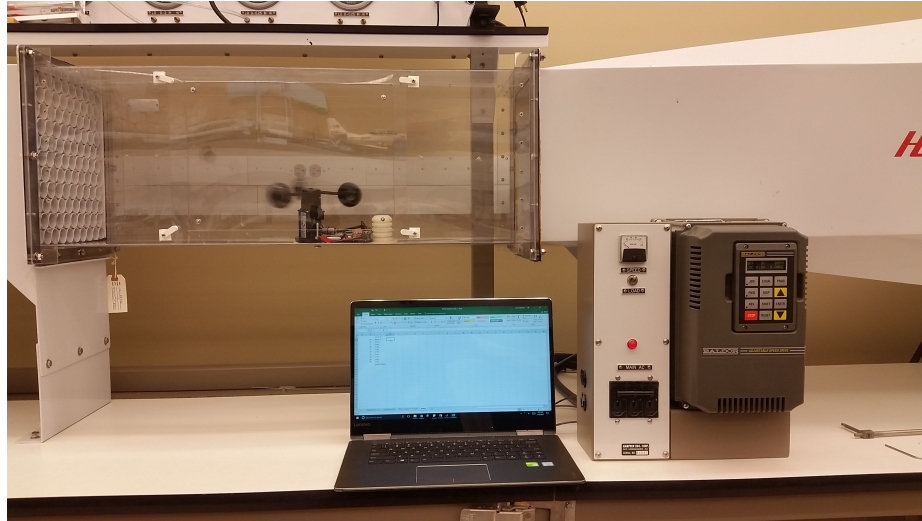
Figure 33. Anemometer wind tunnel test

Voltage outputs (mV) of the anemometers as a function of time (sec) are shown in Figure 34 for the two tests. Results indicate that the voltage outputs are in general agreement.
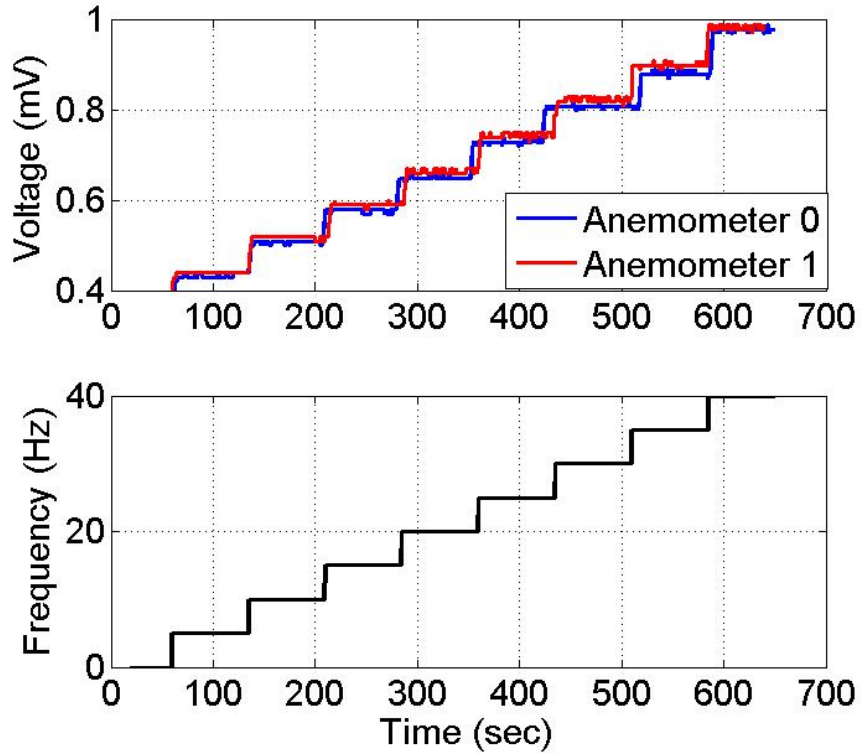
Figure 34.   Anemometer wind tunnel test

Scalar wind speed is calculated from the output voltage of the anemometer using
Equation 36. To calibrate the anemometer wind speed output, a WindTronics wind
gauge, shown in Figure 35, was tested in the wind tunnel using the 0 to 40 Hz test
procedure.
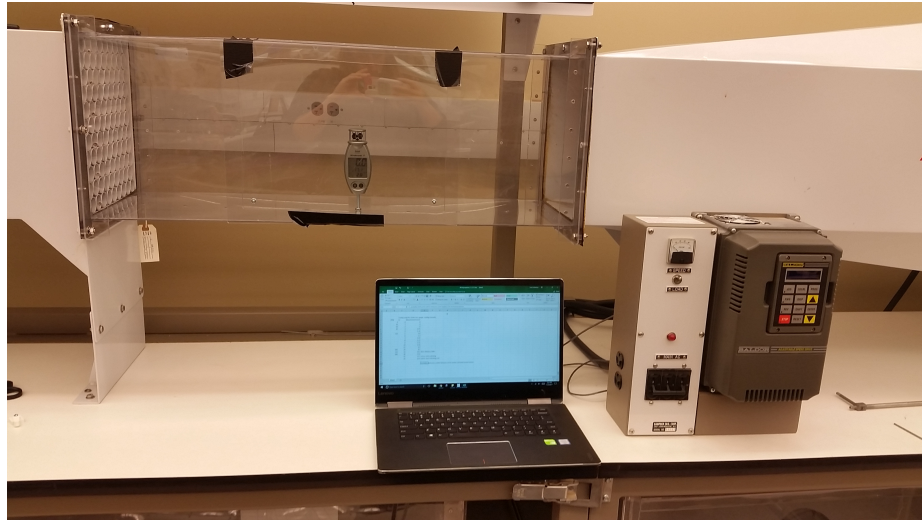
Figure 35.   WindTronics anemometer wind tunnel test

Calculated wind speed, calibrated wind speed and averaged wind speed as function
of time for Anemometer 0 and Anemometer 1 are shown in Figure 36, with
$K_w = 1.545$.
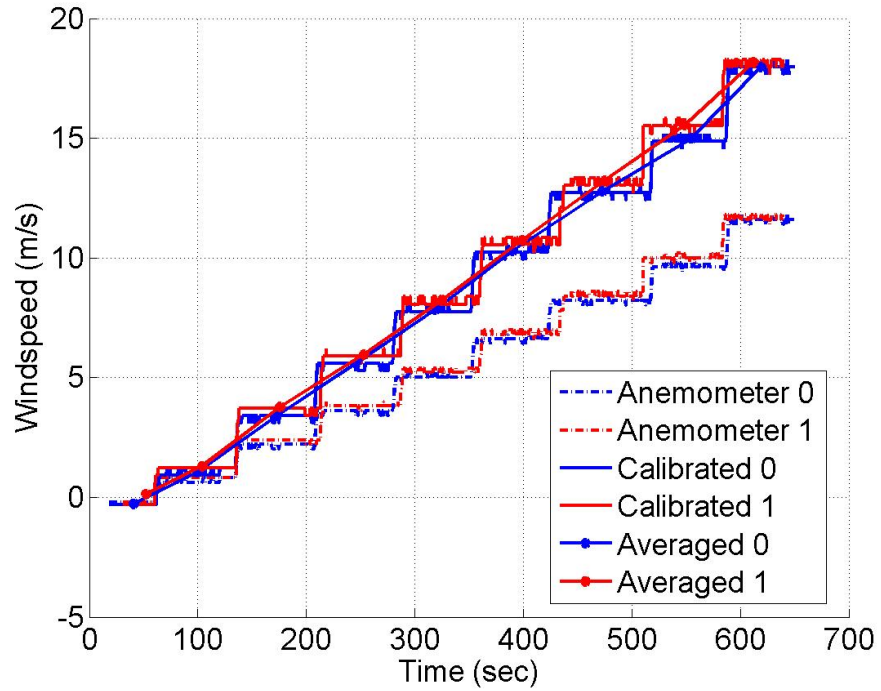
Figure 36.   Windspeed versus Time

The wind speed for each anemometer averaged over 60 second intervals is shown in Figure 37a against the wind gauge windspeed. The percent difference between the two anemometers versus the Windtronics anemometer is shown in Figure 37b.

(a) Windspeed vs. Frequency

(b) Sensor percent difference vs. Frequency
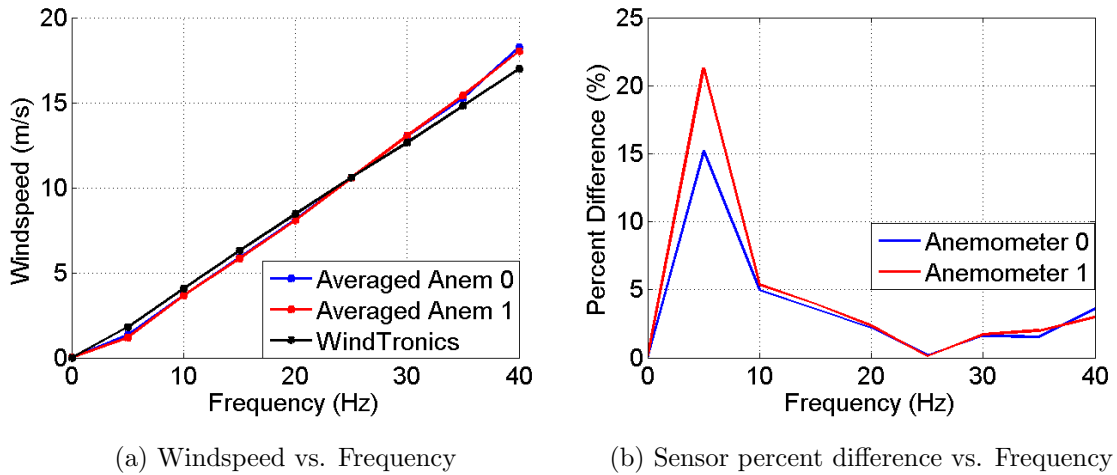
Figure 37. Anemometers and wind gauge wind tunnel tests

The root-mean-square error (RMSE) between Anem 0 and Anem 1 is 0.10 m/s, while the RMSEs between the two anemometers and the Windtronics anemometer are both 0.53 m/s. The absolute error between Anem 0 and Anem 1 are shown in Figure 38. The maximum error between the two sensors occurs at 40 Hz with an absolute error of 0.179 m/s. It is interesting to note that most error is introduced at the lowest and highest wind tunnel frequencies, and the absolute error between 10 and 30 Hz is almost negligible, with errors less than 0.04 m/s between the two anemometers. This could be either from experimental error or the accuracy in measurement range for the sensor itself.
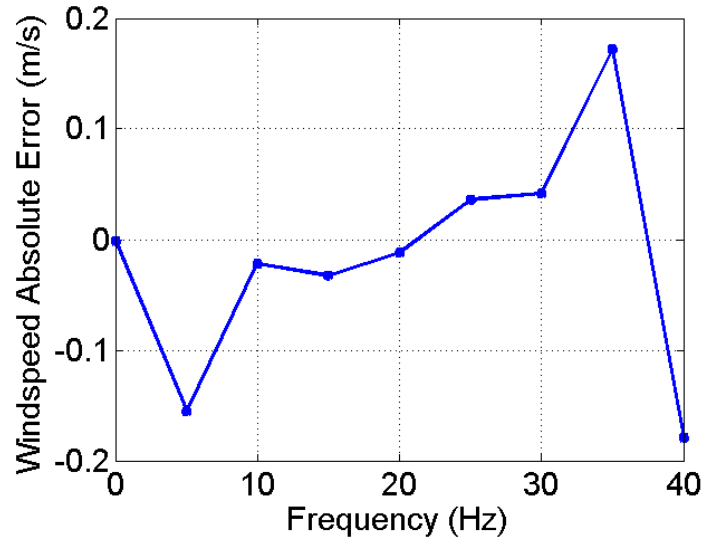
Figure 38. Anemometer absolute error as a function of wind tunnel frequency

3.5.2 Pitot Wind Tunnel Testing

The pitot sensor placement in the wind tunnel is shown in Figure 39. Each of the four pitot static-tube wind speed components were tested individually in the wind tunnel by rotating each component into the wind flow.

63
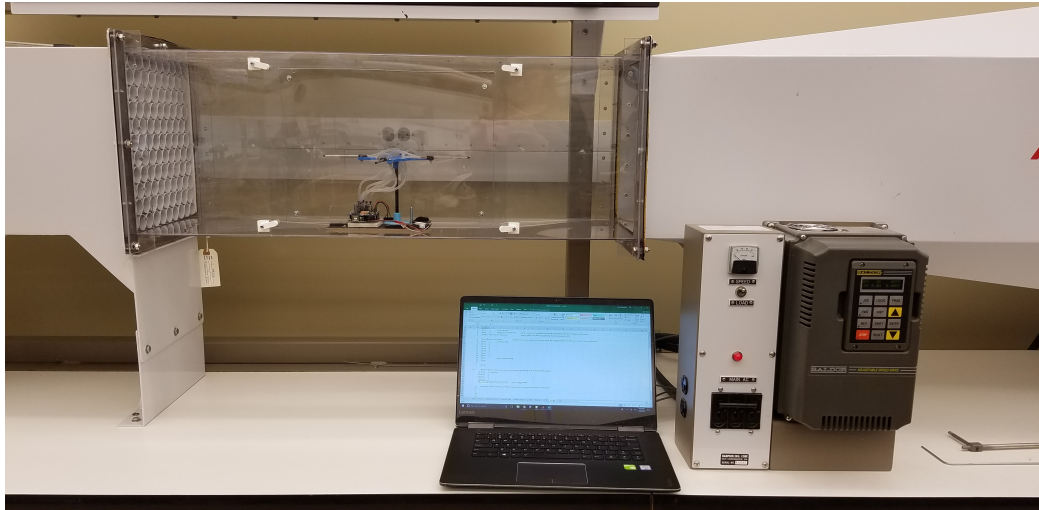
Figure 39. Pitot sensor wind tunnel test

Each of the four components were tested individually at 5 Hz frequency intervals of the wind tunnel fan. The four pitot component results are shown in Figure 40, with raw data as a function of time and average wind speed as a function of frequency.
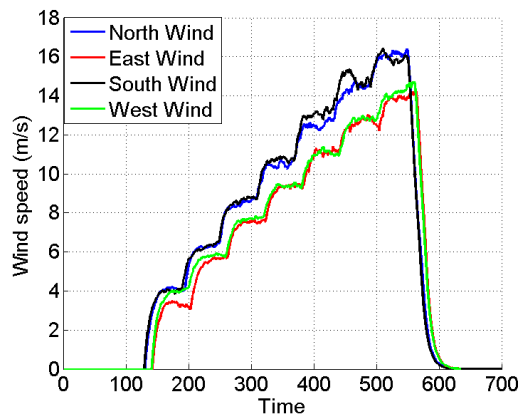
(a) Raw pitot data
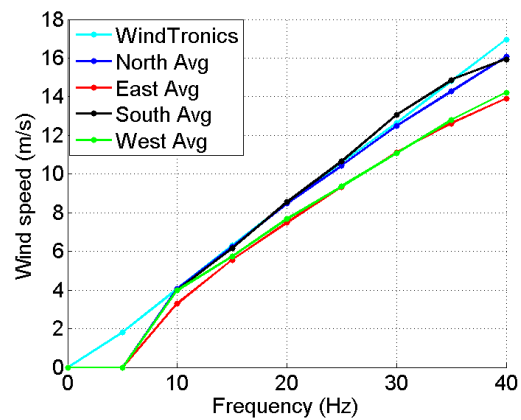
(b) Wind speed data as function of frequency

Figure 40. Four pitots wind tunnel testing

64

Pitots were corrected using scale a factor: $s = [1.02, 1.15, 1.01, 1.1]$ for the North, East, South and West sensors. Using this correction factor, the RMSE's of the four sensors are 0.64, 0.70, 0.70 and 0.81, respectively.

(a) Raw pitot data   (b) Wind speed data as function of frequency
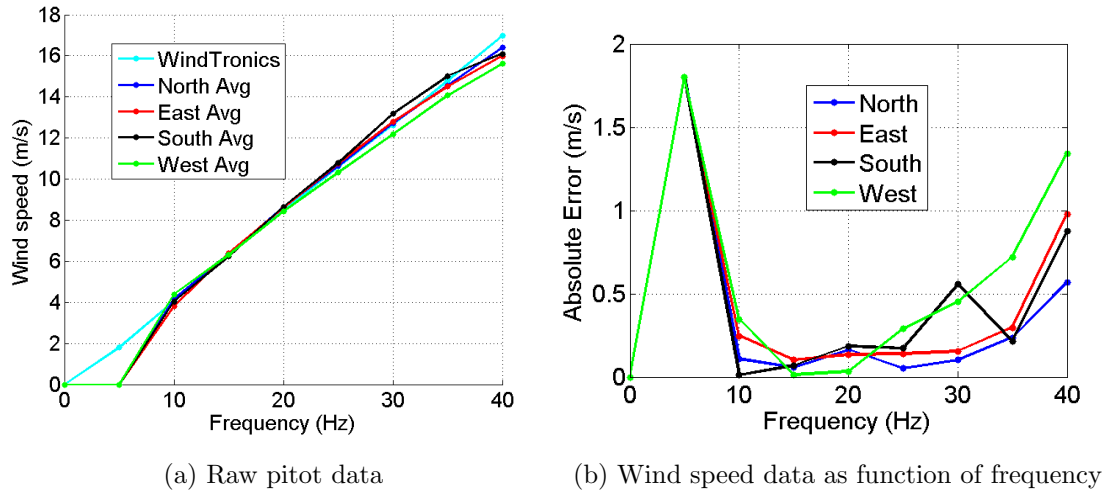
Figure 41. Corrected four pitots and asbolute error

The north wind speed component was tested in higher frequency intervals in the wind tunnel and compared to the WindTronics anemometer. The wind speed of the north pitot component as a function of frequency in 1 Hz intervals is shown in Figure 42, along with the percent difference between the pitot and the WindTronics Anemometer in Figure 43b. With a correction factor of $K_n = 1.09$, the north wind speed component is calibrated to the WindTronics Anemometer. These results indicate that the pitot does not accurately measure wind speeds below 5 m/s, however, this is an example of over-filtered data. The truncation value of 2 bits cuts off small wind speed measurements. These are difficult to quantify, since the noise of the sensor is high.
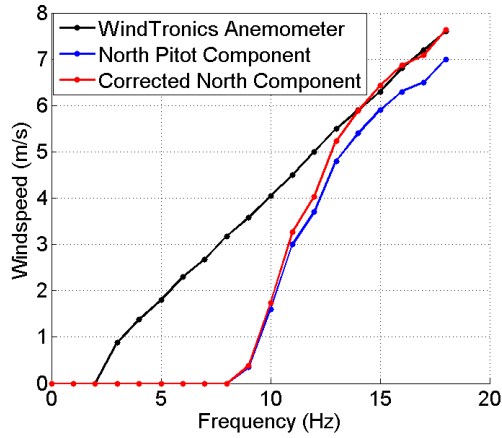
(a) North pitot component against the WindTronics
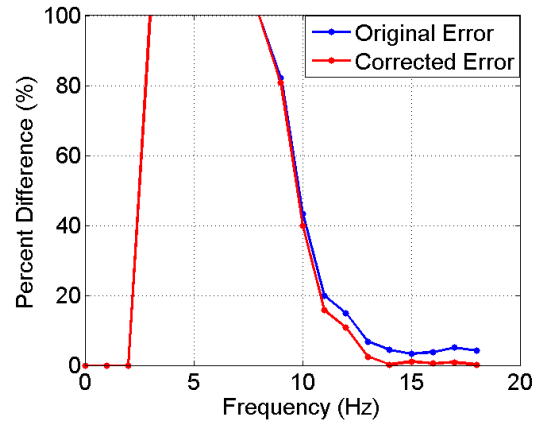
(b) Percent differences

Figure 42. North pitot component wind tunnel test

When the truncation bits are reduced to 1.5 and the complementary filter constant
is set to 0.022, the wind speed measurements match more closely to the
WindTronics. Figure 43 indicates that the pitot probes can accurately measure
wind speeds below 5 m/s, with a threshold of 2 m/s.
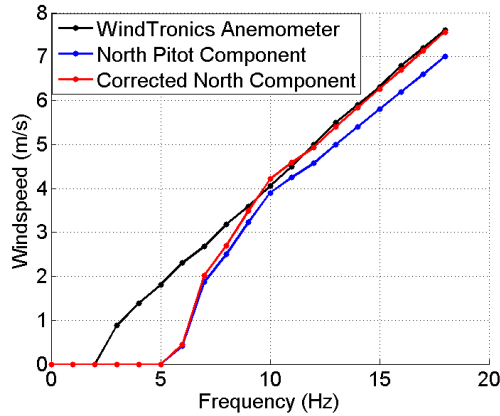
(a) North pitot component against the WindTronics
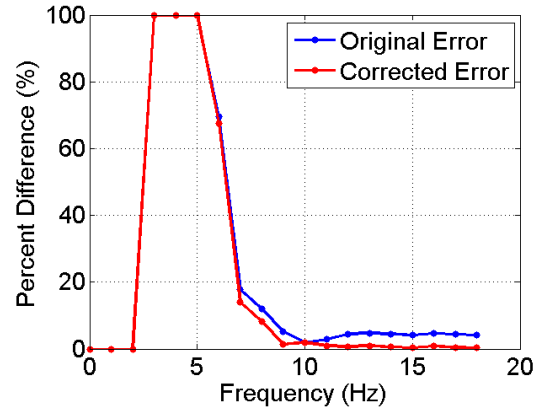
(b) Percent differences

Figure 43. Second north pitot component wind tunnel test

There are clear limitations of the pitot sensors to accurately estimate wind speed. The pitot does not start estimating wind speed until the wind tunnel reaches 9 Hz, which is equivalent to approximately 3 m/s. Furthermore, when each pitot sensor component is tested individually, the actual wind speed measurement in a realistic wind field is not taken into consideration. This is because the direction of flow is not isolated in a wind field, and multiple pitot-static tubes must be used to determine both the wind speed and direction in a realistic wind field. When the pitot probes are arranged orthogonally to each other, the roles of the stagnation port and static ports must be evaluated. A zoomed photo of the pitot probe mounted on the wind measurement sensor is shown in Figure 44. The single pitot probe shown is mounted to a 3D printed platform with a standard screw, and contains one stagnation port and four static ports placed orthogonally.
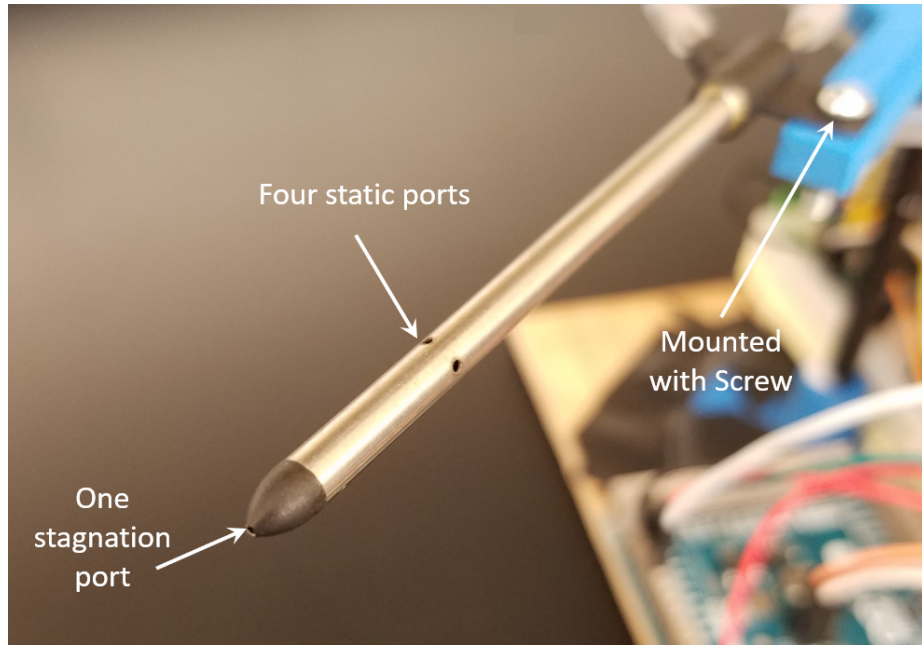
Figure 44. Detailed view of pitot probe mounted to wind measurement sensor

Based on flow direction, the stagnation port and four static ports will each have a corresponding positive or negative reading. An example of the port roles are shown in Figure 45, with the wind field originating from two different directions.

$P_0 > P_\infty$ and $\Delta P > 0$ $P_0 > P_\infty$ and $\Delta P < 0$
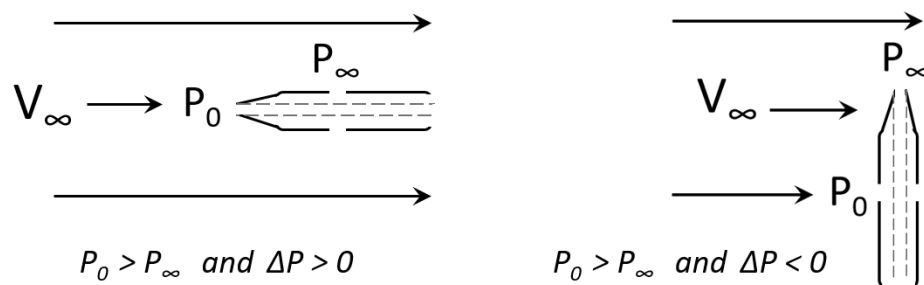
ΔP = Dynamic Pressure = Stagnation − Static Pressure

Figure 45. Stagnation and static pressure ports from wind direction

To mitigate this, a pitot model can be incorporated which relates the components from all four pitots to the flow direction. When the sensor is placed in the wind tunnel, the component facing into the wind will show the maximum magnitude of wind, while the other three components will show the negative readings. As shown in Figure 46, the East component is facing into the wind with increasing fan frequency intervals from 0 to 20 Hz. As the East wind speed increases, the South and North components decrease proportionally, while the West component decreases slightly.
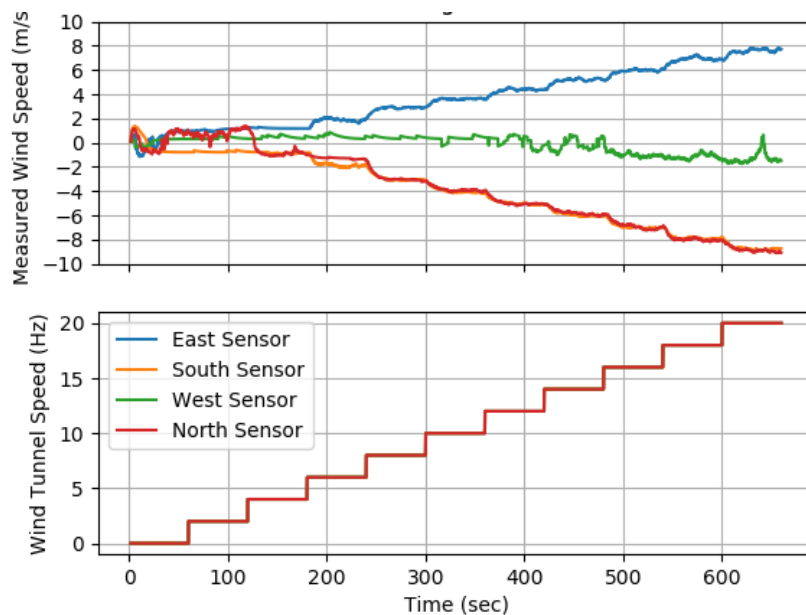
Figure 46. East component facing into the wind

Note, however, that the pitot sensors have an accuracy in the wind tunnel of approximately $\pm 2m/s$, which makes fitting the output to an empirical model potentially erroneous. Nonetheless, the magnitude factor of a single component as it is rotated in the tunnel can be fit to an expected output. The heading of the sensor $\psi = 0°$ corresponds to the North facing component. Magnitude factor as a function

of rotation angle (heading) for the North pitot is shown in Figure 47. This theoretical magnitude factor is based on the geometry of the sensor.
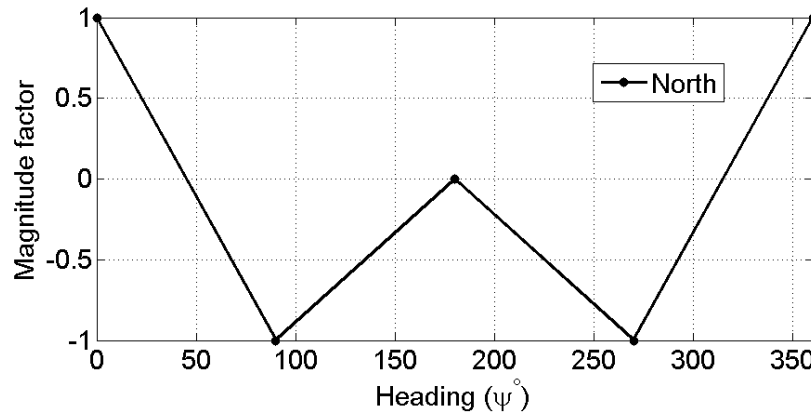
Figure 47. Theoretical magnitude factor as a function of heading based on geometry

In the work done by Simmons, the FP4V was tested in the wind tunnel at various rotation angles at wind tunnel frequencies of 20 and 35 Hz [38]. The wind speeds extracted by Simmons do not match the expected magnitude factor of the four sensors when rotated. Based on the 12 inch size of the wind tunnel test section and the size of the sensor, potential boundary layer issues may cause the wind speed data to be erroneous. This test can be repeated using a larger wind tunnel that is sized appropriately for the sensor size. Note that the discrete data extracted from wind tunnel testing was smoothed and does not reflect expected data representation.
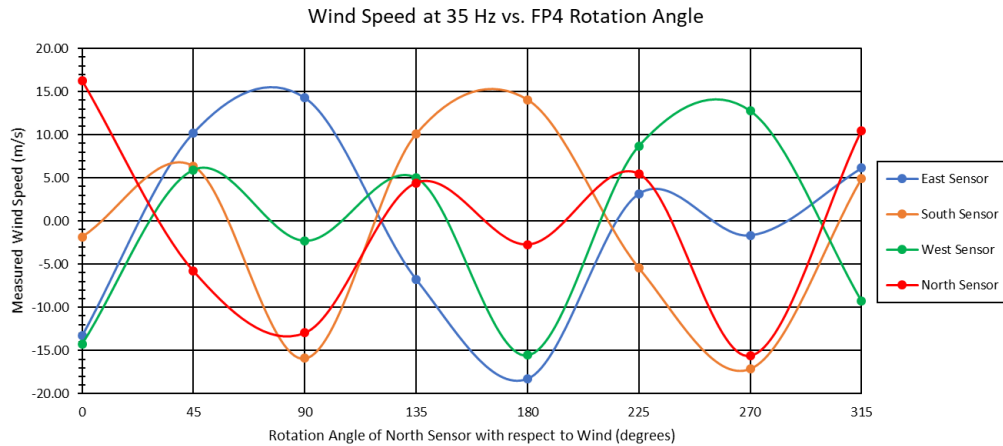
Figure 48. Wind speed (m/s) versus direction (°) at 35 Hz

The raw data from the 20 Hz and 35 Hz wind tunnel tests were scaled to the magnitude factor of ± 1 for proper comparison, as shown in Figure 49. The two data streams were averaged, as shown by the light blue line. To account for experimental error, symmetry was used on the average to obtain the green line. For example, at a 45° heading angle, the magnitude factor should yield the same results as a 315° heading angle. As previously discussed, the potential boundary layer issues in the wind tunnel can cause significant discrepancies in data, as seen in the differences between the 45° and 315° heading angles. Another possibility for these differences is the manual rotation of the sensor during testing. This could be improved with verification of the actual angle of the sensor using an angle sensor or stepper motor to accurately rotate the sensor during data acquisition.

71
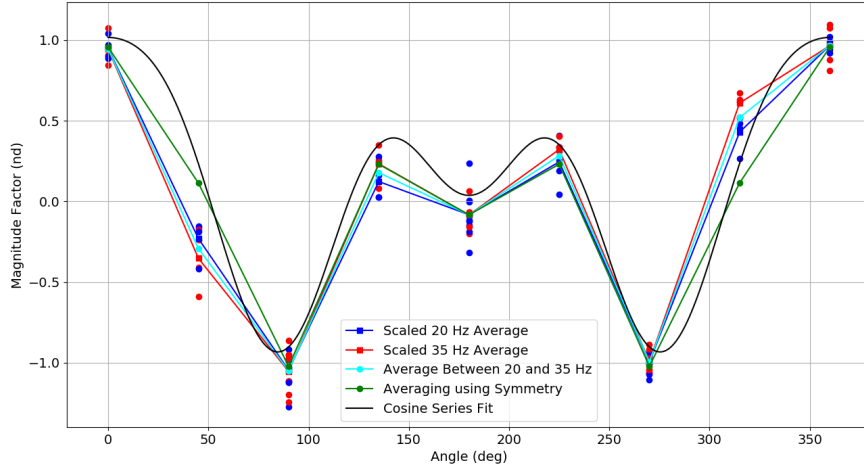
Figure 49. Magnitude factor and direction (°)

Using Figure 49, it is clear that an empirical model can be used to compute the four pitot component measurements given a wind speed, V_0 and direction ψ_0. For example, if the wind speed is 5 m/s and the heading $\psi = 0°$, the four pitot component readings should be [5, -5, 0, -5] with a NESW configuration. If the wind speed is 3 m/s and the heading $\psi = 45°$, the four pitot component readings will be [0.705, 0.705, 1.05, 1.05]. These measurements can be obtained using Equation 39.

$$\hat{V} = v_0 \Sigma (a_n cos((n+1)\psi_n)) \tag{39}$$

where the summation goes from n= 0,3 and $\psi_n = \psi_0 - \frac{n\pi}{2}$

The coefficient a_n is obtained using a half range cosine Fourier series fit, which is also shown in Figure 49 in black [39]. Using Equation 39, a two dimensional grid search can be used to obtain wind speed and direction using the four measured signals of the pitot components. This is accomplished by varying v_0 and ψ_0 from 0 to 10 m/s and -180 to 180°, respectively. The theoretical signals are then computed for each grid point and then compared to actual signals measured, with the best fit

72

selected. Wind speed and flow direction using the algorithm are shown in Figure 50 at 35 Hz. With an actual wind speed of 15 m/s at 35 Hz, the algorithm does not accurately estimate the actual wind tunnel speed, indicating that the empirical model is not a good fit, or the data is skewed because of the wind tunnel boundary layer. The algorithm wind speed oscillates around the actual wind speed, with a 3 m/s error near 45° and 315° rotation angles.
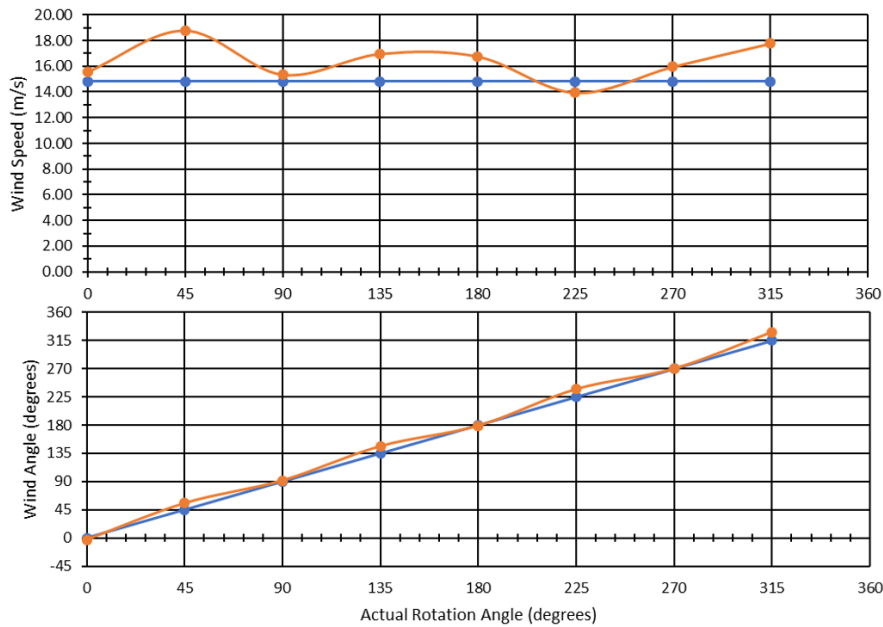
Figure 50. Wind speed (m/s) and direction (°) algorithm vs actual (35 Hz)

The wind speed and direction relative error (%) are shown in Figure 51 with almost a 30 % relative error at the 45° offsets. The maximum error occurs at 45° increments likely because the signals are so close together that any error in each measurement creates a large change in the output of the algorithm. This can be seen in Figure 48, which shows the measured wind speed of each component as a function of rotation angle. Although the maximum error is approximately 30%, most errors remains below 20%.

73
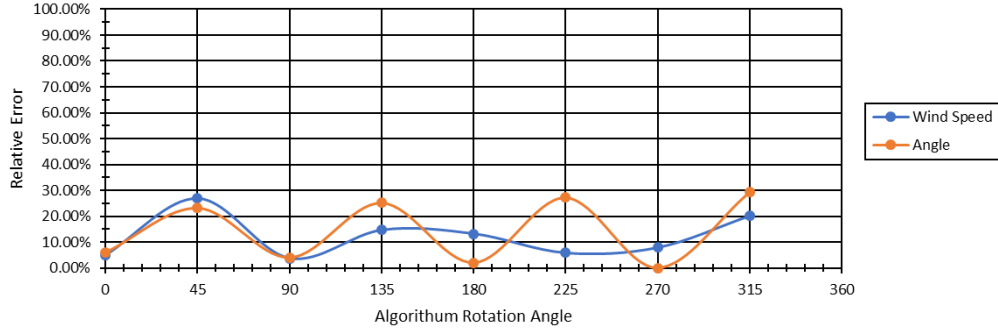
Figure 51. Algorithm wind speed (m/s) and direction (°) error at 35 Hz.

3.6 Wind Speed Kinematic Model

To account for the effects that the moving aircraft have on the wind speed measurements, the dynamics of the moving aircraft are modeled and incorporated into the wind speed calculation. For each MASS, the effects of ground speed must be subtracted from the wind speed measurement from the pitot-static tubes. Thus, the corrected velocity measurement for wind speed in the inertial reference frame $\vec{V}_{ATM/I}$ is represented as:

$$\vec{V}_{ATM/I} = T_{IB}(\hat{V}_P - \vec{w}_{B/I} \times \vec{r}_{B-P}) - \vec{v}_{B/I} \tag{40}$$

The transformation matrix, $\mathbf{T}_{IB}$, relates the aircraft body reference frame to the inertial reference frame, where trigonometric functions are shorthanded using standard notation: $cos(\alpha) \equiv c_\alpha$ and $sin(\alpha) \equiv s_\alpha$.

$$\mathbf{T}_{IB} = \begin{bmatrix} c_\theta c_\psi & s_\phi s_\theta s_\psi - c_\phi s_\psi & c_\phi s_\theta c_\psi + s_\phi s_\psi \\ c_\theta s_\psi & s_\phi s_\theta s_\psi + c_\theta c_\psi & c_\phi s_\theta s_\psi - s_\phi c_\psi \\ -s_\theta & s_\phi c_\theta & c_\phi c_\theta \end{bmatrix} \tag{41}$$

74

The wind velocities from the pitot static array are represented by

$$\hat{V}_P = \left\{ \hat{V}cos(\hat{\psi}) \quad \hat{V}sin(\hat{\psi}) \quad 0 \right\}^T \tag{42}$$

where $\hat{V}$ and $\hat{\psi}$ are the outputs from the algorithm. The angular velocity of the aircraft in the body frame is

$$\vec{w}_{B/I} = \left\{ p \quad q \quad r \right\}^T \tag{43}$$

which is measured by the aircraft inertial measurement unit (IMU). The distance from the aircraft body frame to the pitot static array is represented as:

$$\vec{r}_{B \to P} = \left\{ l \quad 0 \quad -h \right\}^T \tag{44}$$

where l is the distance of the pitot-static tube inlet from the aircraft center of mass and h is the height of the inlet from the aircraft center of mass. For simplicity, it is assumed that the flow around each pitot probe is equivalent. Although this is not exactly true, the distance between the pitot probes is small enough for this assumption to be valid. The velocity components of the aircraft in the inertial frame are

$$\vec{v}_{B/I} = \left\{ \dot{x} \quad \dot{y} \quad \dot{z} \right\}^T \tag{45}$$

which are measured by the aircraft on-board GPS.

3.7 Pitot Processing Summary

A diagram of the all processing steps for the pitot sensor is shown in Figure 52. The raw bits input from the four pitot probes are processed using truncation, low pass and complementary filters. A scaling factor is used to correct for differences between

each pitot probe. Data is then processed through the Fourier series pitot model and finally, processed through the kinematic model to output wind speed and direction.
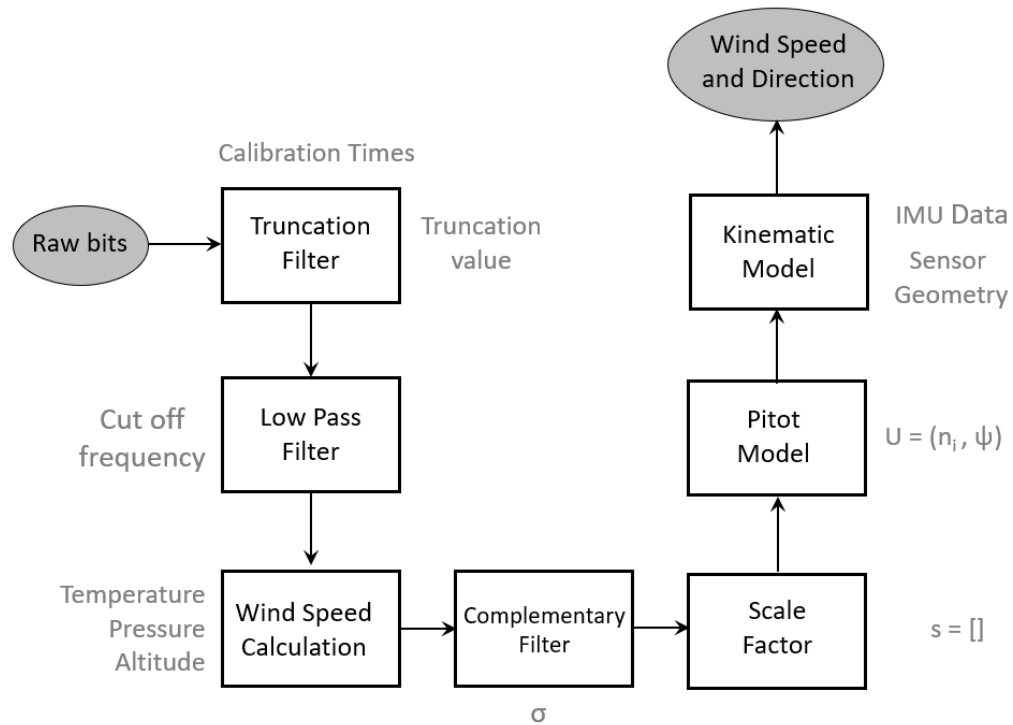
Figure 52. Processing for wind speed and direction output from pitot raw bits

CHAPTER IV

EXPERIMENTAL RESULTS

This chapter includes all experimental results from ground and flight testing of sensors, quadrotors and fixed-wing aircraft. Ground tests are performed to validate sensor measurements without quadrotor influence. Ground calibration for the FP4 sensor is detailed in Chapter III. Sensors are flown alongside a mesonet tower for in-flight calibration. Soundings are performed using quadrotors to characterize a vertical wind profile. The Apprentice fixed-wing aircraft is also tested with the FP4 sensor.

4.1 Ground Testing

Initial testing of the PTH BME280 sensors indicates that radiation shields may be necessary to eliminate solar radiation effects on temperature measurements. A radiation shield (Radiation Shield 2.0) was used that was designed from MakeXYZ, which is a 3D printing service that provides free 3D models files or printed pieces for purchase. Each wind speed measurement sensor was equipped with BME280 PTH sensors with and without radiation shields. A few iterations of the radiation shield were made, as shown in Figure 53, including Radiation Shield 1.0, the BME280 with no radiation shield, Radiation Shield 1.0 with the BME280 mounted upside down facing the platform, and Radiation Shield 2.0.

77
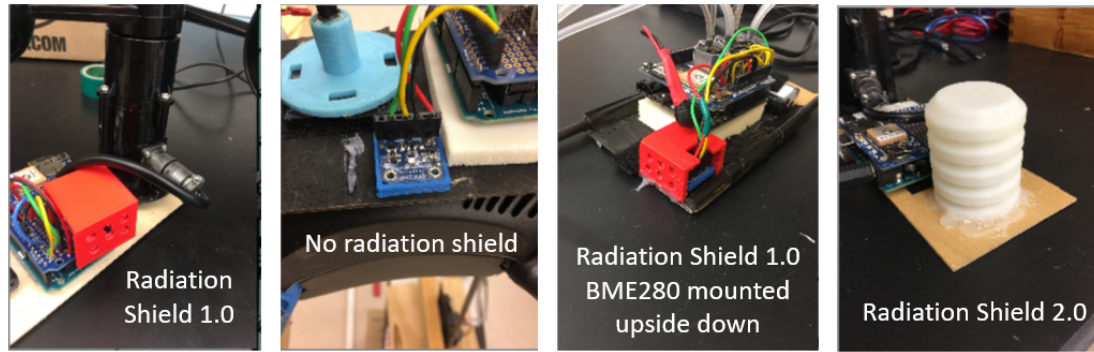
Figure 53. BME280 PTRH sensor with radiation shields

Each system contained the following:

1) Anemometer 1 - Radiation Shield 1.0

2) FP4V - No Radiation Shield

3) FP4H - Radiation Shield 1.0 with BME280 sensor mounted upside down

4) Anemometer 0 - Radiation Shield 2.0

5) SenseHAT - No Radiation Shield with Raspberry Pi (Not pictured)

Each sensor system was tested side-by-side to compare effects of solar radiation on measurements, as shown in Figure 54. These tests were performed near the South Alabama mesonet tower to compare to tower PTRH instruments on a partially sunny day on January 31, 2018.
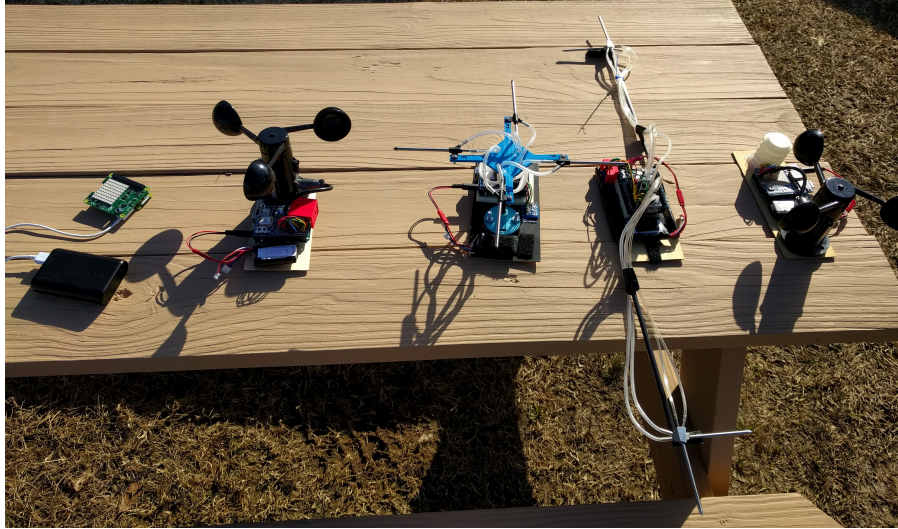
Figure 54. PTH sensors testing

Results from the 20 minute test compared to the mesonet tower are shown in Figure 55. According to local weather stations and the mesonet tower measurements, the temperature at the time of testing was approximately $17°C$. As expected, the FP4V sensor without a radiation shield performed the worst, with the most effect from solar radiation, showing measurements above $25°C$. Meanwhile, Anemometer 1 equipped with Radiation Shield 1.0 measured temperatures around $19°C$, which was closest to the tower measurements. Most temperature measurements from the BME280 sensor are not reliable however, with significant fluctuations, even when sensors are equipped with radiation shields. Pressure measurements for all sensor systems ranged from 1015.9 to 1016.9 hPa, while relative humidity ranged from 40 - 60 %. More testing is needed to fully quantify the effects of the radiation shields on temperature measurements. The sensors can be tested again on a fully cloudy day or a fully sunny day. Also, the sensors may need aspiration for proper measurements, so testing on a windy day could confirm this.

(a) Temperature ($°C$)   (b) Pressure (hPa)   (c) Relative Humidity (%)
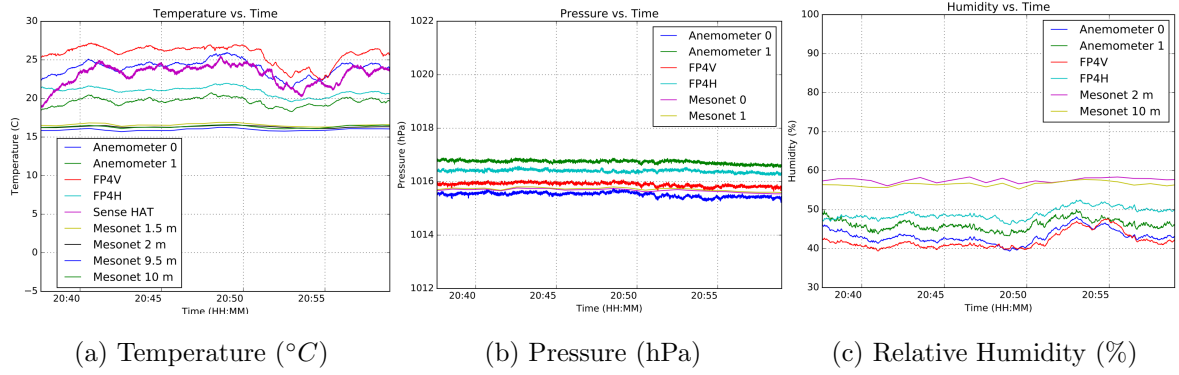
Figure 55. BME280 sensor PRTH testing

Two anemometers were tested side-by-side to validate filtered wind speed measurements, as shown in Figure 56. This test is considered Case 2, in which the sensors are tested while stationary (the velocity of the quadrotor is zero, V_Q) with atmospheric winds, V_A. Resulting wind estimations from the sensors, U_A, should then just be equal to V_A.

Case 2: Sensors stationary with atmospheric winds

$$\vec{V_Q} = 0$$

$$\vec{V_A} \neq 0$$

$$U_A = \|\mathbf{V_A}\|$$

Figure 56. Anemometer validation ground test

Scalar wind speed results for the two anemometers indicate that both sensors are capable of measuring atmospheric winds, within $0.2m/s$ of each other with a standard complementary filter, truncation filter and low-pass filter.
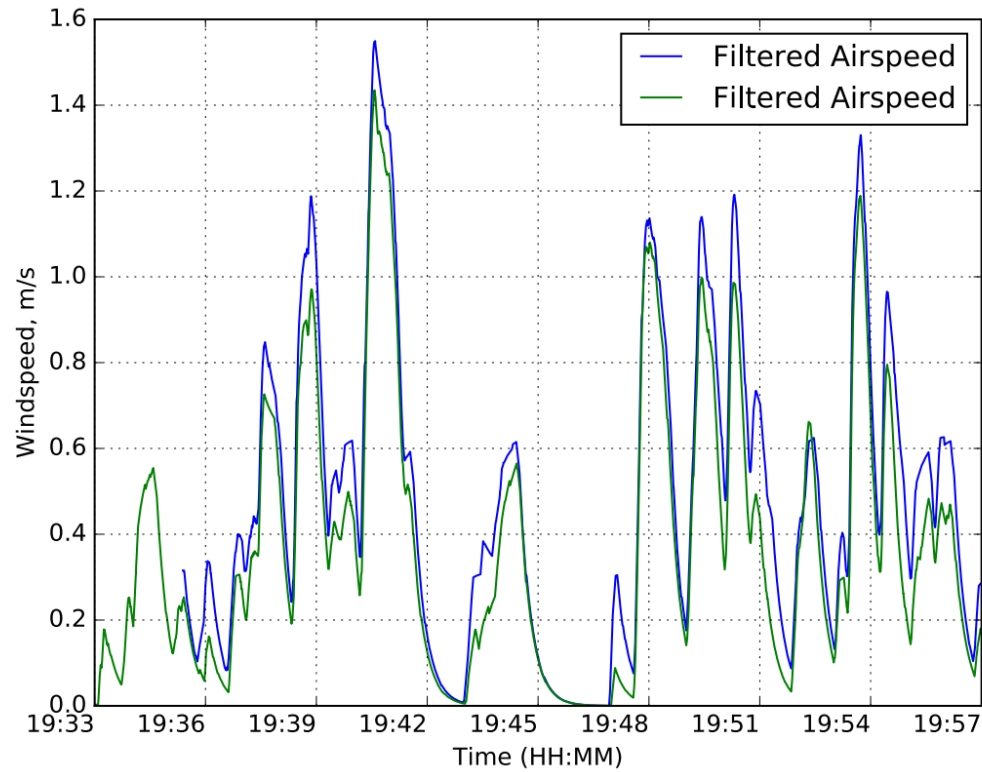
Figure 57. Anemometer scalar wind speed validation results

4.2 Flight Testing

After design and initial ground testing, the quadrotor equipped with sensors was tested in flight. The mobile atmospheric sensing system (MASS) utilizes wind measurement sensors and an iMet-XQ meteorological sensor with a commercially available Iris+ 3D Robotics quadrotor as a mobile platform. Equipped with both sensors, the MASS is capable of characterizing the atmosphere by measuring wind speed, atmospheric pressure, temperature and relative humidity and logging GPS data to a micro SD card. Wind speed data is recorded using a custom-built FMS mounted on the Iris+ quadrotor. The FMS combined with an Adafruit Pressure Temperature Humidity (PTRH) sensor make up a sensor called the FAST Pitot

82

(FP). A breakdown of the data collection capabilities of each component of the MASS is shown in Table 8.

Table 8. MASS data collection capabilities

Measurement	iMet-XQ	PTRH	AA	PSA	Iris+	Apprentice
Pressure	✓	✓			✓	✓
Temperature	✓	✓				
Relative humidity	✓	✓				
Wind speed			✓	✓		
Wind direction				✓		
GPS	✓	✓	✓	✓	✓	✓
IMU					✓	✓

Further testing and results from the iMet-XQ sensors and other atmospheric sensors can be found in the work done by Kimball, et al. [40].

4.2.1 Vicon Testing

The anemometer on-board the quadrotor was tested at the Autonomous Tracking and Optimal Measurements (ATOM) lab at the University of Alabama Huntsville (UAH). The ATOM lab is equipped with a Vicon motion capture system with 33 Vicon T40 series infrared (IR) cameras which can track objects up to 370 frames per second with a latency of 5 ms, and a spatial resolution of 1.5 mm [41]. The quadrotor was flown in the ATOM lab to test Case 3, in which the quadrotor velocity is non-zero with no atmospheric winds.

Case 3: Quadrotor motion with no atmospheric winds

83

$$\vec{V_Q} \neq 0$$

$$\vec{V_A} = 0$$

$$U_A = \|\mathbf{V_Q}\|$$

The quadrotor is shown in Figure 58 equipped with the anemometer and four tracking tape markers for the Vicon system. The quadrotor was flown in the 50 ft x 30 ft x 12 ft capture area of the ATOM lab and tracked by the IR cameras to determine aircraft speed, V_Q, which should equal the anemometer measured speed, U_A.
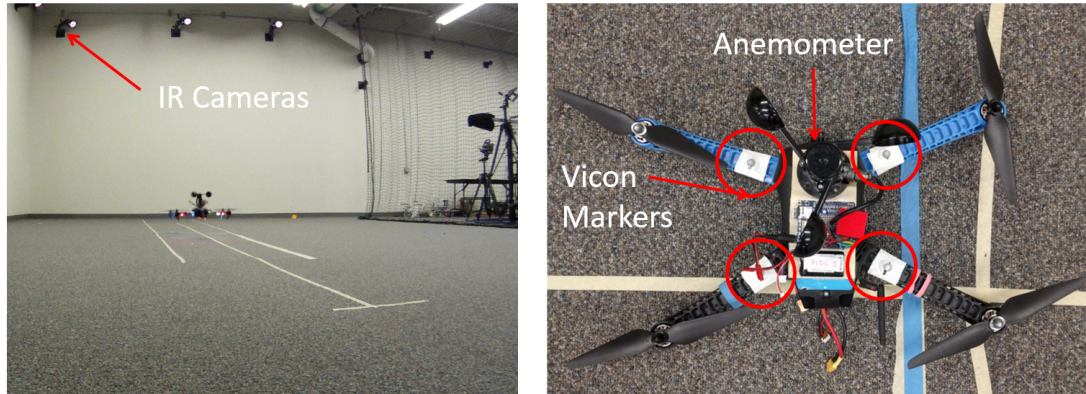
Figure 58. Quadrotor and anemometer Vicon test

For testing, the quadrotor was remotely piloted to move forward and then rearward with a heading angle equal to zero. The pilot then rotated the quadrotor by 90 degrees in yaw and performed the same maneuver with the quadrotor moving laterally. Results from ATOM lab flight testing in Figure 59 indicate that as expected, the direction of travel of the quadrotor has no effect on the reading from the anemometer, since it only reads scalar wind speed. The quadrotor experienced a rough takeoff, which is reflected in the absolute speed spike to 5 m/s between 10 and 20 seconds. During this takeoff, the aircraft rises, but the pilot does not

account for ground effect and reduces throttle too quickly at which point the quadrotor slams into the ground. Ground effect, or rotor downwash impacting the ground, circulates large enough that the anemometer experiences enough inflow to read a rather large velocity. Once the vehicle rises out of ground effect the anemometer reads no velocity. During aircraft landing at approximately 80 s, the anemometer experiences an inflow of 2 m/s. Overall, results indicate that there is potentially some de-synchronization issues in the data which are most likely attributed to hardware limitations of the Arduino Uno microcontroller used for logging wind speed measurements.
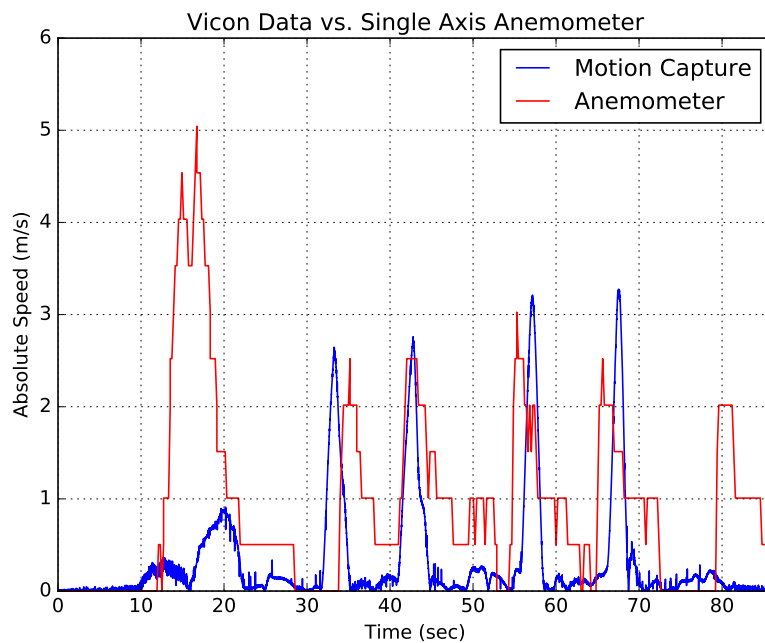
Figure 59. Quadrotor ATOM lab flight test absolute speed results

The quadrotor IMU data is also compared to data obtained from the Vicon IR cameras [42]. The roll, pitch and yaw of the quadrotor from the IMU and captured from the Vicon system is shown in Figure 60. The roll and pitch angles from the

85

quadrotor and Vicon system match well, while the yaw angles match only in the end due to the Extended Kalman filter removing bias from the data. This is likely because of the limitations of the magnetometer on board the quadrotor. The yaw angle begins to converge to the correct yaw angle from the Vicon once the dynamics of the quadrotor are excited, and the data from the magnetometer and accelerometer are combined to output the true yaw angle.

| (a) Roll angle | (b) Pitch angle | (c) Yaw angle |
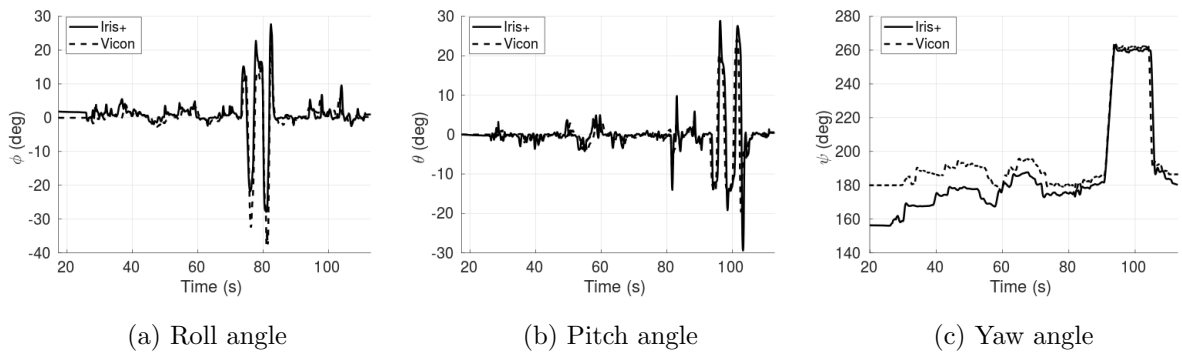
Figure 60. Quadrotor IMU data compared to Vicon-captured data

4.2.2 Pitot Mesonet Test

To calibrate sensors, the quadrotor was flown next to a 10 m mesonet tower on the University of South Alabama (USA) campus. The mesonet tower is equipped with a Vaisala HMP45C T/RH probe and a R. M. Young 05103 helicoid propeller anemometer with wind vane for directional orientation, which are installed at both 2 and 10 m. Two Vaisala pressure sensors are installed in the data logger enclosure at about 1.5 m height. Data is logged using one-minute averages for all mesonet tower sensors. A standard three-cup anemometer by Adafruit is placed at a height of 2.5 m near the mesonet tower for additional wind speed comparison. The

mesonet tower with meteorological instruments is shown in Figure 61 along with the Adafruit anemometer and the quadrotor for sensor calibration.
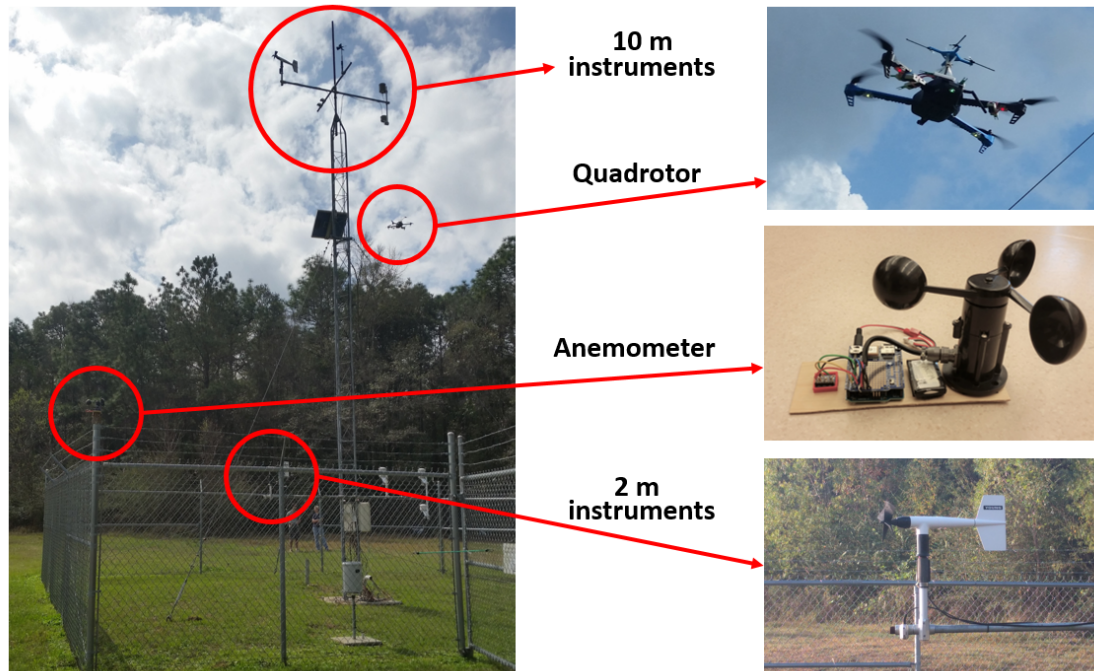
Figure 61. Mesonet calibration apparatus

After ground-based testing and validation of the flow measurement sensors, two quadrotors equipped with the atmospheric sensing packages were remotely piloted to hover alongside the mesonet tower at heights of 2 m and 10 m, as shown in Figure 62. These flight tests were used to calibrate the flow measurement sensors and develop algorithms for measuring wind speed in the lower atmospheric boundary layer. The procedure for flight testing is as follows. First, the sensors are equipped on the grounded quadrotors and then caps are placed on the ends of each pitot-static tube for thirty seconds for sensor calibration. The caps eliminate any external winds so that the mean data taken while the caps are on can be used to create a zero offset for wind speed data from the raw bits recorded. Next, the two

sensors are flown simultaneously on two Iris+ quadrotors on the east and west side of the mesonet tower at 10 m as shown in Figure 62b. After hovering next to the mesonet tower at an altitude of 10 m for 10-15 min, the quadrotors are landed and then flown individually at heights of 2 m next to the mesonet tower. Because of the close proximity of the quadrotor to the mesonet tower equipment at 2 m, only one quadrotor is flown at a time.

(a) Horizontal FMS flown at 2 m   (b) Dual sensor testing

Figure 62. Example mesonet tower sensor testing

Results from the dual sensor testing at the mesonet tower are shown in Figures 63 - 64. The altitude of each quadrotor equipped with each FMS, and the anemometer are shown in Figure 63a for the first 10 m AGL flight with both FMSs. Altitude is also shown for the second two flights at 2 m with the horizontal FMS and then the vertical FMS. The anemometer is shown at a fixed altitude of 1.5 m AGL next to the mesonet tower as shown in Figure 61. The scalar wind speed measurements of each sensor and the mesonet tower at both 2 and 10 m are shown in Figure 63b. The anemometer provides measurements close to the mesonet tower at 2 m; however, the two FMSs both significantly underestimate wind speed at both 2 and 10 m AGL.

Note that the wind speed data extracted from this experiment only utilizes the scalar component of the positive readings, with negative values of pitot components set to zero. This was the original design of the sensor before the half range cosine Fourier series was determined for estimating wind speed from data measurements.

(a) Altitude (m) vs. time (HH:MM)   (b) Scalar wind speed (m/s) vs. time (HH:MM)
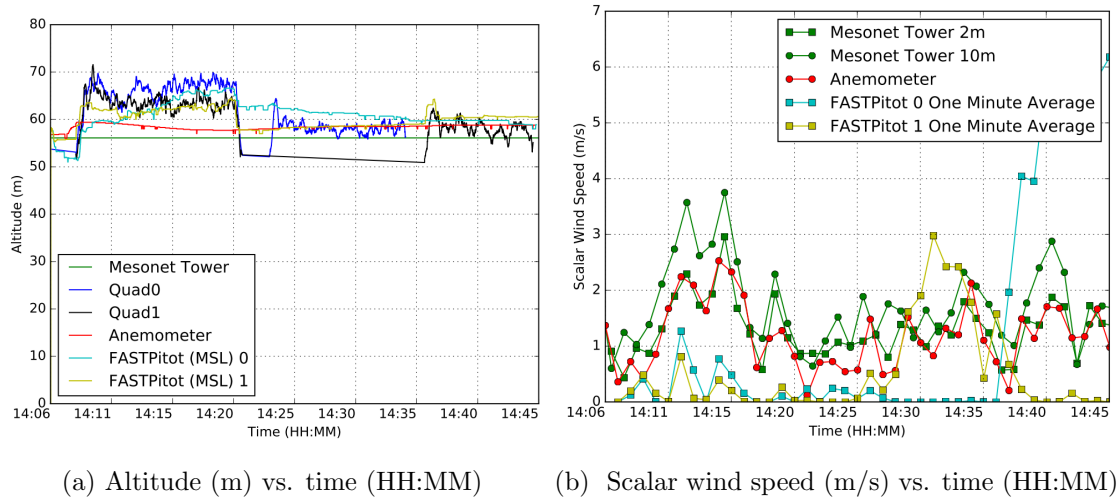
Figure 63. Mesonet tower dual sensor testing results

Pressure (kPa), temperature ($°C$) and relative humidity (%) for both quadrotors equipped with the horizontal FMS and vertical FMS, the anemometer at 1.5 m and the mesonet instruments at 2 and 10 m are shown in Fig. 64. As expected, the pressure reading (kPa) drops significantly for both quadrotors during the 10 m flights between 14:10 and 14:20 and minimally during the 2 m flights between 14:22 and 14:45. The pressure readings for the anemometer remain consistent with the mesonet tower pressure readings. As shown in Fig. 64b, the mesonet tower provides stable temperature measurements around $22°C$ for the entire duration of the flight test, while the anemometer, and the FP4 and FP4V sensors provide measurements ranging from $23°C$ to $38°C$. The drastic temperature increase for the FP4V sensor

89

between 14:25 and 14:40 could be due to overheating of the electronics from solar radiation which can be mitigated with the use of a radiation shield, as described in Chapter II. Percent relative humidity, shown in Fig. 64c, is stable with an average relative humidity of 65 % for the mesonet tower instruments, while the anemometer provides measurements around 10 % lower. The FP4 sensor provides more accurate relative humidity measurements with an average value around 61% while the FP4V sensor fluctuates drastically with an average value around 50%. Inaccuracies are likely due to sensor heating, causing the saturation vapor pressure to increase and the relative humidity to decrease. Further analysis is needed to fully investigate and quantify these inaccuracies.

(a) Pressure (kPa)   (b) Temperature (°C)   (c) Humidity (%)
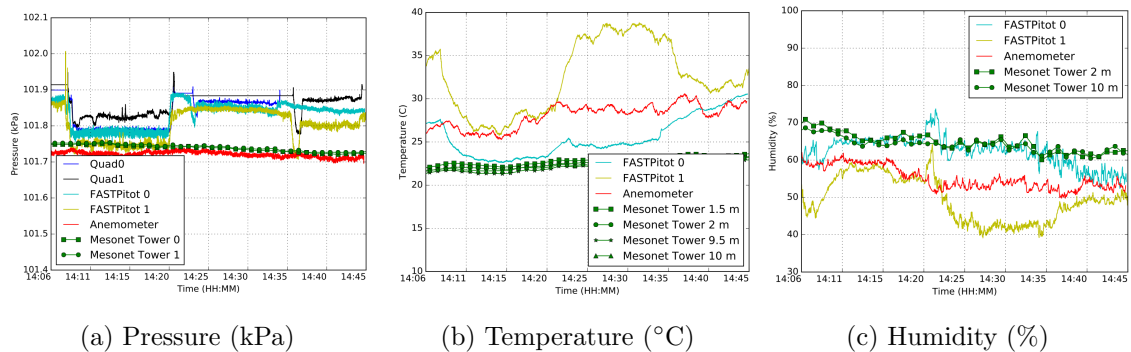
Figure 64. Pressure, temperature and relative humidity vs. time mesonet testing

The sensors were tested again on the quadrotor flown in a square pattern around the mesonet tower. The purpose of this flight pattern is to aspirate the sensors so that the inflow of wind provides a large pressure differential for the pitot sensors. The lateral speed of the quadrotor is then subtracted from the wind speed data using the quadrotor IMU data and the kinematic model. This test case is considered Case 4, in which the quadrotor velocity is non-zero and the atmospheric winds are non-zero:

Case 4: Quadrotor motion with atmospheric winds

$$\vec{V_Q} \neq 0$$

$$\vec{V_A} \neq 0$$

$$U_A = \|\mathbf{V_Q}\| + \|\mathbf{V_A}\| + B_Q$$

where B_Q is a correction factor for velocity from the bias of the quadrotor. The flight path of the quadrotor around the mesonet tower is shown in Figure 66a. The roll and pitch of the quadrotor from the IMU are shown in Figure 65b.

(a) X versus Y (m)   (b) Roll and pitch (°) versus time
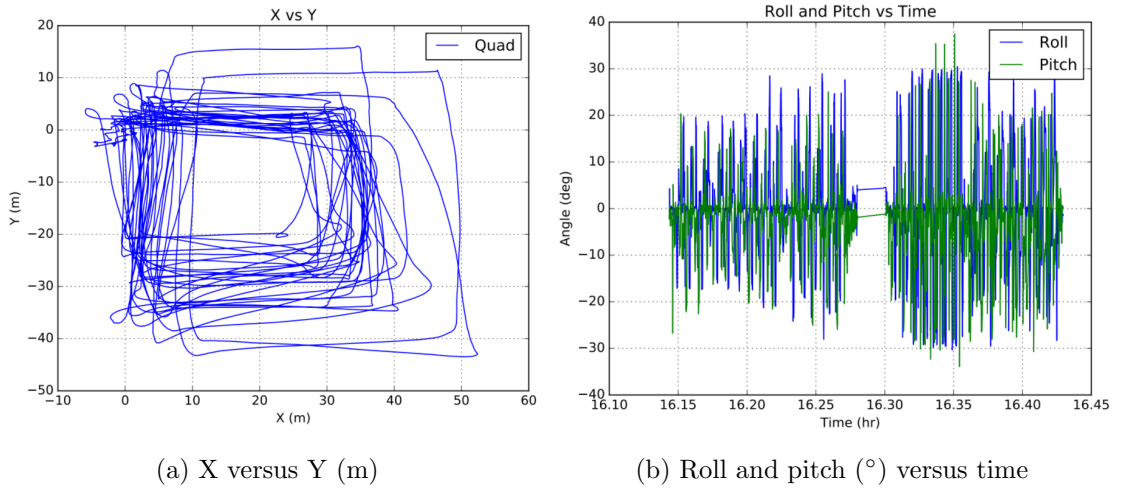
Figure 65. Quadrotor square pattern flight positions

Scalar wind speed and direction results from the square pattern mesonet flight test are shown in Figure 66. The kinematic model outlined in Section 3.6 was used to subtract the rotational and lateral speeds of the quadrotor to more accurately estimate wind speed and direction. During the square pattern path, the FP4V significantly overestimates wind speed using the algorithm, and does not accurately capture wind direction.

91
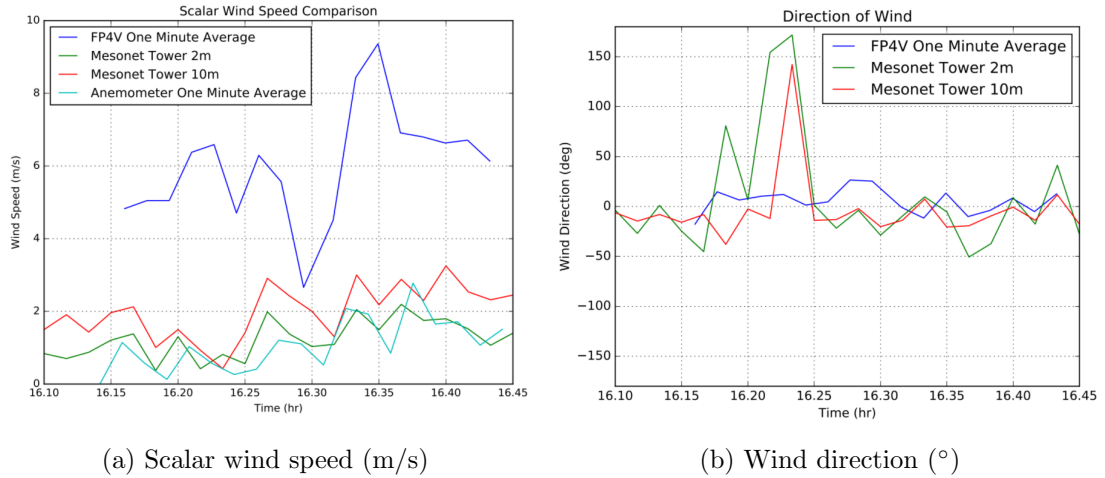
(a) Scalar wind speed (m/s)

(b) Wind direction (°)

Figure 66. Quadrotor square pattern flight wind measurements

The algorithm and model clearly need more adjustment and do not reflect actual wind speed or direction well. This could possibly be from a data synchronization issue between the IMU and pitot sensors. As shown in Figure 67, the raw data for wind direction (°) filtered using the algorithm achieves a maximum wind direction of about 125°, which is close to the actual wind direction of 140° measured by the mesonet tower 10 m instruments. This maximum value for wind direction at about 16:30 is not reflected in Figure 66b, which measures a maximum wind direction of 25°. Desychronization between data is likely the cause of the algorithm output issue for wind measurements, since several data streams from different sensors are stitched together. A more sophisticated sensor with accurate GPS, and higher data logging capabilities to one microcontroller is needed for future testing.

92
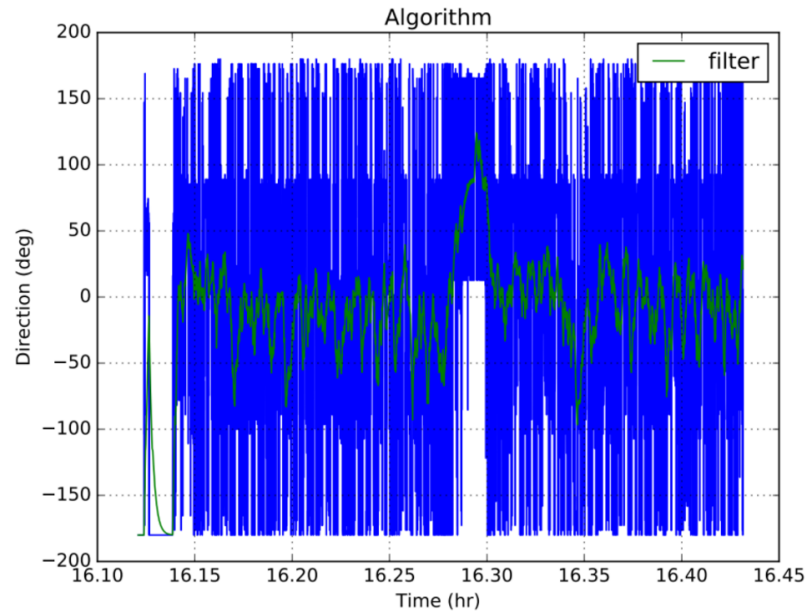
Figure 67. Square pattern wind direction results from algorithm

4.2.3 Anemometer Mesonet Test

A 3-cup anemometer was flown onboard the quadrotor to determine the impact of the quadrotor on scalar wind measurements. One anemometer (Anem 1) was placed on the quadrotor as shown in Figure 68a. A second anemometer (Anem 0) was placed at a height of 2 m on the mesonet fence as shown in Figure 68b to compare to the anemometer onboard the hovering quadrotor. The quadrotor with Anem 1 was remotely piloted to hover next to the fixed anemometer for about ten minutes.

93

(a) Top down of anemometer
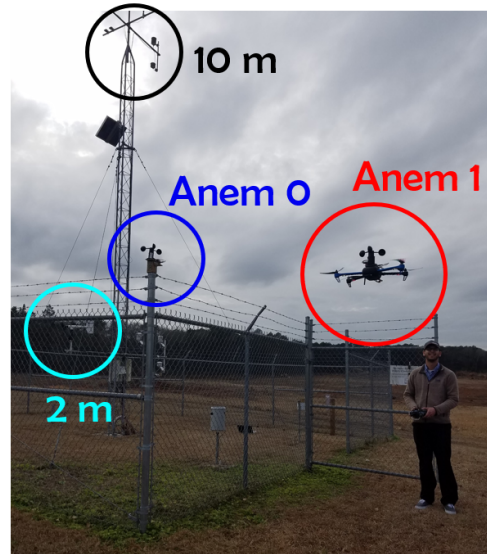
(b) Anemometer flight test

Figure 68. Mesonet anemometer flight test

Scalar wind speed results from flight testing are shown in Figure 69 with raw wind speed data taken at 5 Hz and wind speed 1-minute averages. Anem 1 equipped on the hovering quadrotor captured the wind speed fluctuations with an average bias around 1 m/s higher than Anem 0. Between 600 and 700 seconds, both anemometers measured a wind gust of 5.5 m/s with almost no error - showcasing the increased accuracy associated with higher wind speeds.
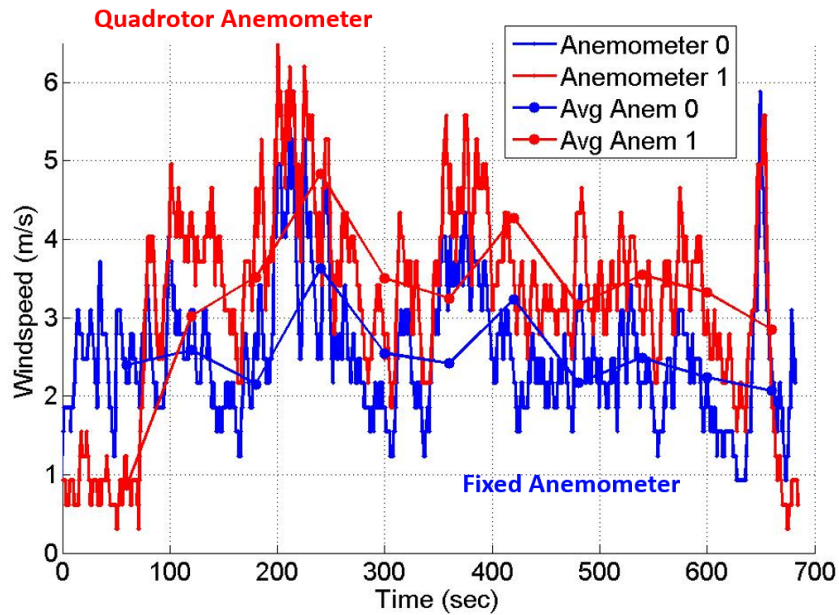
Figure 69. Raw data and anemometer 1-minute averages

Data from both anemometers processed with 1-minute averages against the mesonet 2 m and 10 m wind speed measurements are shown in Figure 70. Interestingly, Anem 1 equipped on the quadrotor matches wind speeds more closely to those obtained from the mesonet tower instruments at 10 m, although Anem 1 was at the same height as Anem 0 at 2 m. This difference is expected, however, given the influence of the quadrotor motion on wind speed measurements.

95
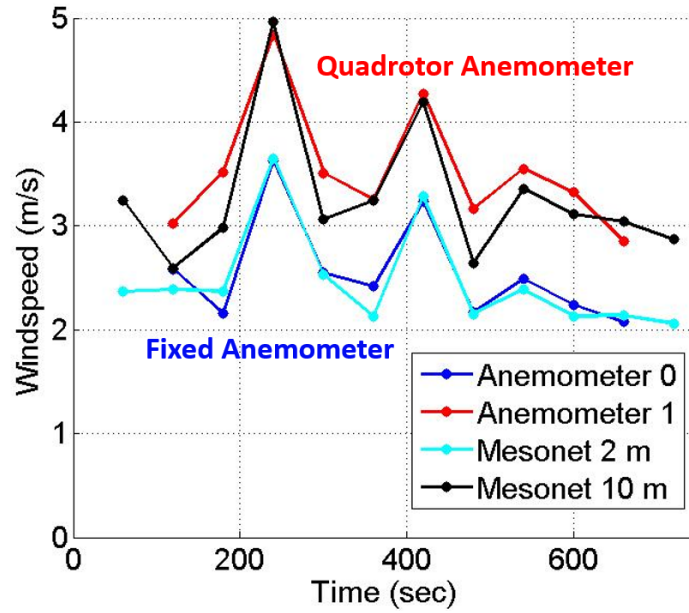
Figure 70. Anemometer 1-minute averages against mesonet

The average absolute error between Anem 0 and Anem 1 is 0.97 m/s. By
subtracting this value, B_Q, from the hovering anemometer wind speed
measurements, a corrected wind speed for Anemometer 1 can be established, as
shown in Figure 71a. The average absolute error between Anemometer 0 and the
Mesonet 2 m measurements is 0.11 m/s and between Anemometer 1 and the
Mesonet 2 m is 0.16 m/s, as shown in Figure 71b. The RMSE between the two
anemometers is 0.2406 m/s. This, however, is a crude method for correcting wind
speed, as it is almost impossible, in this case, to isolate the effects of the rotor
downwash on wind speed measurements. Many factors could affect the increased
wind speed measurements of the anemometer onboard the quadrotor, such as the
spatial distance away from the mesonet sensors and fixed anemometer. Without
further testing, the correction factor determined from this test cannot be validated.

96
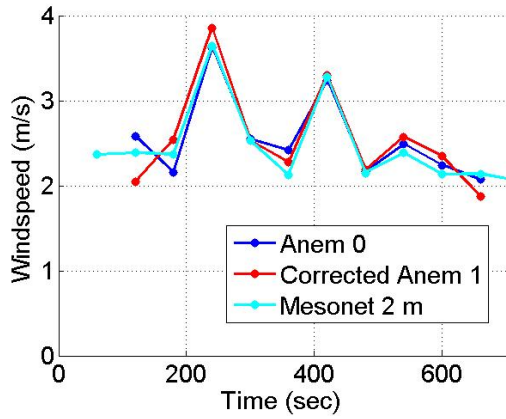
(a) Corrected anemometer (b) Anemometer flight test
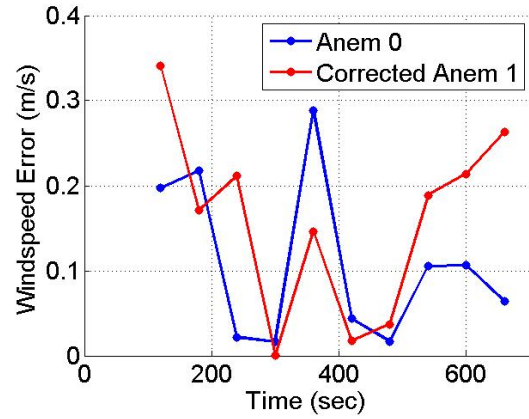
Figure 71. Mesonet anemometer flight test

4.2.4 Sensor Soundings

For comparison of the quadrotor flow measurement sensors, each of the two sensors were equipped on one of two Iris+ quadrotors, shown in Figure 72, and tested in flight. Both quadrotors equipped with the sensors were remotely piloted and flown simultaneously to a height of 100 m AGL while an anemometer was placed at ground level for a wind speed data baseline.

Figure 72. Flow measurement sensor dual sounding

97

The altitude of each quadrotor is depicted in Figure 73a showing ascent and descent of the quadrotors during the two 100 m AGL flights and the altitude of the anemometer fixed on the ground at 22 m MSL. The altitudes of the two FMSs were also recorded, but results show how inaccurate GPS data can be with a maximum altitude of 100 m for the horizontal FMS while the quadrotor reached a maximum altitude of 130 m during the first ascent. Scalar wind speed (m/s) as a function of pressure altitude (m) is shown in Fig. 73b for the two flow measurement sensors on board the quadrotors. Altitude was determined using the relation between changes in pressure, rather than altitude from GPS, since GPS provides less accuracy. Results indicate that scalar wind speed is highly variant and time dependent, and there is a correlation between higher wind speeds and higher altitude. This is expected due to surface frictional effects.

(a) Altitude (m) vs. time (HH:MM)   (b) Altitude (m) vs. scalar wind speed
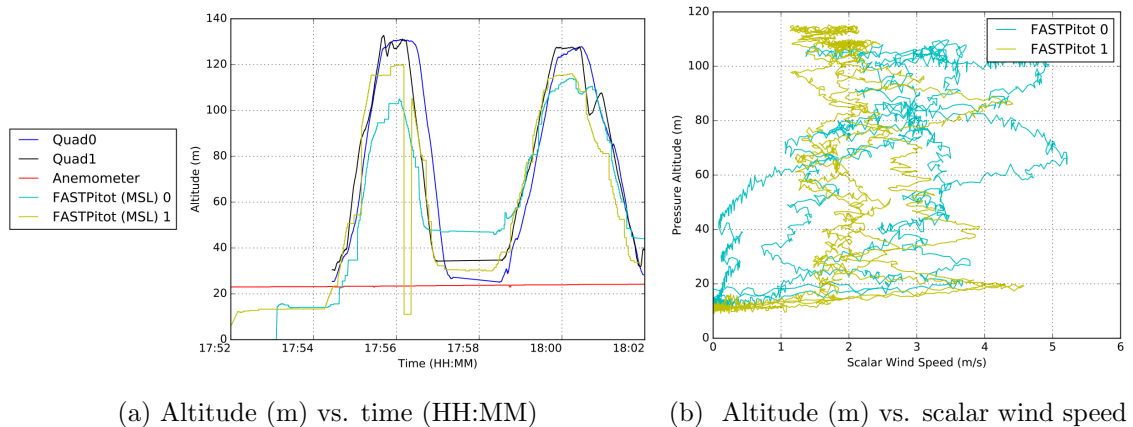
Figure 73. Dual sensor sounding flight test results

Scalar wind speed (m/s) as a function of time for the anemometer and two flow measurement sensors are shown in Figure 74. The anemometer recorded an average wind speed of about 1.0 m/s at a fixed altitude of 22 m, while the wind speed

recorded by the two flow measurement sensors varied with their changes in altitude. At time 17:59, when all three sensors were at ground level in between soundings, the three sensors recorded a scalar wind speed value of 1.4 m/s, indicating the two flow measurement sensors are calibrated properly compared to the anemometer. During soundings, however, the the horizontal flow measurement sensor records a scalar wind speed approximately 1.5 m/s higher than the vertical sensor at maximum altitude. This may indicate bias in the sensor data that can potentially be mitigated using a correction factor for each pitot-static tube. It is important to note, however, that although the two quadrotors were at approximately the same altitude, they were separated laterally by approximately 30 m. It is possible that local turbulence is the cause for the discrepancy between sensors, especially given the relatively close scalar wind values.
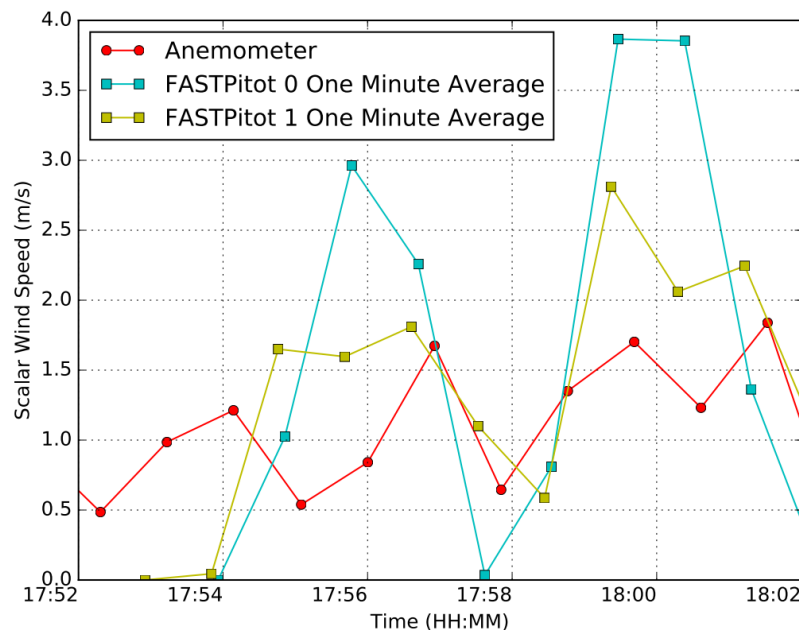
Figure 74. Dual sensor sounding scalar wind speed (m/s) vs. time

The pressure readings (kPa) recorded from the two quadrotors, the two FMSs and the anemometer during the two soundings are shown in Figure 75a. These results show the fixed pressure reading of 100.9 kPa for the anemometer at ground level and an expected drop in pressure to 99.8 kPa as the quadrotors climb in altitude. Temperature ($°C$) of the two FMSs and the anemometer are shown in Fig. 75b. Although the temperature for the anemometer fluctuated between $36°C$ and $42°C$ the trend is generally decreasing, and follows the same decreasing trend for the two FMSs. As expected, the temperature drops for both FMSs as the quadrotors climb in altitude; however, the horizontal sensor shows a temperature reading bias of about $-5.5°C$. The relative humidity for the anemometer, shown in Figure 75c remains relatively fixed at approximately 30% at ground level, while the relative humidity readings for the two FMSs change similarly with altitude changes, again with a bias for one sensor of approximately 5%.

(a) Pressure (kPa)   (b) Temperature (°C)   (c) Relative humidity (%)
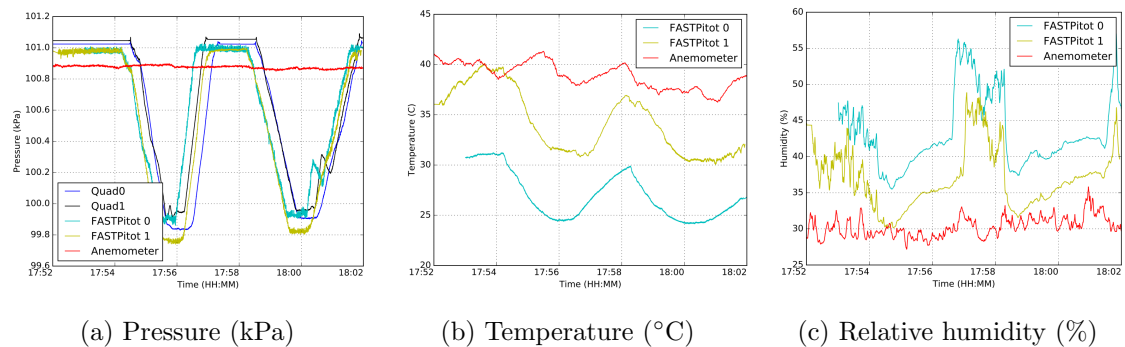
Figure 75. Pressure, temperature and relative humidity vs. time (HH:MM)

Furthermore, pressure, temperature and relative humidity are shown as a function of altitude in Fig. 76. As expected, both pressure and temperature are inversely related to altitude and decrease as altitude increases. As shown in Fig. 76c, relative

100

humidity remains relatively constant as altitude increases, but fluctuates at ground level.

(a) Pressure (kPa)   (b) Temperature (°C)   (c) Relative humidity (%)
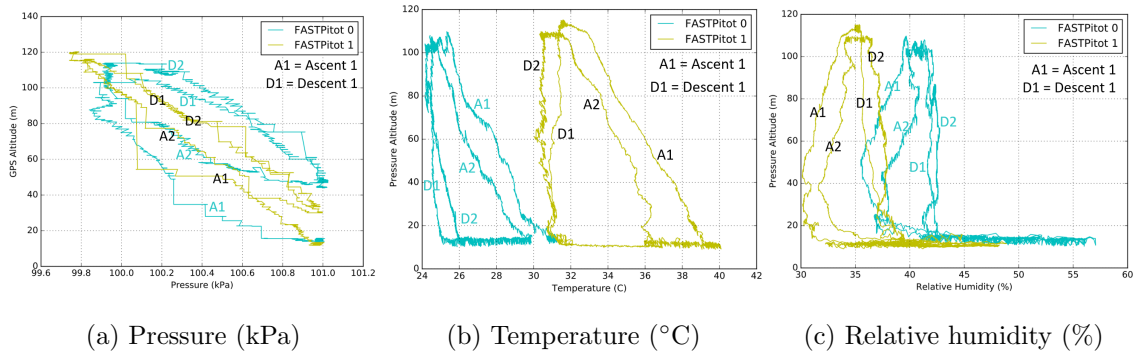
Figure 76. Altitude (m) vs. pressure, temperature and relative humidity

4.2.5 Quadrotor Flight Tests Summary

The four experimental test cases for wind measurement sensors and quadrotor motion were evaluated for determining atmospheric winds, U_A. Table 9 summarizes the experimental test cases performed for both the FP4 pitot probe sensor and 3-cup anemometer. Case 1 was tested for both the FP4 and anemometer with indoor ground testing of the quadrotor stationary with no atmospheric winds. The anemometer was fully tested for Case 2, with outdoor ground testing of the quadrotor stationary with atmospheric winds. Both sensors were also tested in a wind tunnel with known wind speeds and wind direction. Although the FP4 was tested indoors, it was only partially tested with atmospheric winds, since it was not tested outdoors in low wind speed conditions. Case 3 for quadrotor motion with no atmospheric winds was tested only for the anemometer with the indoor Vicon equipment in the ATOM lab. Both wind measurement sensors were tested for Case 4, with quadrotor motion with atmospheric winds. The two sensors were tested in

101

hover onboard the quadrotor next to the mesonet tower, while the FP4V was additionally tested in a square pattern around the mesonet tower for aspirating the sensor.

Table 9. Test cases summary for FP4 and anemometer

Sensor	FP4	Anem	Test Case Description
Case 1	X	X	Quadrotor stationary with no atmospheric winds
Case 2	/	X	Quadrotor stationary with atmospheric winds
Case 3		X	Quadrotor motion with no atmospheric winds
Case 4	X	X	Quadrotor motion with atmospheric winds

Additional testing is needed for both sensors to validate experimental results from various ground and flight tests. The FP4V pitot probe sensor was only partially tested for Case 2, and not tested at all for Case 3, with quadrotor motion with no atmospheric winds. This jump from Case 1 to Case 4 was too quick, and did not allow for the problems of the FP4V to be incrementally tested to isolate variables and the factors influencing wind speed and direction measurements.

4.2.6 Aircraft Flight Testing

Multiple MASS were remotely piloted at the Irvington Airfield to show an example flight path with multiple aircraft. The quadrotor was equipped with the FP4V sensor as shown in Figure 77, and the Apprentice fixed-wing aircraft was equipped with a pitot sensor and iMet-XQ sensor, as shown in Figure 78.

102

Figure 77. Multi-MASS remotely piloted flight test

The pitot probe and iMet-XQ mounted on the Apprentice are shown in Figure 78. The pitot sensor was placed under the wing away from the propeller to avoid influence on the wind speed measurement. The electronics for the pitot sensor were placed inside a compartment in the center of the fuselage underneath the wing.
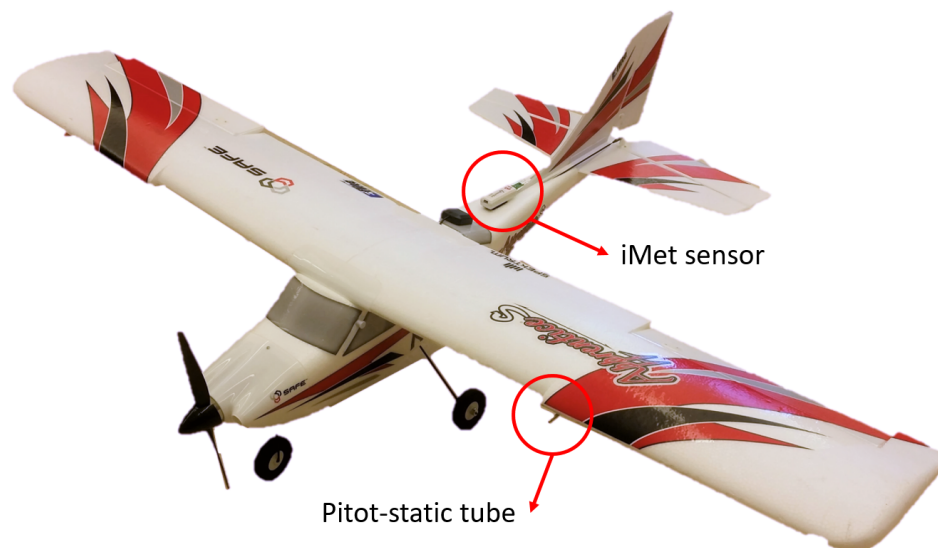
Figure 78. Apprentice with sensors

103

The quadrotor MASS was remotely piloted to fly in a pre-determined grid pattern at a fixed altitude and the fixed-wing MASS was flown in a spiral pattern around the quadrotor, as shown in Figure 79. The quadrotor flight path is shown in blue and the Apprentice flight path is shown in red. In the future, the quadrotor can be given set waypoints using a flight program to fly autonomously, rather than directing the pilot to manually fly in an approximate grid pattern.

(a) Latitude (°) versus longitude (°)　　(b)　Altitude (m) versus X (m) and Y (m)
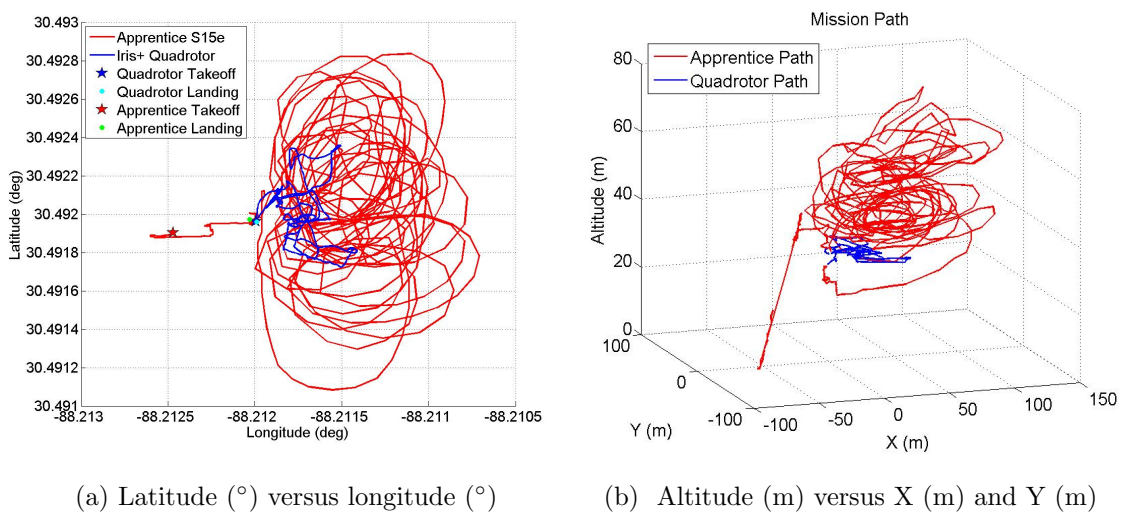
Figure 79. Multi-MASS example flight mission path

Wind speed data was not extracted for this flight test, and the aircraft trajectories are shown as an example. The test can be repeated with multiple autonomous aircraft flying at different altitudes to sample a wind field.

4.2.7 Apprentice Flight Testing

The Apprentice fixed-wing aircraft was tested with the FP4V sensor at the Irvington Airfield on March 15, 2018 at approximately 4:23 PM. The sensor was fixed on the Apprentice with the anemometer 2 m above the ground and is shown in Figure 80.

104

(a) Apprentice with FP4V sensor   (b) Apprentice in flight

Figure 80. Apprentice fixed-wing flight test with FP4V sensor

The purpose of this flight test was to assess the portability of the FP4V sensor on a mobile platform other than the quadrotor and to validate the wind speed and direction algorithm. Since the fixed-wing aircraft was flown at a higher speed than the quadrotor, the measurements from the pitot sensors should provide accurate wind speeds if the aircraft velocity is accurately subtracted using the kinematic model. The flight path of the fixed-wing aircraft flown in large spirals is shown in Figure 81a. The roll and pitch of the fixed-wing aircraft from the IMU are shown in Figure 81b.

(a) X versus Y (m)

(b) Roll and pitch (°) versus time
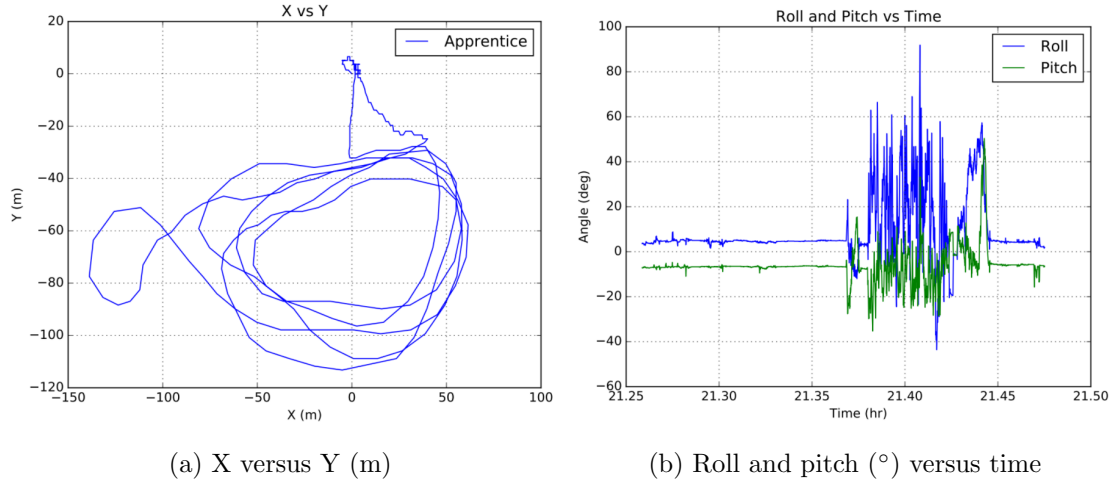
Figure 81. Apprentice FP4V flight tests

Scalar wind speed and direction results from the Apprentice flight test are shown in Figure 82. Data from the single pitot probe fixed to the aircraft wing are also extracted.

(a) Scalar wind speed (m/s)

(b) Wind components
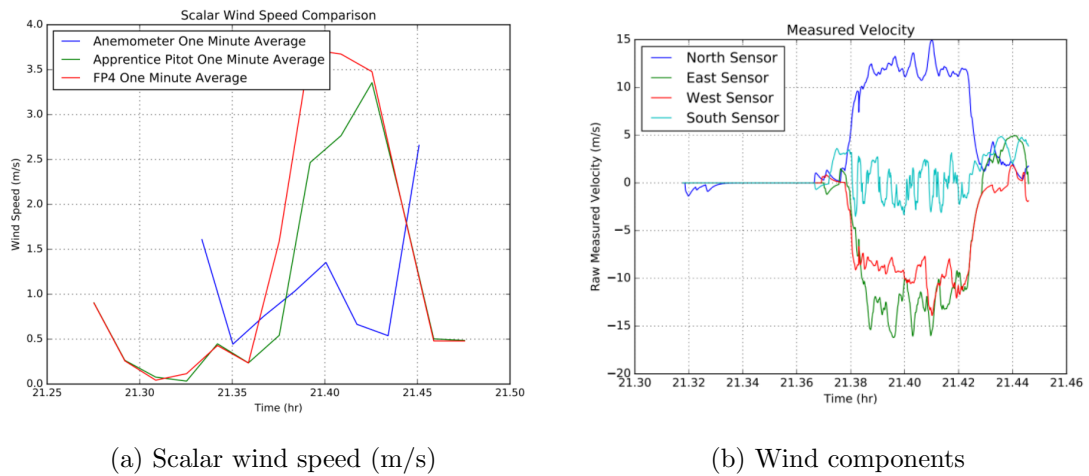
Figure 82. Pitot sensor results from Apprentice flight

106

Figure 82 shows the raw data from the fixed-wing flight. It is clear that the main winds are hitting the North sensor, which for this flight was pointing from the nose of the aircraft. The East and West sensors are reading negative values while the South sensor is reading approximately 0 m/s. The algorithm produces a scalar wind speed of approximately 15 m/s due North. However this "due North" is in the body frame of the aircraft. The issue with extracting the atmospheric wind speed is properly determining the heading angle of the aircraft (IMU+GPS) and the translational velocity of the GPS. With the GPS only obtaining measurements at 4Hz and the hardware limitations of the UNO, the results are not as promising as expected. More work is needed to validate experimental tests.

CHAPTER V

CONCLUSIONS

This research presents a mobile atmospheric sensing system which is calibrated using a wind tunnel, tested in flight and modeled in simulation. The mobile atmospheric sensing system (MASS) is relatively inexpensive and the custom-built wind measurement sensor is portable across multiple platforms. The FP4V sensor was designed specifically for an Iris+ quadrotor, but can be used on multiple rotary platforms. The sensor was tested on both the Iris+ and an Apprentice S15e fixed-wing aircraft. The concept of operations for utilizing multiple atmospheric platforms for sampling the atmosphere was established and simulated using the WRF model and MaaWM tool. Using a quadrotor and fixed-wing aircraft, the two equipped with wind measurement sensors are able to sample the atmosphere with correlation coefficients of 0.9938, 0.9904 and 0.9942 for the U, V, and W wind components, respectively. Multiple wind measurement sensors were compared and evaluated based on cost, accuracy and weight, given constraints of the mobile platform. To quantify the impacts of the mobile platform on wind estimations, several experimental test cases were evaluated. The resultant estimation of atmospheric winds, U_A, is dependent on several factors, including the quadrotor velocity, V_A, angular rotation, and empirical model for the pitot static array. The sensors are calibrated using scaling factors and ground-based and flight-based correction factors. The following test cases were evaluated:

Case 1: Quadrotor stationary with no atmospheric winds

$$\vec{V_Q} = 0$$

108

$$\vec{V_A} = 0$$

$$U_A = 0$$

Case 2: Quadrotor stationary with atmospheric winds

$$\vec{V_Q} = 0$$

$$\vec{V_A} \neq 0$$

$$U_A = \|\mathbf{V_A}\|$$

Case 3: Quadrotor motion with no atmospheric winds

$$\vec{V_Q} \neq 0$$

$$\vec{V_A} = 0$$

$$U_A = \|\mathbf{V_Q}\|$$

Case 4: Quadrotor motion with atmospheric winds

This case includes the quadrotor in hover, flown in a square pattern, and soundings.

$$\vec{V_Q} \neq 0$$

$$\vec{V_A} \neq 0$$

$$U_A = \|\mathbf{V_Q}\| + \|\mathbf{V_A}\| + B_Q$$

where B_Q is a correction factor for bias from the quadrotor.

5.1 Future Work

The MASS, specifically the wind measurement sensor, can be improved in various ways. Although the sensor was shown to work for a variety of test cases, the sensor still could not provide reliable data for in-situ flight tests such as soundings and even hover experiments next to the Mesonet tower. Some ways to improve the sensor include modeling the quadrotor in a subsonic wind tunnel to test the indirect method of wind extraction. This could help improve the control system on the quadrotor to stabilize the platform and potentially keep the translational velocity of the vehicle to zero. This however, will not solve the problem of aspirating the sensor

109

to move measurements out of the low speed wind region. During the square pattern flight, the quadrotor must rotate by a large pitch and roll angle. To mitigate this, it would be beneficial to gimbal the sensor to remove all angular motion or even gimbal the rotors on the vehicle so that the body of the vehicle remains horizontal while the rotors move in three dimensions. This would undoubtedly create new rotor propwash that would need to be modeled using CFD or wind tunnel testing. Another vehicle upgrade could be to move from a quadrotor to an octocopter as well as upgrade the wind measurement sensor to a 2D or 3D anemometer. The issue, of course, is that the entire system will no longer be "low-cost". Thus, a simple way to keep costs low would be to upgrade the microcontroller from an Arduino UNO to an Arduino DUE microcontroller. The DUE is about $25 more but has ten times the clock speed of an Arduino UNO. The benefit of this would be to reduce the amount of de-synchronization from timing issues and include an IMU on board the pitot static array so that all information needed for the kinematic equation is on one sensor. More experiments can be run with this new sensor or platform to create a reliable mobile atmospheric sensing system.

Future work will include:

1. Additional sensor testing (ultrasonic anemometers, multi-hole probes)

2. Additional platform testing (quadrotors, octocopter)

3. Wind tunnel testing of quadrotor equipped with sensors

3.1. FP4V calibration wind tunnel tests (1 Hz each)

4. Sensitivity analysis of pitot probes

5. CFD modeling of rotor propwash

6. Additional soundings and PTRH testing

7. Improved microcontroller processing using Arduino Mega 9DOF or Raspberry Pi

8. Implementation of quadrotor IMU as wind measurement sensor

REFERENCES

REFERENCES

[1] John Roy Garratt. The atmospheric boundary layer. *Earth-Science Reviews*, 37(1-2):89–134, 1994.

[2] Stefan Emeis, Klaus Schäfer, and Christoph Münkel. Surface-based remote sensing of the mixing-layer height–a review. *Meteorologische Zeitschrift*, 17(5):621–630, 2008.

[3] John Roy Garratt. Review: the atmospheric boundary layer. *Earth-Science Reviews*, 37(1-2):89–134, 1994.

[4] Gregor Giebel, Uwe Schmidt Paulsen, Jens Bange, Anders La Cour-Harbo, Joachim Reuder, Stephanie Mayer, Aline van der Kroonenberg, and John Mølgaard. Autonomous aerial sensors for wind power meteorology-a pre-project. Technical report, Danmarks Tekniske Universitet, Risø Nationallaboratoriet for Bæredygtig Energi, 2012.

[5] Benjamin L Hemingway, Amy E Frazier, Brian R Elbing, and Jamey D Jacob. Vertical sampling scales for atmospheric boundary layer measurements from small unmanned aircraft systems (suas). *Atmosphere*, 8(9):176, 2017.

[6] Alexey Bulgakow, Sergey Emelianov, Thomas Bock, and Daher Sayfeddine. Inspection of flyover bridges using quadrotor. In *ISARC. Proceedings of the International Symposium on Automation and Robotics in Construction*, volume 32, page 1. Vilnius Gediminas Technical University, Department of Construction Economics & Property, 2015.

[7] ML Hill, TG Konrad, JH Meyer, and JR Rowland. A small, radio-controlled aircraft as a platform for meteorological sensors. 1970.

[8] Juan Jesús Roldán, Guillaume Joossen, David Sanz, Jaime del Cerro, and Antonio Barrientos. Mini-uav based sensory system for measuring environmental variables in greenhouses. *Sensors*, 15(2):3334–3350, 2015.

[9] Caroline M Kiefer, Craig B Clements, and Brian E Potter. Application of a mini unmanned aircraft system for in situ monitoring of fire plume thermodynamic properties. *Journal of Atmospheric and Oceanic Technology*, 29(3):309–315, 2012.

[10] DN Axford. On the accuracy of wind measurements using an inertial platform in an aircraft, and an example of a measurement of the vertical mesostructure of the atmosphere. *Journal of Applied Meteorology*, 7(4):645–666, 1968.

[11] Ainsworth, J. E., D. F. Fox, and H. E. LaGow. Upperatmosphere structure measurement made with the pitotstatic tube. *Journal of Geophysical Research*, 66.10, 1961.

[12] Langelaan, J W., Nicholas Alley, and James Neidhoefer. Wind field estimation for small unmanned aerial vehicles. *Journal of Guidance, Control, and Dynamics*, 34.4, 2011.

[13] Neidhoefer J. Langelaan J., Alley N. Wind field estimation for small unmanned aerial vehicles. In *AIAA Guidance, Navigation and Control Conference Toronto, Canada*, 2010.

[14] Patrick P Neumann and Matthias Bartholmai. Real-time wind estimation on a micro unmanned aerial vehicle using its inertial measurement unit. *Sensors and Actuators A: Physical*, 235:300–310, 2015.

[15] Am Cho, Jihoon Kim, Sanghyo Lee, and Changdon Kee. Wind estimation and airspeed calibration using a uav with a single-antenna gps receiver and pitot tube. *IEEE transactions on aerospace and electronic systems*, 47(1):109–117, 2011.

[16] Ernest Ower and Ronald Charles Pankhurst. *The measurement of air flow.* Elsevier, 2014.

[17] Ross T Palomaki, Nathan T Rose, Michael van den Bossche, Thomas J Sherman, and Stephan FJ De Wekker. Wind estimation in the lower atmosphere using multirotor aircraft. *Journal of Atmospheric and Oceanic Technology*, 34(5):1183–1191, 2017.

[18] P Bruschi, M Piotto, F DellAgnello, J Ware, and N Roy. Wind speed and direction detection by means of solid-state anemometers embedded on small quadcopters. *Procedia Engineering*, 168:802–805, 2016.

[19] Dunion J. Katzberg S. Comparison of reflected gps wind speed retrievals with dropsondes in tropical cyclones. *Geophysical Research Letters*, 36:L17602, 2009.

[20] JJ Cione, EA Kalina, EW Uhlhorn, Aaron M Farber, and B Damiano. Coyote unmanned aircraft system observations in hurricane edouard (2014). *Earth and Space Science*, 3(9):370–380, 2016.

[21] J. Marshall C. Montalvo, J. D. Richardson. Robust three-dimensional characterization of a complex atmosphere at high resolution using multi-agent windmappers. *AIAA AVIATION 2015, Dallas,TX*, 2015.

[22] Joseph Richardson Joshua Marshall and Carlos Montalvo. Greens function based surrogate model for windfields using limited samples. *Wind Engineering*, 2016.

[23] STK Miller, BD Keim, RW Talbot, and H Mao. Sea breeze: Structure, forecasting, and impacts. *Reviews of geophysics*, 41(3), 2003.

[24] Sytske Kimball. Sea-breezes in the mobile bay area. *Bulletin of the American Physical Society*, 60, 2015.

[25] The weather research and forecasting model.

[26] Carlos J Montalvo, Joe Richardson, and Joshua Marshall. Robust three-dimensional characterization of a complex atmosphere at high resolution using multi-agent windmappers. In *AIAA Atmospheric Flight Mechanics Conference*, page 2856, 2015.

[27] S Sadr S A A Moosavian and P Zarafshan. "Dynamics Modeling and Control of a Quadrotor with Swing Load". *Journal of Robotics*, pages 1–6, 2014.

[28] Hoffman G.M., Huang H., Waslander S.L., and Tomlin C.J. "Quadrotor Helicopter Flight Dynamics and Control: Theory and Experiment". *AIAA Guidance, Navigation, and Control Conference and Exhibit*, pages 6–15, 2007.

[29] Mahoney R., Kumar V., and Corke P. "Multirotor Aerial Vehicles: Modeling, Estimation, and Control of a Quadrotor". *IEEE Robotics and Automation Magazine*, pages 20–32, 2012.

[30] Etkins B. *Dynamics of Atmospheric Flight*. Dover, New York, 2000.

[31] Kiam Heong Ang, Gregory Chong, and Yun Li. Pid control system analysis, design, and technology. *IEEE transactions on control systems technology*, 13(4):559–576, 2005.

[32] Norman S Nise. Control system engineering, john wiley and sons. *Inc, New York*, 2011.

[33] Brandon Troub and Carlos J Montalvo. Meta aircraft controllability. In *AIAA Atmospheric Flight Mechanics Conference*, page 3395, 2016.

[34] Brandon E Troub. *Simulation and Testing of Connected Autonomous Aircraft*. PhD thesis, University of South Alabama, 2018.

[35] Ed Dumas and C Bruce Baker. Push the boundaries. *Meteorological Technology International*, April 2016.

[36] BME280 Combined Humidity and Pressure Sensor. Bosch sensortec. *Germany, Oct*, 2015.

[37] William Gracey. Measurement of aircraft speed and altitude. 1980.

[38] Matthew T Simmons and Carlos J Montalvo. "calibration of a multi-directional pitot-static tube array". 2018.

[39] Steven C. Chapra and Raymond P. Canale. *Numerical Methods for Engineers.* McGraw-Hill Education, 7th edition, 2015.

[40] Sytske Kimball, C. Montalvo, M. Mulekar, and L. Schibelius. Observing atmospheric parameters using quadcopters. In *AMS American Meteorological Society, 98th Annual Meeting, Austin, Texas*, 2018.

[41] Chang-kwon Kang, Jacob Cranford, Madhu K Sridhar, Deepa Kodali, David Brian Landrum, and Nathan Slegers. Experimental characterization of a butterfly in climbing flight. *AIAA Journal*, pages 1–10, 2017.

[42] Huynh N. "Multi-Purpose Towed Systems with Disturbance Sensitive Payloads in Realistic Wind Fields". *M.S. Thesis, University of South Alabama*, 2018.

BIOGRAPHICAL SKETCH

BIOGRAPHICAL SKETCH

Name of Author: Lisa M. Schibelius
Place of Birth: Mobile, Alabama
Date of Birth: July 10, 1993

Graduate and Undergraduate Schools Attended:
    University of South Alabama, Mobile, Alabama

Degrees Awarded:
    Master of Science in Mechanical Engineering, 2018, Mobile, Alabama
    Bachelor of Science in Mechanical Engineering, 2016, Mobile, Alabama

Representative Publications:
    Kimball, S., Montalvo, C.J., Schibelius, L.M. (Jan. 2018) Observing atmospheric paramters using quadcopters. American Meteorological Society Conference, Texas

    Schibelius, L.M., Montalvo, C.J. (May 2017) MultiMASS: A fleet of unmanned aerial vehicles for atmospheric characterization. American Institute of Aeronautics and Astronautics (AIAA) 2017 Forum and Exposition, Denver, Colorado

    Schibelius, L.M., Montalvo, C.J. (March 2017) Design of an atmospheric sensing package for a quadrotor. AIAA 2017 Region II Student Conference, Starkville, Mississippi

    Kimball, S., Montalvo, C.J., Schibelius, L.M. (Jan. 2017) Comparing quadcopter, iMET temperature, pressure, and humidity data with tower data, American Meteorological Society Conference, Seattle, Washington

    Schibelius, L.M., Montalvo, C.J. (April 2016) Simulation analysis of a speed-controlled single-cylinder vehicle. Oral presentation given at the American Institute of Aeronautics and Astronautics Region II Student Conference, Huntsville, Alabama